Ion Implantation-Induced extended defects: structural investigations and impact on Ultra-Shallow Junction properties

Fuccio Cristiano

UNIVERSITE DE TOULOUSE III

Habilitation à Diriger des Recherches

Ion Implantation-Induced extended defects: structural investigations and impact on Ultra-Shallow Junction properties

---

Soutenue le 14 mars 2013 par

Filadelfo CRISTIANO

LAAS-CNRS

Jury :

Frédéric MORANCHO	Université de Toulouse	Président
Alain CLAVERIE	CEMES-CNRS Toulouse	Directeur des recherches
Daniel BENSAHEL	STMicroelectronics Crolles	Rapporteur
Abelmadjid MESLI	IM2NP-CNRS Marseille	Rapporteur
Dimitris TSOUKALAS	NTUA Athènes	Rapporteur
Ray DUFFY	Tyndall Institute Cork	Examinateur
Evelyne LAMPIN	IEMN-CNRS Villeneuve d'Ascq	Examinateur

Table des matières

Introduction

Computing and communication technologies, supported by strong progress in microelectronics and, today, in nanoelectronics, have progressively modified our societies over the last fifty years, virtually affecting every aspect of life. This progress was rendered possible by the aggressive scaling of the MOS transistor, the building block of all integrated circuits. Economic as well as performance/power benefits derived from MOS miniaturisation, justifying the enormous R&D investments made to maintain the miniaturisation pace set by the Moore's law.

Until the early 2000s, the enforcement of Moore's law was mainly based on the "geometrical" Dennard miniaturisation model, whereby the transistor's gate length, oxide thickness and source/drain junction depths are decreased by a constant factor in order to provide an improvement of the transistors speed at a constant electric field. The situation drastically changed during the last decade, due to the unsustainable increase of several deleterious effects associated with miniaturisation, including the increase of parasitic capacitances and resistances. This led to the implementation of alternative solutions (to simple scaling) for ensuring performance improvements when passing from one technology node to the next, such as the introduction of new gate and source materials and, more recently, of new device architectures.

In this context, the scaling strategies for the source/drain regions have always been defined by the sheet resistance/junction depth (R_S/x_j) paradigm, according to which both parameters are required to be sufficiently low to minimise the transistor external resistance and the short channel effects, respectively. To this respect, the ITRS consortium has played a major role in defining the specifications to be reached by future device generations, depending on the planned applications.

The most common method for the fabrication of source/drain regions consists in the localized doping of the substrate material by ion implantation, followed by thermal annealing to achieve electrical activation. The R_S/x_j paradigm has therefore determined the evolution of this fabrication process over the years. Today's Ultra-Shallow Junctions (USJs) are obtained using implantation energies below 1 keV, with the option of adding a pre-amorphisation step and/or an additional impurity co-implantation, while further improvements might come from alternative implantation-based doping technologies, such as molecular, cluster, cold and plasma implants. Similarly, thermal annealing has evolved towards shorter cycles combined with higher temperatures, with currently used RTA "spike" anneals expected to be replaced with even faster methods operating in the millisecond scale and below (Flash-RTA or non-melt laser annealing).

The major problem related to the use of ion implantation is the formation of various defect types resulting from the precipitation of the large amounts of

interstitials and vacancies generated during the implantation process and their interaction with dopant atoms during annealing. In addition, dopants are usually implanted at concentrations exceeding their equilibrium solid solubility limit, leading to their partial precipitation. The various complex interactions between the defects and the implanted dopants are at the origin of the diffusion and activation anomalies that represent the major obstacles to the fabrication of USJs satisfying the ITRS requirements.

Since I joined CNRS in 1998, the aim of my research activity has therefore been to contribute to the understanding and modelling of the physical phenomena occurring during the fabrication of Ultra-Shallow junctions in order to *(i)* extend the capabilities of process simulators, which are systematically used in R&D activity for the design of new devices and *(ii)* directly contribute to the optimisation of the fabrication process.

For my work, I mainly relied on the combined use of Transmission Electron Microscopy for the structural investigation of the extended defects with chemical dopant profiling (SIMS) necessary to investigate dopant diffusion, and electrical characterization methods (4PP and Hall-effect) for the studies on dopant activation.

My research activity in this domain started as a post-doctoral researcher at CEMES, which I joined from Surrey, UK, where I previously obtained a PhD on the Ion Beam Synthesis of SiGe buried layers. At CEMES, I mainly focused on defect studies related to dopant diffusion issues. Since I joined LAAS as a permanent researcher in 2000, I extended my work to the dopant-activation related issues, and more recently to the transfer of these concepts to new materials and processes, successively as a member of the TMN (then M2D) group and of the newly created MPN[#] team that I coordinate since January 2012.

The results that will be presented in this manuscript are strongly based on the work of several PhD students and post-doctoral researchers that I had the chance to co-supervise over the years. In addition, my work was systematically carried out in collaboration with several French and European partners, within several EU projects to which I participated. Among them, a fundamental role for the progress of my work was played at the national level by CEMES and STMicroelectronics with whom I shared the supervision of most of my PhD students working on TEM structural investigations (CEMES) and USJ fabrication process modeling (STM). At the European level, the collaborative work with Peter Pichler, Nick Cowern, Wilfried Lerch and their colleagues respectively at the FhG-IISB laboratory in Erlangen, the University of Surrey (now the University of Newcastle) and Mattson Thermal Products (now Centrotherm Thermal Solutions) has also been crucially important to succeed in my work.

[#] TMN : Tecnologies of Micro and Nano-Systems
M2D: Microdevices and Microsystems for Sensing
MPN: Materials and Processes for Nanoelectronics

For the sake of coherency, I will present in this manuscript only the work that was directly related to the fabrication of ion-implanted USJs, and neglected some equally important works to which I contributed or research projects that I coordinated, particularly the PhD work of Mathieu Gavelle that I co-supervised with Aomar Halimaoui from STMicroelectronics[#]. The project concerned a fabrication process applicable for the realisation of gradual $Si_{1-x}Ge_x$ ultra-shallow layers for pMOSFETs transistors, based on the Silicon-Germanium interdiffusion from pure Germanium deposited layers.

The manuscript is organised in three chapters. The first is dedicated to the fundamental studies on the formation and evolution of implant-induced defects and on their impact on transient enhanced diffusion.

In the second chapter, I will focus on the defect-dopant interactions causing dopant activation anomalies, due to their impact on the active dose and is some cases, also on the carrier mobility. In the case of p^+-n junctions formed by Boron implantation, these anomalies are due to the formation of small Boron-Interstitial Clusters (BICs), which will be at centre of all the studies presented in this chapter.

Finally, the third chapter will present the results of my work on the investigation of implant-induced defects formation and their impact on USJ fabrication, when advanced processes (such as millisecond Flash anneals) or new materials (SOI or Ge-based substrates) are used.

The perspectives of my research activity will finally be presented at the end of the manuscript.

[#] - M. Gavelle, PhD Thesis, University of Toulouse, 2008

- M. Gavelle, E. Scheid, F. Cristiano, C. Armand, J.-M. Hartmann, Y. Campidelli, A. Halimaoui, P.F. Fazzini and O.Marcelot, J. Appl. Phys., 102 (2007) 074904
- M. Gavelle, E.M. Bazizi, E. Scheid, P.F. Fazzini, F. Cristiano, C. Armand, W. Lerch, S. Paul, Y. Campidelli, A. Halimaoui, J. Appl. Phys. 104 (2008) 113524

Chpapter 1

Implant defects and dopant diffusion anomalies

In this chapter I will present the results of my research activity on the characterisation and modelling of the evolution of extended defects and of their impact on dopant diffusion. The chapter starts with a summary of the previous knowledge and the open questions at the time when I started to work on this subject (1998). Sections 1.2 to 1.4 are dedicated to the results achieved on the three main types of investigated defects, i.e. small interstitial clusters, 311 rod-like defects and dislocation loops. Finally, section 1.5 will summarise the obtained results in a global description, including the implementation of the developed defect model into a commercial TCAD simulator.

1.1. Background

1.1.1. Transient Enhanced Diffusion (TED)

Since the introduction of ion implantation for semiconductor doping in the late 1960s, the investigation of dopant diffusion during annealing revealed strong differences compared to the (until then) conventional doping method based on thermal diffusion from a solid or a gaseous source. On the basis of dopant concentration profiles measured by Rutherford Backscattering Spectroscopy (RBS [1]) or Secondary Ion Mass Spectrometry (SIMS [2]), it was evident that at, the very beginning of the annealing process, dopant diffusion in ion-implanted layers occurred at much stronger rates than during thermal processes of non-implanted ones (equilibrium diffusion). In addition, the diffusion enhancement was stronger at low annealing temperatures. After prolonged annealing (or at high temperatures), dopant diffusion slowed down until it occurred again according to equilibrium diffusion. Since the early 1980s [3], this phenomenon has been known as Transient Enhanced Diffusion (TED). A typical example is shown in Figure 1 for Boron diffusion at 900°C induced by furnace annealing, where the minimum anneal time was 35 minutes. Later experiments run with Rapid Thermal Processing tools in similarly implanted layers [4] allowed to quantify in more detail the time scale of TED (cf. Figure 2, where TED at 900°C is already over after 30 s).

Radiation damage caused by the implantation was rapidly suspected to be the cause of TED, although the actual mechanism by which the dopant-damage interaction occurs has been the subject of several debates during no less than two decades. These debates mainly covered two issues. The first concerned the identification of the atomistic mechanisms governing dopant diffusion, particularly the interaction of dopant atoms with the native point defects, i.e. silicon interstitials

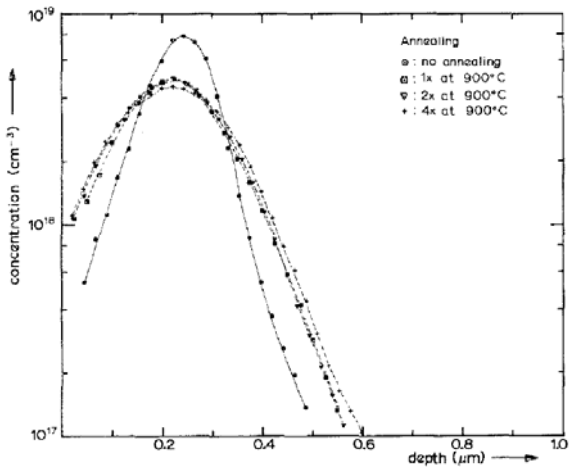

Figure 1 – Concentration profiles of a boron implantation with a dose of 10^{14} ions/cm^2 and at an energy of 70 keV measured after furnace anneals for one, two and four times at 900°C. (Each annealing period is of 35 min duration). From Ref. [2].

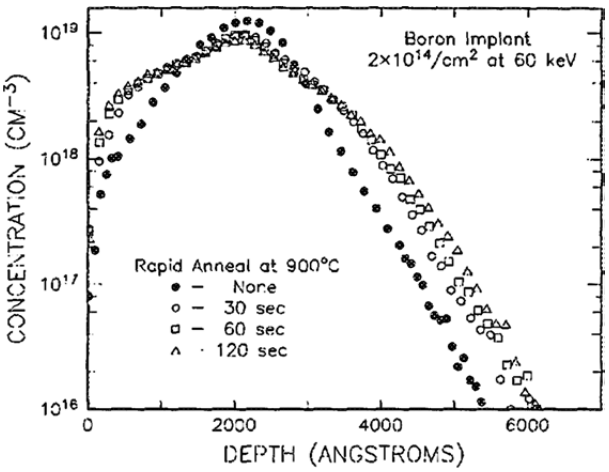

Figure 2 – Concentration profiles of a boron implantation with a dose of 2x10^{14} ions/cm^2 and at an energy of 60 keV measured after Rapid Thermal Anneals for different durations at 900°C. (From Ref. [4])

and vacancies, which are created during implantation with concentrations largely exceeding their equilibrium values. The second concerned the evolution of radiation damage during annealing into larger "extended" defects and their possible role in controlling the concentration of free point defects responsible for dopant diffusion.

The interactions between dopant atoms and point defects were reviewed in detail in the work of Fahey *et al.* [5]. In that work, it was shown that, for a generic dopant *A*, the "effective" diffusion coefficient, D_A, which is measured experimentally by fitting concentration profiles taken at different annealing times using Fick's law, is always the result of a somewhat complex phenomenon in which the vast majority of dopant atoms (that occupy substitutional sites) is immobile, while only a minority of them is in a "defect state" by forming a fast diffusing pair with either type of point defects. Assuming a dependence on both interstitials and vacancies, it was shown that, under intrinsic doping conditions, the effective diffusion coefficient, D_A, can be written as

$$\frac{D_A}{D_A^*} = (f_I)\frac{C_I}{C_I^*} + (1 - f_I)\frac{C_V}{C_V^*} \qquad (1)$$

where C_i and C_v are, respectively, the concentrations of free interstitials and vacancies created by the implant; D_A^*, C_I^* and D_V^* are the corresponding values at thermal equilibrium and f_I is the fractional interstitial component of diffusion under equilibrium conditions. In the case of Boron, it was found that it mainly diffuses through the interstitial kick-out mechanism [6], with f_I being close to unity ($f_I(B)$ = 0.98 [7]). This implies that any measurement of Boron TED in ion implanted structures gives an excellent approximation of the interstitial supersaturation:

$$\frac{D_B}{D_B^*} \approx \frac{C_I}{C_I^*} = S_I \qquad (2)$$

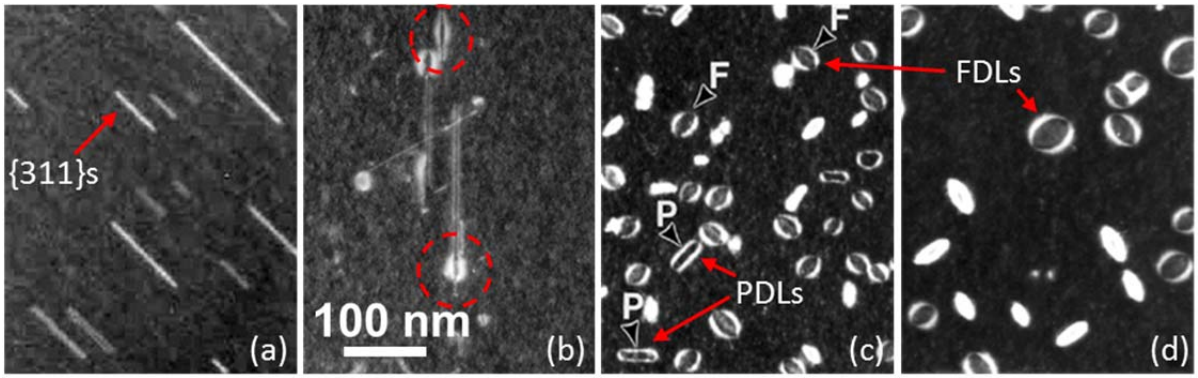

Figure 3 – Different types of extended defects typically observed after annealing of ion implanted silicon. Thermal budget increases from *(a)* to *(d)*. *(a)* {311} *rod-like* defects. *(b)* {311} defects transforming into dislocation loops. *(c)* Perfect (PDLs) and Faulted (FDLs) dislocation loops. *(d)* FDLs only are formed at the highest thermal budgets.

From these results, it was clear that the development of reliable physical models for the simulation of Boron TED depended on the ability to predict the evolution of the free Si interstitial (Si_{int}) supersaturation, S_I, during annealing of an ion implanted silicon layer.

As it will be shown in the following sections (1.2-1.4), the evolution of S_I is intimately related to the formation and evolution of the extended defects resulting from the precipitation of the large amounts of interstitials and vacancies generated during the implantation process. Before discussing these relations in detail, the main types of extended defects typically observed in ion implanted silicon will be presented in next section.

1.1.2. Ion Implantation Defects

Ion implantation in silicon results in the creation of large concentrations of interstitials and vacancies which, during annealing, tend to recombine and eventually condense to form defects of various types. Among them are the ”extended” defects which can be defined as those defects that can be imaged by Transmission Electron Microscopy (as opposed to point defects and small clusters of very few atoms which cannot), thanks to their well-defined crystallographic characteristics and associated strain fields.

Depending on the experimental conditions (implant dose and energy, thermal budget), three main types of extended defects can be observed, which are presented in Figure 3. They include {311} *rod-like* defects (Figure 3a), which appear elongated on <110> directions, typically observed after low temperature anneals (600-700°C). At higher thermal budgets (900-1000°C), the observed defects consist of dislocation loops of two types, perfect dislocation loops (PDLs) and faulted dislocation loops (FDLs) (Figure 3c), with the latter typically surviving at the highest thermal budgets (Figure 3d). In particular conditions, it is also possible to observe the transformation of {311} defects into dislocation loops (Figure 3b).

The detailed description of the crystallographic characteristics of these defects and the reasons for their evolution in size and nature during annealing will be given in sections 1.2, 1.3 and 1.4. Here, it is important to note that all these defects are of extrinsic character, i.e. they are precipitates of the Si_{int} atoms that survive total recombination with the vacancies at the very early stages of annealing.

In addition, their structure and thermal evolution is the same in both amorphising and non-amorphising implants. The only difference between these two cases is the depth at which the defects are formed, i.e. close to the mean projected range of the implanted species in the case of non-amorphising implants or just below the amorphous/crystalline interface in the case of amorphising implants. In the latter case they are known as End-of-Range (EOR) defects.

Finally, there are experimental evidences showing that interstitial clusters as small as di-interstitials can form already in the as-implanted state [8,9]. These results support one of the main assumptions used in the development of physical models of defect evolution (to be presented in the following sections), according to which, at the beginning of annealing, the whole initial supersaturation of Si_{int} atoms created during the implant is arranged in the form of di-interstitial clusters.

1.1.3. Extended defects and TED: experimental evidence and open questions

The link between the TED phenomenon and the evolution of extended defects was clearly demonstrated during the 1990s, particularly through the works of Cowern *et al.* [10] and Eaglesham *et al.* [11] which were published almost simultaneously. In the well-known experiment of Eaglesham *et al.* [11], the time necessary for the "evaporation of {311} defects" was found to be similar to the duration of Boron TED over the temperature range 670°C-815°C. {311} defects were therefore proposed to be the "source of the interstitials". The observed evolution of the defect population (increase of the average length, decrease of the total density) was associated to Ostwald ripening, however, the consequences of this mechanism on the equilibrium between extended defects and free Si_{int} atoms were not considered. Instead, the TED enhancement (Si_{int} supersaturation of the order of 10^3 to 10^4) was supposed to be caused only by the emission of interstitials from the {311}s, the latter phenomenon being due to an "intrinsic" property of the defects, rather than to the recombination of emitted interstitials at the surface.

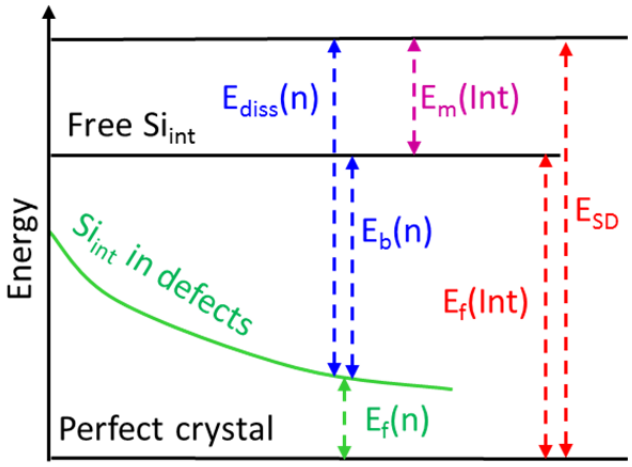

Figure 4 – Schematic description of the energy levels associated to free and clustered Si_{int} atoms in a Si matrix.

A physical model to explain these

results was proposed soon after by Rafferty *et al.* [12]. Here, the dynamic equilibrium between captured and emitted free interstitials was correctly modelled, with the {311}s dissolution rate being controlled by the interstitial recombination at the surface. In particular, the emission rate of free interstitials from a defect was supposed to be thermally activated through the sum of two activation energies, schematically presented in Figure 4: the binding energy, E_b, necessary to "extract" a free Si_{int} atom from a defect and the migration energy, E_m, necessary for its diffusion in the silicon crystal. Their sum, E_{diss}, is therefore the activation energy for the dissolution of the defects. For comparison, the formation energy of free interstitials from a perfect crystal, $E_f(int)$, is also reported in Figure 4, together with the activation energy for the interstitials self-diffusion, $E_{SD} = E_f(int) + E_m$. The activation energy for the defect dissolution can be written in an equivalent way by replacing the binding energy, $E_b(n)$, by the formation energy of the defect, $E_f(n)$, i.e. the energy required to add an extra Si_{int} atom to an existing defect of size n:

$$E_{diss}(n) = E_b(n) + E_m(Int) = E_{SD}(Int) - E_f(n) \quad (3)$$

According to the Ostwald ripening theory, large defects are more energetically favourable than small ones, i.e. $E_b(n)$ (or $E_f(n)$) is expected to increase (or decrease) with increasing defect size, as schematically show in Figure 4 (green line). However, the size dependence of the defect binding energy was not known in the work of Rafferty *et al.*, and a constant value was taken instead. As a consequence, the proposed model could not simulate the time evolution of the size and density of {311} defects, but only the evolution of the total number of Si_{int} atoms contained in the defects, with, in addition, some considerable discrepancies in the shape of the evolution curves. It was therefore concluded in that work that "*a more sophisticated model with a distribution of cluster sizes would capture this effect*".

In an independent experiment, Bonafos *et al.* [13] investigated TED in different experimental conditions compared to the work of Eaglesham *et al.* (amorphising implants, higher annealing temperatures around 1000°C), where Faulted Dislocation Loops (FDLs) are formed. Also in this case, the link between TED and extended defects was evidenced by the experiment. But in addition, a full Ostwald ripening theory for FDLs was developed [14] and applied *(i)* to show that the TED decay time closely followed the evolution of the interstitial supersaturation in equilibrium with the defects and *(ii)* to successfully predict the size and density of the loop population during anneal. However, in this work, it was assumed that FDLs directly nucleate from the free excess interstitials created during the implant, rather than being the final result of the transformation of some smaller and less stable "precursor" defects. As a consequence, while correctly predicting the low TED levels (Si_{int} supersaturation of the order of *10*) typically measured in the presence of FDLs, this model could not predict the rapid decrease of the Si_{int} supersaturation (from initial values close to 10^5) occurring in the early stages of the anneal.

Indeed, several experimental studies run in the same years [10,15,16,17] indicated that extremely high TED levels (Si_{int} supersaturation of the order of 10^5) could be measured when using implant and anneal conditions (low non-amorphising doses, annealing temperatures not higher than 750°C) that did not result in the formation of observable extended defects. The diffusion time scales observed in these experiments were much shorter than those observed in experiments where TED was driven by extended defects evolution ({311}s or DLs), giving rise to the "*ultrafast TED*" definition for this apparently different phenomenon. These results implied that it should exist "*more than one source of interstitials for TED*" [15]. The ultrafast TED was therefore alternatively assumed to be due to the release of interstitials directly "*emerging from the ion collision cascades*" [10], to the release of "*weakly bound excess interstitials"*(WBEI) generated during the implant [16], or to the equilibrium of free interstitials with "*submicroscopic defects that are less stable than {311} defects*" [18].

While considerable knowledge was acquired thanks to all these investigations, some open questions clearly remained that needed to be answered. In particular, concerning the defect evolution, a unified description explaining why, depending on the implant and annealing conditions, a given defect type is formed, why it dissolves during annealing or transforms into a larger defect with different crystallographic characteristics and how it evolves in the presence of different defect types, was still missing.

In the following, I will therefore present the results of some research works conducted under my supervision (PhD and post-docs) or in collaboration with other colleagues (mostly within European research projects) that have contributed to establishing the "global vision" of the defect evolution mechanisms available today, and allowed to develop a comprehensive physical model for the simulation of TED in most technology relevant experimental conditions.

The results will be presented following the defect type in sections 1.2-1.4, while a global description in terms of their implications on TED modelling, including the model implementation into commercial TCAD simulators will be given in section 1.5.

1.2. Small interstitial clusters

As shown in section 1.1.3, several investigations indicated that extremely high values of Boron diffusion enhancement ("*ultrafast TED*") can occur when damage is introduced in silicon at low levels, i.e. in the absence of visible (by TEM) extended defects [10,15,17].

Indeed, only {311}s and DLs are directly observable by TEM after ion implantation (cf. section 1.1.2). Even when using low temperature anneals (600-700°C), the smallest defects that can resolved in TEM are 2 nm-long {311} defects containing no less than ~40 atoms.

From previous TED experiments [18], it was suspected that ''precursors'' of the {311} defects might exist with binding energies intermediate between those of di-interstitials and of larger defects and that might also play a role in TED. In this section, we therefore present the experimental study that allowed to determine the formation energies, E_f, of these precursor clusters [19].

1.2.1. Experimental evidence

This was achieved by first performing accurate TED measurements using B-doped marker layers, to determine the transient interstitial supersaturation, S, during cluster ripening in a "low-damage" system. Following a low-dose implant (20 keV Si^+, $2x10^{13}$ cm^{-2}), the deep Boron marker layers, analyzed by secondary-ion mass spectrometry, showed significant diffusive broadening within the first seconds of annealing at 600°C (see Figure 5).

Figure 6 (symbols) reports the corresponding values of the Si_{int} supersaturation $S=D_B/D_B^*$, where D_B is the average Boron diffusivity extracted from the concentration profile broadening and D_{B^*} is the equilibrium Boron diffusivity. The data show two phases of enhanced diffusion. An initial phase of ultrafast TED (more than 10^6 at 600°C) followed by a sharp drop in S and a lower "plateau" with near-constant S. The supersaturation values of the plateau regions were similar to those measured in previous studies of TED driven by {311} defects [11], whose presence in these structures was confirmed by TEM investigations. In contrast, no extended defects were observed by TEM for annealing times corresponding to the ultrafast TED regime.

The hypothesis that the ultrafast regime reflects the ripening of very small interstitial clusters (i.e. the precursors in the nucleation of {311} defects) was finally demonstrated by an inverse modeling of the experimental data, which allowed to extract from S the fundamental physical information on the interstitial clusters formation energy, E_f.

1.2.2. Modelling

Although initially developed for the specific investigation of small interstitial cluster, this model represents the basis for all further extension to larger defects. The main physical concepts will therefore be presented in this section, while in the following ones we will show how our subsequent work has contributed to its improvement/extension to all defect families. It has also to be noted that the model equations will be presented in a different (but equivalent) form compared to the original work of Cowern, in order to facilitate the understanding of its extension to all defect types, as discussed in the following sections.

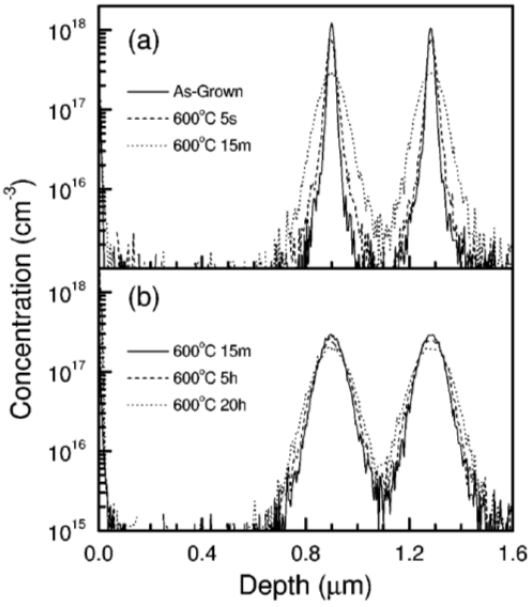

Figure 5 – B concentration profiles before and after annealing for a range of times at 600°C. (From Ref. 19)

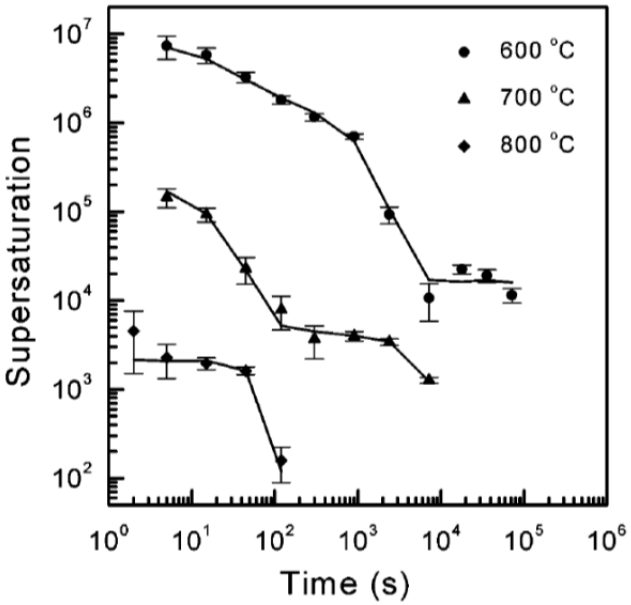

Figure 6 – Interstitial supersaturation, S, as a function of annealing temperature and time. Symbols: experimental values. Lines: fits based on Ostwald ripening model (From Ref. 19)

The model is based on the main assumption that, similarly to larger extended defects ({311}s [20] and DLs [14]), small interstitial clusters also evolve following an Ostwald ripening mechanism, i.e. they grow in size and reduce their density during annealing through the emission and capture of the Si self-interstitials they are composed of, the driving force for this phenomenon to occur being the minimization of the total interfacial energy. Further assumptions state that *(i)* the number of free Si_{int} atoms interstitials in the wafer is always much smaller than the number of clustered Si_{int} and *(ii)* the volume fraction occupied by the clusters is small. In such conditions, S quickly reaches a quasi-steady state with respect to the cluster-size distribution ($\frac{dC_i}{dt} \rightarrow 0$), while clusters only interact through the mean field between them.

Using the rate equation approach [20,21], the evolution of the cluster size distribution, N_n, can be described by the following equation:

$$\frac{dN_n}{dt} = F_{n-1}N_{n-1} - F_nN_n - R_nN_n + R_{n+1}N_{n+1} \quad (4)$$

where F_n and R_n, are the forward and reverse reaction rates describing the capture and emission of Si_{int} from clusters of size n. In a diffusion-limited defect growth mechanism, F_n and R_n are such that the growth rate, dn/dt, of a cluster containing n atoms can be written as follows:

$$\frac{dn}{dt} = |F_n - R_n| = D_iC_i^* \frac{A_n}{R_{eff}}(S - S_n) \quad (5)$$

where D_i and C_i^* are the diffusivity and equilibrium concentration of Si_{int} in Si, and the capture efficiency $\frac{A_n}{R_{eff}}$ is given by the ratio between the capture cross-section of the cluster, A_n, and the radial extension of the Si_{int} diffusion field, R_{eff}. Finally, $S = \frac{C_i}{C_i^*}$ is the mean supersaturation of free interstitials within the matrix (mean field) and S_n is the supersaturation of interstitials atoms in equilibrium with a cluster of size n. Based on equation (5), the capture and emission rates, F_n and R_n, can therefore be written as follows:

$$F_n = D_i C_i^* \frac{A_n}{R_{eff}} S \tag{6}$$

and

$$R_n = D_i C_i^* \frac{A_n}{R_{eff}} S_n \tag{7}$$

The value of S reflects the evolution of the free Si_{int} atoms in dynamical equilibrium with the clusters. These atoms can be trapped (or emitted) by an existing cluster. In addition, they can diffuse towards the surface where they annihilate. Under the steady-state assumption mentioned above, S can be directly determined as follows:

$$S = \frac{\sum_{n=2}^{\infty} \beta_n R_n N_n}{D_i C_i^* \left[\left(\sum_{n=2}^{\infty} \frac{A_n}{R_{eff}} N_n \right) + \frac{1}{R_p + L_{surf}} \right]} \tag{8}$$

where R_p is the depth at which the defects are located[#] and L_{surf} is the mean free path for the interstitial recombination at the surface[##]. The quantity β is the number of atoms released by the break-up of a cluster ($\beta = 2$ for $n = 2$, $\beta = 1$ otherwise).

Finally, S_n is given by the Gibbs–Thomson equation [22] and can be written

$$S_n = exp\left(\frac{E_f(n)}{kT}\right) \tag{9}$$

where the formation energy, E_f, is defined as the energy required to add one extra atom to the defect, i.e., the derivative of the total energy of the defect, E_T, with respect to the number of atoms bound to it, n:

$$E_f(n) = E_T(n+1) - E_T(n) = \frac{dE_T(n)}{dn} \tag{10}$$

[#] In the case of non-amorphising implants, this depth corresponds to the mean projected range of the implant.

[##] The impact of the surface on the defect evolution will be discussed in more detail in section 1.5.2

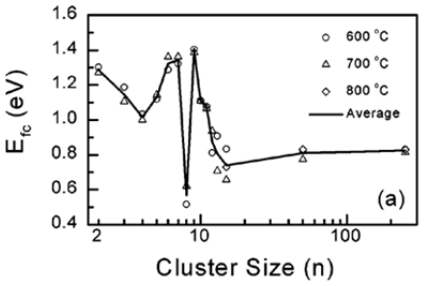

Figure 7 – Formation energies of interstitial clusters, estimated from the Ostwald ripening analysis of ultrafast TED experiments. (From Ref. 8)

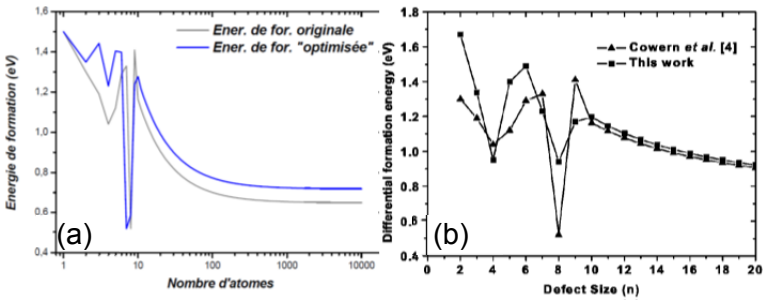

Figure 8 – Small cluster formation energies obtained with different extraction methods and their comparison with the original values of Cowern et al.[19] (a) "Simulated annealing method" (From Ref. 25). (b) "Genetic algorithm" (From Ref. 26).

When solved together, the $n+1$ coupled differential equations (4) and (8) allow to fully describe the time evolution of the cluster size distribution, N_n, and of the supersaturation of free Si_{int} atoms, S, provided all the physical parameters included in the model are known. In particular, two of them depend on the cluster geometry, namely the capture efficiency $\frac{A_n}{R_{eff}}$ and the formation energy $E_f(n)$. Details of their calculation will be discussed below for the small interstitial clusters, then in section 1.3.2 (p.22) for {311} defects and in section 1.4.2 (p. 29) for dislocation loops.

In the original work of Cowern *et al.*, the determination of the formation energy of small interstitial clusters was the final goal. The model was therefore used in a "reverse" fashion, where the experimental values of the Si_{int} supersaturation, S (cf. Figure 6), were "best-fitted" using $E_f(n)$ (as well as the product $D_iC_i^*$) as free parameters. Concerning the other parameters, the capture efficiency $\frac{A_n}{R_{eff}}$ was calculated assuming that the clusters are elongated planar defects whose capture radius, a_n, is a linear function of n. In our implementation of the model, we have instead assumed a spherical shape for the clusters for which $\frac{A_n}{R_{eff}}$ is equal to $4\pi r$ [23], where the cluster radius r is related to the number of atoms contained in it, n, by $n = \left(\frac{4\pi r^3}{3v_m}\right)$, with the atomic volume of Si v_m = 1.97x10^{-23} cm^3. These different assumptions have been verified to induce only modest variations in the simulation results. The surface was assumed to be a perfect sink (L_{surf} = 0) and R_p was taken equal to the mean projected range of the Si implant. Finally, the cutoff cluster size, n_{max}, was set at 250, large enough to include the small {311} defects observed in this study.

The formation energy values that provided the best fit to the supersaturation values (see lines in Figure 6) are presented in Figure 7. Two main conclusions can be drawn from this result. First, the formation energies of small clusters (n < 10) are systematically higher than those of larger clusters, whose formation energy is close to the one estimated for {311} defects [24]. This confirms that the small clusters are

indeed the precursors of {311} defects and naturally transform into the latter in order to decrease the total energy of the system.

Second, the formation energy of small clusters has an "oscillating" behavior with two particularly stable configurations (E_f minima) at n=4 and 8. These features have a strong impact on the time evolution of both the cluster size distribution as well as the Si_{int} supersaturation, with nearly half of the clustered interstitials remaining in clusters of size 8 even after several hours at 600°C. This behavior is clearly different than the one known for larger defects ({311}s and DLs), where the formation energy is found to monotonically decrease with the defect size. However, all attempts to fit ultrafast TED experimental data with such a monotonic formation energy curve completely failed. In addition, further studies in which different algorithms have been used to determine the small clusters formation energies, have resulted in similar values, as shown in Figure 8(a) ("simulated annealing" method [25]) and Figure 8(b) (genetic algorithm [26]).

Finally, it has to be noted that, although close to the known value for {311} defects, the formation energy of large cluster was found to have a quasi-constant value in the original work of Cowern et al., i.e. it exhibited no size dependence. In fact, this experiment was not designed to specifically investigate this issue, as the extremely low implant dose did not allow to form large enough {311} defects to allow a reliable measurement of their size and density evolution.

The extension of this defect model to {311} defects, as well as the corresponding experiments will therefore be presented in the next section.

1.3. {311} rod-like defects

As discussed in section 1.1.2, {311} rod-like defects typically form in ion implanted silicon (both in amorphising and non-amorphising implants) during annealing at low temperatures (600-850°C). They appear as long narrow defects, elongated on <110> directions (cf. Figure 3a in section 1.1.2). When imaged in HREM cross section, their {311} habit plane can be observed, as shown in Figure 9 taken from Ref. 11. A detailed description of the {311} defect structure is given in Ref. 27, where it is pointed out that most of the available knowledge about {311} rod-like defects relies on the assumption that they have the same atomic structure as the larger planar {311} defects formed during electron irradiation. As shown in Figure 10, {311} defects consist of chains of additional atoms in the <110> direction [30] (each one defining the defect length). These chains arrange in the <332> direction (defect width) so that the whole defect lye on a {311} plane.

Eaglesham and co-workers [11] carried out the first detailed investigation of the evolution of {311} defects during annealing, which allowed to establish their crucial role in the Boron transient enhanced diffusion phenomenon. In that study, they observed an increase in the defect average length and corresponding decrease in

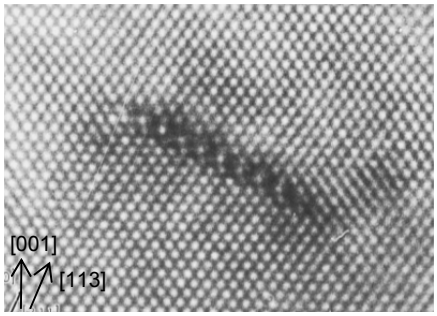

Figure 9 – Cross-section HREM showing the typical image contrast and the habit plane of an ion-implant-induced {311} defect. (From Ref. 11).

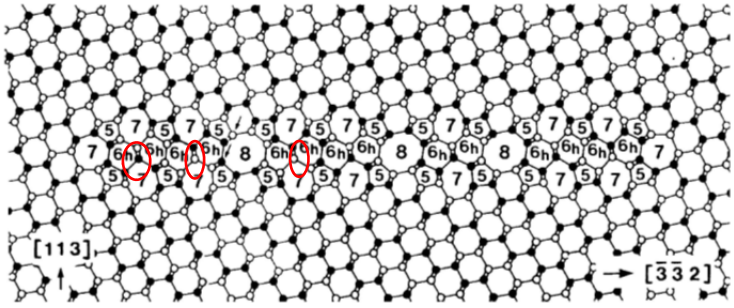

Figure 10 – Atomic structure of an electron-irradiation-induced planar {311} defect viewed along a $[1\bar{1}0]$ direction. The atomic rings which are different from those in a perfect crystal are designed by numbers. Chains of additional atoms in the <110> direction belong to five-, hexagonal six- and seven-membered rings (cf red shapes). Notice that both edges of the defect have no dangling bonds. (From Ref.30).

density during annealing. In addition, the total amount of Si_{int} atoms contained in the defects was found to decrease. Although this behavior was proposed to be explainable in terms of an Ostwald ripening mechanism, the observed flux of Si_{int} atoms away from the damage region was not associated to the recombination of interstitials at the surface. Instead, the {311} defect dissolution (with en exponential behavior) was assumed to be an "intrinsic" characteristic of the defect. This description was later supported by a TEM experimental study on the evolution of the width of the {311} defect band during annealing [28] that concluded stating that the surface is not the limiting factor in the interstitial removal from {311} defects. In contrast, TED experiments with Boron marker layers [29] had clearly proved that the surface plays a key role in annealing implant damage and provided a first quantitative estimation of the surface recombination length. In section 1.3.1, we will therefore present some of our experimental work that contributed to clarify the actual mechanism by which {311} defects dissolve in the presence of a recombining surface.

Finally, concerning the atomistic modeling of {311} rod-like defects, one of the key issues is the determination of the defect formation energy (cf. eq. 10). In previous defect models [31,32] the formation energy of {113} defects was determined through a fitting procedure of some experimental results of defect evolution, similarly to the case of small interstitial clusters seen in previous section. In other models [33] the {113} formation energy was instead calculated on the basis of the crystallographic defect structure, however the considered structures corresponded to a different (and simpler) defect type. The method we developed for the calculation of the {311}s formation energy and the related results of defects and TED evolution will be shown in section 1.3.2. Most of the results presented in this section were obtained within the PhD theses of B. Colombeau, P. Calvo and Y. Lamrani, that I co-supervised with Alain Claverie and Gérard Ben Assayag from CEMES-CNRS between 1998 and 2005.

1.3.1. Experiments on {311}s dissolution kinetics

For the experimental investigation of the evolution of {311} defects, we used typical experimental setups where the defects were induced by a non-doping non-amorphising implants (typically Si^+ ions at doses not higher than $2x10^{14}$ cm^{-2}) [34,35], while the Si substrates contained boron marker layers, allowing the additional investigation of the Si_{int} supersaturation through the measurement of their diffusion enhancement.

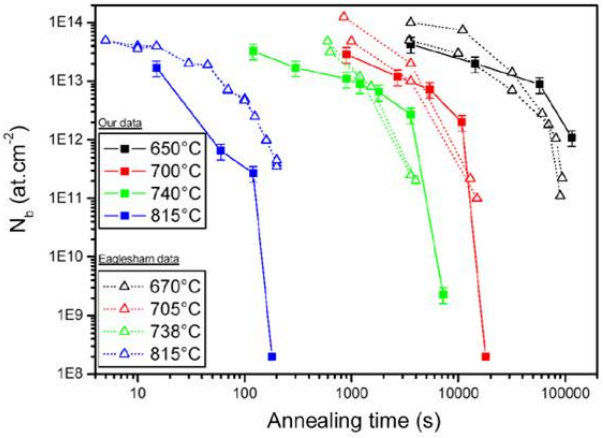

Figure 11 – Time evolution of the number of atoms stored in {311} defects during annealing at various temperatures following Si^+ implantation at 40 keV to a dose of $6x10^{13}$ cm^{-2}. Filled symbols: data from this work. Empty symbols: data from Ref.11.

In one particular experiment, we selected process conditions close to those originally used by Eaglesham et al. [11] to study the dissolution of {311} defects, i.e. 40 keV Si^+ $6x10^{14}$ cm^{-2}, and annealing in the 650°C-815°C range. Our results are presented in Figure 11 (filled symbols) and compared to those obtained by Eaglesham (empty symbols). Although the general trend in the two experiments is similar, our data clearly indicate that the defect evolution and dissolution process is characterised by two separate regimes. Referring for example to Figure 12, relative to the data obtained at 740°C, it appears that a classical Ostwald ripening process occurs first (increasing size, decreasing density, not shown), during which a weak interstitial loss from the defect band is observed. Following this initial period, defect dissolution occurs very rapidly with a much higher dissolution rate than the one observed at the early stages of the annealing. Our data could not therefore support the proposed explanation according to which the {311} dissolution could be fitted by a single exponential decay function throughout the annealing process.

The transition from the weakly non-conservative Ostwald ripening regime to the

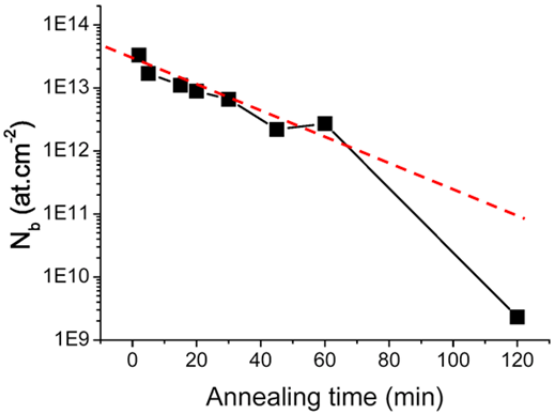

Figure 12 – Total number of Si_{int}s contained in the {311} defects as a function of annealing time for an annealing temperature of 740°C. An exponential decay function is also shown for comparison.

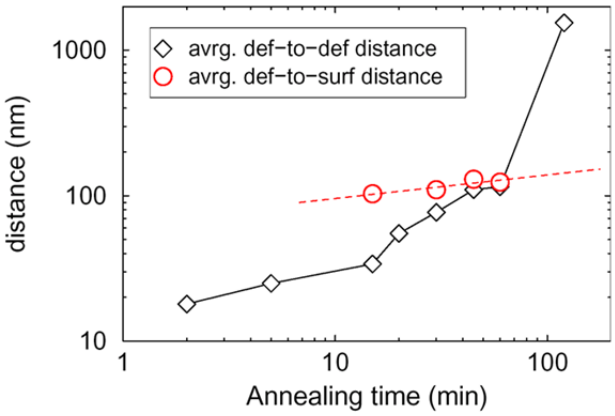

Figure 13 – Time evolution of the average defect-to-defect distance (diamonds) and the defect-to-surface distance (circles) during annealing at 740°C.

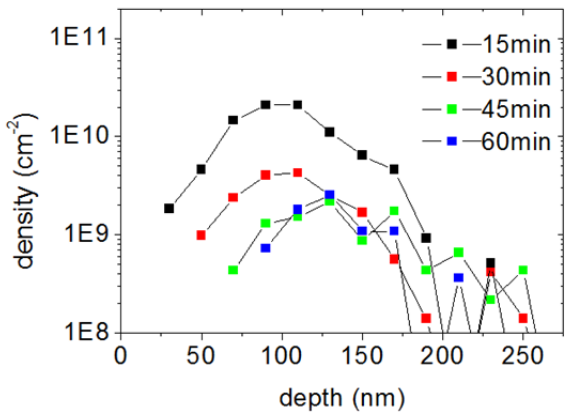

Figure 14 – Time evolution of the defect depth distribution after 40 keV Si implantation to a dose of $6X10^{13}$ cm^{-2} and annealing at 740°C.

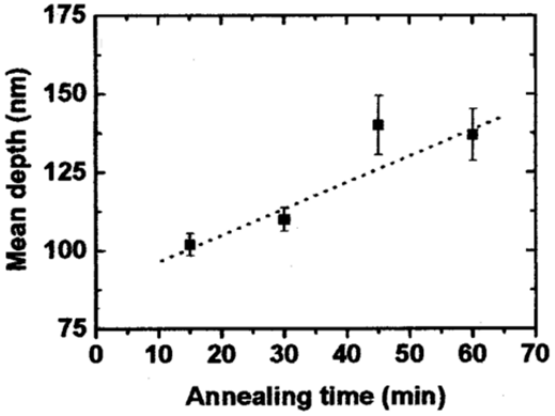

Figure 15 – Time evolution of the mean depth of the defects formed by 40 keV, $6x10^{13}$ cm^{-2} Si implant annealed at 740 °C. The mean depth increases with time.

rapid dissolution regime could finally be understood by considering the comparison between the average defect-to-defect distance and the defect-to-surface distance during annealing, shown in Figure 13 for an annealing temperature of 740°C. Indeed, during the early stages of the anneal, the high defect density implies that the average distance between defects is much lower that the distance between the defects and the surface. The interstitials emitted by one defect during the Ostwald ripening process have therefore a higher probability to be re-captured by a close defect rather than dissolving at the surface. However, the progressive decrease of the defect density during annealing results in an increase of the average defect-to-defect distance that becomes comparable and eventually higher than the defect-to-surface one. In this case the interstitials emitted by the defects have a much higher probability to diffuse and recombine at the surface rather than being recaptured by other defects, leading to a rapid dissolution of the whole defect layer. For the case shown in Figure 13 (740°C) this transition occurs after 50-60 min annealing, in agreement with what is found experimentally (cf.Figure 12). These results prove that the dissolution of {311}s is not an "intrinsic" characteristic of the defects themselves, but is driven by the proximity of the surface that acts as a recombination site.

We also performed on the same test structures a detailed investigation of the evolution of the depth profile of {311} defects during annealing [36] which provided a further experimental evidence that the surface is the main sink for interstitials escaping from the defect region. Figure 14 presents histograms of the depth distribution of the {311} defects during annealing at 740°C. The {311} defect band is found to shrink preferentially on the surface side, while the peak of the distribution moves towards the right (from 100 to 125 nm). The mean depth of the defects, obtained by integrating the defect density over depth, is shown in Figure 15 and is found to significantly increase with annealing time. In contrast to the previous data from Moller et al. [28], it therefore appears that the majority of the interstitials escaping from the defect band originate from the near surface side of the band, and

only later do the deeper defects start to dissolve as well. Possible reasons for the different results found by Moller are given in Ref. 36.

The rapid {311} dissolution is evidently a consequence of the proximity of the silicon surface, which is a sink for interstitials escaping from the defect band. The absence of dissolution on the deep side of the band shows that interstitials escaping into deeper regions of the silicon encounter few significant sinks, and most of them simply return to the band to be reincorporated within extended defects. These results perfectly support the view that the surface is the ultimate sink for interstitials escaping from the defect region[#].

Finally, it is important to note that, in order to achieve such a detailed knowledge on the defect dissolution kinetics, it was necessary to dispose of a reliable method for the quantitative TEM analysis of {311} defects. It was thanks to such method [35] that it was possible to identify and explain these specific features which were not evidenced in previous works.

1.3.2. Modelling

In section 1.2.2, it was mentioned that two of the parameters contained in the physical model describing the Ostwald ripening of extended defects depend on the defect geometry, namely the capture efficiency $\frac{A_n}{R_{eff}}$ and the formation energy $E_f(n)$. In this section, we present the method we developed for their calculation in the case of {311} defects. Once inserted in the system of $n+1$ coupled differential equations (4) and (8), it is then possible to perform predictive simulations of the evolution of {311} defects and of TED in their presence during annealing.

The calculation of the formation energy is based on the defect crystallographic structure, and includes the calculation of the elastic energy of the various dislocation segments forming it as well as the stacking fault energy [37]. Considering that the Burgers vector, $\boldsymbol{b}$, of a given {311} defect is parallel to the <611> direction [30,38] closest to the defect plane normal and according to the defect description given in section 1.3 (cf. Figure 10), the defect can be assumed to be planar and of rectangular shape. It consists of two edge dislocations on the <110> direction (corresponding to the defect length, L), two mixed dislocations on the <332> direction (corresponding to the defect width, W) and a stacking fault. The total energy $E_{T\text{-}311}(n)$ of a {311} defect of size n is therefore given by:

$$E_{T-311}(n) = E_{el} + E_{fault} = 2 \times \left(E_{edge} + E_{mixed}\right) + \gamma\, n \qquad (11)$$

where γ is the stacking fault energy per atom in the defect (0.44 eV/at) and

[#] The impact of the surface on the defect evolution will be further discussed in section 1.5.2

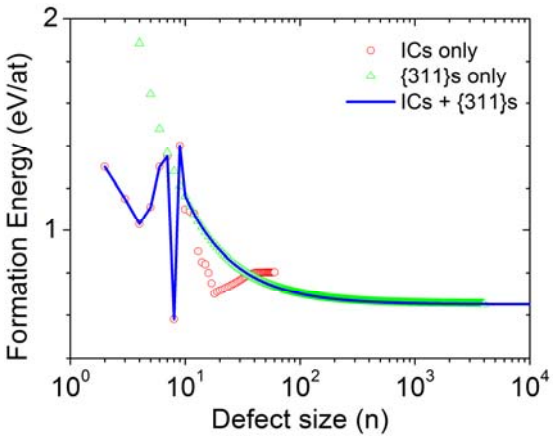

Figure 16 – Red dashed line: formation energies of small interstitial clusters (*n<10*) and of {311} defects (*n>10*) used in our simulations. The blue line refers to {311} defects only.

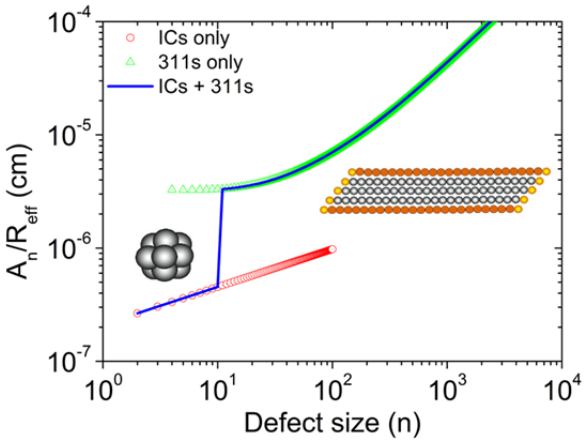

Figure 17 – Variation of the capture efficiency $\frac{A_n}{R_{eff}}$ of clusters and {311} defects as a function of the number of Si atoms they contain.

$$E_{edge} = \frac{\mu b^2 L}{2\pi(1-\nu)} \ln\left(\frac{2W}{b}\right) \quad ; \quad E_{mixed} = \frac{\mu b^2 W}{2\pi}\left[cos^2\theta + \left(\frac{sin^2\theta}{1-\nu}\right)\right] \ln\left(\frac{2L}{b}\right) \quad (12)$$

where θ is the angle between the mixed dislocation line (<332>) and the defect Burgers vector (<116>) directions, μ is the shear modulus (7.55x10^{10} N/m^2) and ν is the Poisson ratio (0.3). The defect width is assumed to be constant [11] (W = 4nm). Concerning the atomic density on the {311} planes within the defects, d_{113}, we take 5x10^{14} cm^{-2} determined by Takeda [39], so that the number of atoms contained in a {311} defect is equal to:

$$n\,(L) = d_{113} W\, L = 20\, L(nm) \quad (13)$$

Further details about the choice of the numerical values of the parameters used in this calculation are given in Refs. [37,40,41].

The formation energy of {311} defects, calculated according to equation (10) is reported in Figure 16 (green triangles). It monotonically decreases as the defect size increases, i.e. large defects are more stable than small ones. For extremely large defect sizes, the formation energy value tends to the asymptotical limit set by the {311} stacking fault energy. For small defect sizes (less than 10 atoms) it appears that {311} defects are much less energetically favourable than small interstitial clusters (cf. red circles in Figure 16). Assuming that a structural transition occurs at size 10[##], it is therefore possible to continuously describe the defect evolution from small interstitial clusters to larger {311} defects using a single curve such as the one shown in Figure 16 (blue line).

[##] It has been verified [37] that the exact position of the cluster-to-{311}s transition has not a strong impact on the simulation outputs, provided the two minima of the formation energy at sizes 4 and 8 are kept.

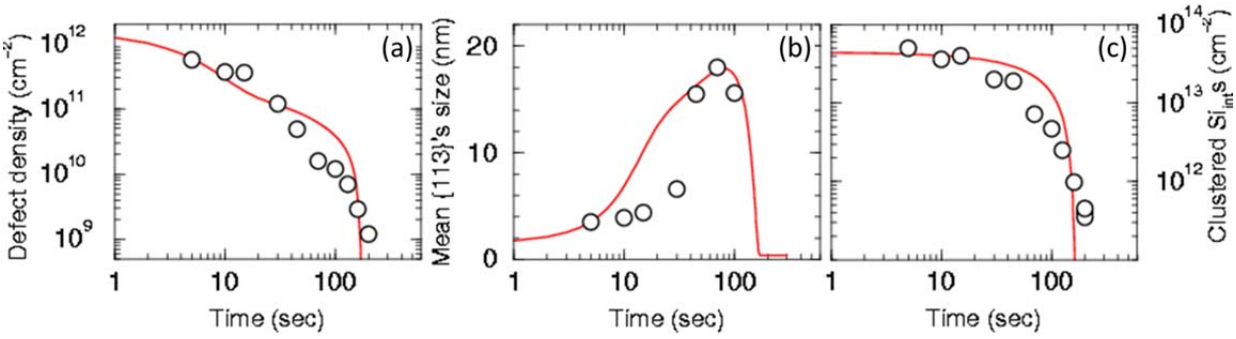

Figure 18 – Time evolution of the {311} defect density *(a)*, defect size *(b)* and number of Si_{int} atoms they contain *(c)* during annealing at 815°C, following a 40 keV Si^+ implant ($5x10^{13}$ cm^{-2}). Symbols: TEM data from Ref. 11. Lines: simulations using our physical model.

Concerning the capture efficiency $\frac{A_n}{R_{eff}}$, we modified a previous calcuation of Gencer and Dunham [42] who proposed that the capture of incoming Si_{int} atoms occurs only through the short edges of the {311} defects, which implies that A_n is independent on the defect length. Instead, we preferred to assume that the capture area increases as they become longer. A_n is therefore given by the sum of three terms (cf schematic drawing of a rectangular {311} defect in Figure 17): (*i*) two cylinders at the short defect edges ("yellow atoms" in Figure 17), (*ii*) two cylinders along the length sides ("red atoms" in Figure 17) and (*iii*) four hemispheres at the corners. This choice was later supported by stress calculations and TEM image simulations carried out at the Ioffe institute of St Petersburg [41] which showed that the regions located in the vicinity of the {311} long sides (parallel to the <110> direction) are submitted to tensile stress and are therefore expected to preferably capture Si interstitial atoms. The resulting $\frac{A_n}{R_{eff}}$ for {311} defects is shown in Figure 17 (green triangles), together with the capture efficiency of small spherical clusters (red circles). Similarly to the calculation of the formation energy, a transition from small interstitial clusters to {311} defects is set at a defect size of 10 atoms, so that the blue solid line corresponds to the "global" capture efficiency of ICs and {311} defects.

Once the values of $\frac{A_n}{R_{eff}}$ and $E_f(n)$ were determined for the {311} defects, it was possible to test the model against existing studies on the evolution of {311} defects and of TED in their presence during annealing [43]. An example is given in Figure 18, concerning the Eagleasham experiment on the dissolution of {311} defects after a non-amorphising implant [11] (40 keV Si^+, $5x10^{13}$ cm^{-2}), and annealing at 815°C. An excellent fit is obtained by adjusting only the $(R_p + L_{surf})$ parameter (cf. eq. 8) at 80 nm. The Ostwald ripening of the defects i.e., the density decrease (Figure 18a) and the size increase (Figure 18b) they experience during this non-conservative process (Figure 18c) perfectly matches the experimental observations and this evolution strongly depends on the size dependence of the formation energy of the defects. In addition, a very good fit of the experimental results was obtained for all the annealing temperatures considered in that study (see Figure 19) without modifying any of the model parameters. Finally, in order to verify the ability of the model to

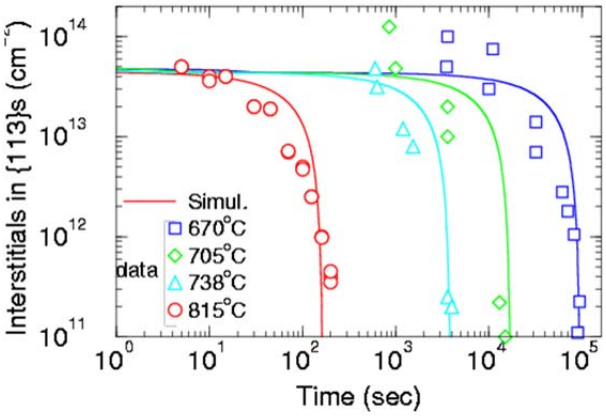

Figure 19 – Time evolution of the number of atoms contained in {311} defects, after 40 keV Si^+ implantation to a dose of $5X10^{13}$ cm^{-2} and annealing at different temperatures. Symbols: TEM data from Ref. 11. Lines: simulations using our physical model.

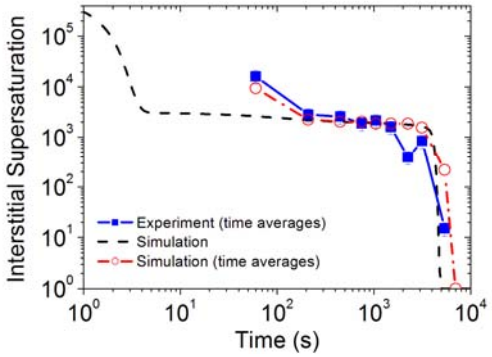

Figure 20 – Diffusion enhancement of B marker layers as a function of annealing time, following Si implantation at 40 keV to a dose of $6x10^{13}$ cm^{-2} and annealing at 740°C. Squares: experiment. Line: simulation (time dependence). Circles: simulations (average values corresponding to the experimental time intervals).

predict the Boron TED in the presence of {311} defects, we reproduced the same experiment (cf. section 1.3.1) using Si substrates that contained boron marker layers, allowing the investigation of the Si_{int} supersaturation through the measurement of their diffusion enhancement [25].

Figure 20 reports the measured Si_{int} supersaturation during annealing at 740°C (blue symbols). Each point represents the average diffusion enhancement during the time interval between two consecutive annealing times. The high diffusion enhancement measured for the first time interval (0-60 sec) reflects the contribution of small interstitial clusters to TED at the early stages of annealing (before their transformation into {311} defects). This behaviour is perfectly reproduced by simulations (black dashed line), once the average diffusion enhancements corresponding to the experimental time intervals are calculated (red symbols).

1.4. Dislocation Loops

Dislocation loops (DLs) are the most common and well known type of extended defect in annealed ion-implanted silicon and were already observed and studied in details using weak-beam dark-field (WBDF) TEM methods in the 1970s [44,45]. An example of DLs observed in WBDF-TEM after an amorphising Ge^+ implant is shown in Figure 21. Two types of DLs have been observed, the faulted Frank dislocation loop (FDL), labeled "F" in Figure 21, and the perfect dislocation loop (PDL), labeled ''P''. A method for the unambiguous determination of the DLs nature and structure has been proposed by De Mauduit *et al.* [46]. They demonstrated that the faulted dislocation loops lie on {111} planes and have a Burgers vector $\boldsymbol{b}$ of $a/3<111>$ perpendicular to the loop plane. There are four variants of this defect which have a circular shape projected as an ellipse on typical TEM micrographs taken on the (001) surface plane. The perfect dislocation loops have also been found to lie on {111}

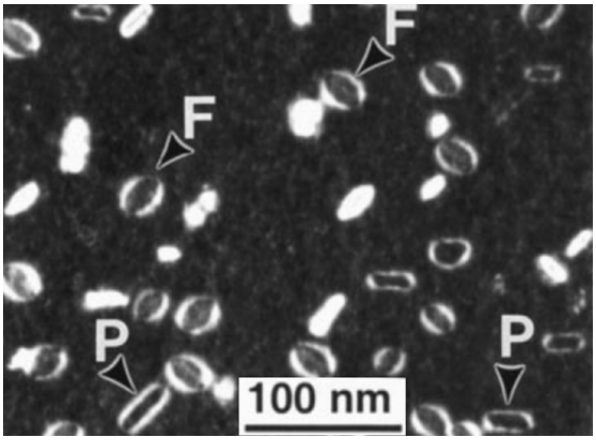

Figure 21 – Plan-view (400) WBDF TEM micrograph from a sample implanted with 150 keV Ge^+ ions to a dose of $2x10^{15}$ ions/cm^2 after RTA at 900°C for 10 sec in N_2.

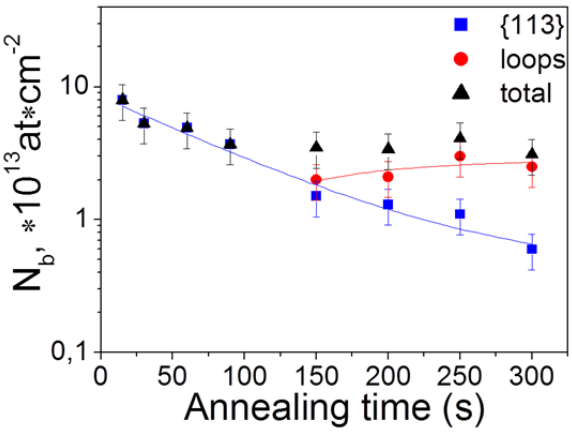

Figure 22 – Time evolution of the number of atoms stored in the different types of extended defects during annealing at 850°C following Si^+ implantation at 100 keV to a dose of $2x10^{14}$ cm^{-2}.

planes and have a Burgers vector of $(a/2)<110>$. They are elongated along that particular <110> direction on their habit plane which is perpendicular to the Burgers vector. Therefore, 12 variants of this defect exist. The formation of PDLs under similar conditions has also been reported in other published works where these defects have been named ''dislocation dipoles'' [47] or rectangular elongated dislocations [48].

An important aspect of DLs is that, similarly to the other defects types, they do not nucleate directly at the beginning of the annealing but they form upon transformation of already existing smaller/less stable defects into larger/more stable ones, in order to minimize their formation energy. In particular, it was proposed on the basis of *in-situ* TEM investigations [49] that PDLs and FDLs are the result of an unfaulting reaction of {311} defects. Due to the strong impact of such mechanism on the development of a comprehensive and reliable model of defect evolution, we focused our attention on this issue and performed some experimental studies with the aim of improving our understanding of the {311}-to-DL transformation. In section 1.4.1, we will therefore recall two of these works carried out within the PhD thesis of Pascal Calvo and the post-doctoral work of Simona Boninelli aiming at *(i)* identifying the conditions under which {311} defects can alternatively dissolve or transform into dislocation loops (DLs) [50] and *(ii)* investigating in detail the defect crystallographic structure during the {311}-to-DL transformation [51].

Once formed, FDLs and PDLs have been observed by different authors after different implantation and annealing conditions with sizes and proportions which strongly vary from one paper to the next. For example, after annealing of Ge-amorphised Si wafers at 1000°C for less than a minute, Bonafos *et al.* [14], observed only faulted dislocation loops while after comparable anneals of Si-implanted Si wafers Pan *et al.* [52] observed mostly perfect dislocation loops. Skarlatos *et al.* [53] have shown that, during oxidation, perfect loops grow faster than faulted loops, while Omri *et al.*[54] have shown that they dissolve faster if a free surface is put

closer to the defects. In order to elucidate how the relative thermal stability of PDLs and FDLs depends on the experimental conditions, we carried out a series of dedicated experiments [55] to study the influence of the ion dose, annealing ambient, and proximity of a free surface on the evolution of a population of defects composed of both types of loops. Through the calculation of the formation energy of both types of dislocations, we demonstrated that all these experimental studies can be explained using the concept of Ostwald ripening of two coexisting populations of interstitial defects, during which the competitive growth is achieved at the expense of the less energetically stable defect. The experimental details of these experiments (published in [55]) will not be presented here. Instead, in section 1.4.2, we will give the details of the calculation of the formation energy of PDLs and FDLs and a brief summary of its application to the interpretation of typical experiments.

1.4.1. Experimental studies: From {311}s to faulted and perfect DLs

In a first experiment [50], we quantitatively studied by (TEM) the effect of the annealing temperature on the structural evolution of {311} defects formed after high dose non-amorphising implants. A (100) Si wafer was implanted with Si^+ ions at 100 keV to a dose of $2x10^{14}$ ions/cm^{-2}. Following this implant, pieces of the wafer were annealed either at 800°C or at 850°C for times ranging from 5 s to 1 h under nitrogen.

Under such particular conditions, we could show how within a very limited range of temperatures, the {311} defects can dramatically change their thermal behaviour. At 800°C, they follow the typical dissolution kinetics already described in section 1.3.1 (page 20), i.e. they grow in size (up to ~170 nm) and decrease in density (more than 2 decades in 2h) before dissolving. In the meantime, the number of atoms they contain constantly decreases, typical of a non-conservative Ostwald ripening process.

In contrast, during annealing at 850°C, the defect behaviour was very different. In particular, while for short annealing times (< 150 s) only {311} defects were observed, for longer times a mixture of {311} defects and DLs was found. Finally, for long enough annealing times, only DLs survive. Figure 22 shows the evolution of the total number of Si atoms bound to the defects as a function of annealing time at 850°C. Surprisingly, the dissolution rate of the {311} defects seems to be unaffected by the appearance of DLs in the population for times larger than 150 s (squares in Figure 22). On the other hand, once DLs are formed, the whole defect population does not lose atoms anymore (triangles in Figure 22), clearly indicating that the atoms lost by the {311} defects are captured by the DLs. The latter therefore provide internal sinks within the population and transform the non-conservative Ostwald ripening into a quasi-conservative one. In the meantime, the flux of Si_{int} atoms towards the surface that drives the defect dissolution is suppressed and replaced by internal fluxes between defects of different types.

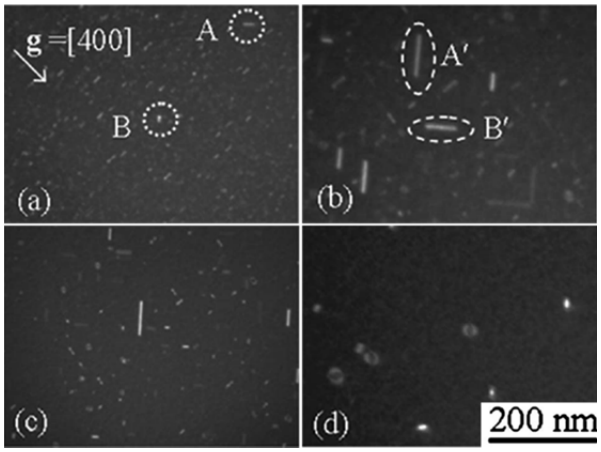

Figure 23 – Plan-view (400) WBDF TEM micrograph from a sample implanted with 30 keV Ge^+ ions to a dose of $1x10^{15}$ ions/cm^2 after RTA at 800°C for *(a)* 15 s, *(b)* 120 s, *(c)* 300 s and *(d)* 2700 s.

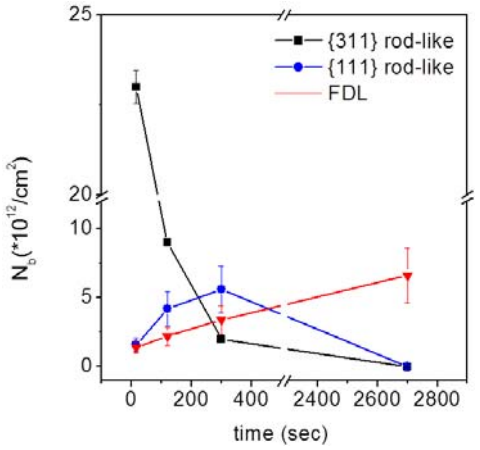

Figure 24 – Time evolution of the number of atoms stored in the different types of extended defects during annealing at 800°C following Ge^+ implantation at 30 keV to a dose of $1x10^{15}$ cm^{-2}.

Finally, it was found that the maximum size that {311} defects could reach at 850°C before transforming into DLs (80 nm) or at 800°C before dissolution (170 nm) are considerably larger than expected when considering the relative formation energy of the two types of defects (cf. next section). These results strongly suggest that the transformation from {311} defects to DLs defects to dislocation loops is thermally activated and takes place through a reaction barrier, this barrier reflecting the difficulty in rearranging the large number of Si atoms into a very different configuration without (too many) intermediate steps.

The detailed investigation of the defect crystallographic structure during the {311}-to-DL transformation, was the object of a second experiment [51], in which we demonstrated that an "intermediate" rod-like defect forms during the transformation of {311}s into DLs. For this, a Si (001) wafer was amorphised to a depth of 50 nm with a 30 keV Ge^+ implant to a dose of $1x10^{15}$ cm^{-2}. Annealing was then performed at 800°C for times ranging from 15 to 2700 s.

Figure 23 reports four plan-view images of samples annealed for 15 s *(a)*, 120 s *(b)*, 300 s *(c)* and 2700 s *(d)*. The white arrow in *(a)* indicates the direction of the diffraction vector $\boldsymbol{g}$= [400] used for these images. Figure 23a shows that after 15 s only rod-like defects are formed (no DLs). A similar result is found after 120 s (Figure 23b), with a reduced density (and increased size) of the observed defects. After 300 s (Figure 23c), a further reduction of the defect is found, which is accompanied by the appearance of a few dislocation loops (FDLs). Finally, after 2700 s, only FDLs are observed, indicating that the transformation of {311}s into DLs is complete.

However, according to the diffraction contrast theory, only the rod-like defects elongated on a direction perpendicular to the diffraction vector $\boldsymbol{g}$ (i.e. the vast majority in Figure 23a) correspond to conventional {311} defects. In contrast, defects such as those labeled "A" and "B" in Figure 23a are elongated along [110] and [-110] directions (i.e., at 45° with respect to the **g** vector). They do not behave as

conventional {311}s owing to their unpredicted very high contrast and must therefore have different crystallographic characteristics.

A detailed TEM investigation of these "unconventional" rod-like defects, made using different diffraction vectors and sample zone axes, allowed to conclude that a Burgers vector parallel to the <111> direction can accurately explain their contrast behaviour. In addition, it was found that they are elongated along <110> directions and lie on {111} planes. They are therefore referred to as {111}-RL defects. Further analysis allowed to distinguish their contrast behaviour from that exhibited by Perfect Dislocation which have the same habit plane and elongation but a different Burgers vector (parallel to <110> for PDLs). Finally, it is important to note that, applying the diffraction contrast theory to previous *in-situ* TEM investigations of the {311}-to-DL transformation [49], it appears that the rod-like defects found to transform into DLs in that work are not the {311}s but rather the {111}-RL defects shown in Figure 23.

We completed our study by carrying out a quantitative analysis of the defect evolution, by which the density, mean size, and the concentration of atoms trapped in the defects, N_b, were measured as a function of the annealing time. The time evolution of N_b is reported in Figure 24 and indicates that between the shortest anneal time (15 s), when all the excess interstitial atoms are contained in {311} defects (black squares in Figure 24) and the longest one (2700 s) when they are all contained in DLs (red triangles in Figure 24)[#], it exists an intermediate annealing time (300 s) at which the majority of the excess interstitials (~50%) is transferred to the {111}-RL defects. We could therefore propose that the unfaulting reaction leading to the transformation of {311}s into DLs must include the formation of these intermediate defects.

1.4.2. Modelling

Dislocation loops are found to appear in two forms: Frank dislocation loops (FDLs) and Perfect dislocation loops (PDLs). The calculation of their formation energy according to their crystallographic characteristics is given below [55].

For a FDL of radius r the total energy $E_{T\text{-}FDL}(r)$ is given by the sum of the elastic energy of the dislocation line, E_{el}, and the stacking fault energy E_{SF}:

$$E_{T-FDL}(r) = E_{el} + E_{fault} = \frac{\mu r}{4}\left[\frac{2a^2}{3(1-\nu)}\right] ln\left(\frac{2r}{r_0}\right) + \gamma\, \pi r^2 \qquad (14)$$

[#] The total number of Si_{int} atoms contained in the defects initially decreases and, as soon as DLs are formed it stabilises to a constant value, similarly to our previous investigations (cf. Figure 22).

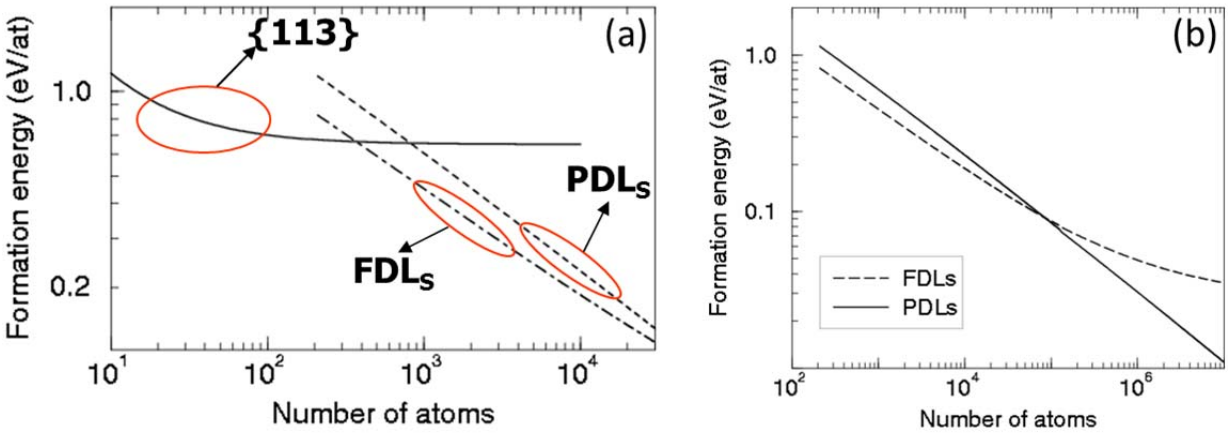

Figure 25 – Formation energy of {311} defects and DLs plotted as a function of the number of atoms they contain. (a) Transition of {311}s into DLs is expected for sizes around 400 atoms. (b) PDLs are lire energetically stable than FDLs for sizes larger than ~80000 atoms (corresponding to a radius of ~40 nm)

where γ is the stacking fault energy per unit area (70 mJ/m^2 or 0.027 eV/at), μ is the shear modulus (7.55x10^{10} N/m^2), a is the lattice parameter (0.543 nm), ν the Poisson ratio (0.3), and r_0=b/4 the dislocation core radius, b being the modulus of the Burgers vector (3.13 nm). The number of atoms in the loop $n_{DL}(r)$ is related to its radius by:

$$n_{DL}(r) = \pi r^2 d_{111} \tag{15}$$

where d_{111} is the atomic density of {111} planes (1.57x10^{15} at/cm^2).

A similar approach can be followed to evaluate the formation energy of a PDL. However, the calculations are based on the assumption that PDLs also have a circular shape. Under this assumption and considering that no stacking fault is associated with the defect, the total energy $E_{T\text{-}PDL}(r)$ can be written as follows:

$$E_{T-PDL}(r) = E_{el} = \frac{\mu r}{4}\left[\frac{a^2}{6} + \frac{5a^2}{6(1-\nu)}\right] ln\left(\frac{2r}{r_0}\right) \tag{16}$$

Using eq. 14 and 16, the energies of the two DL types can be written as a function of the number of atoms, n, they contain. Their derivative with respect to n finally provides their formation energies, which are shown in Figure 25. Comparison with the formation energy of {311} defects (Figure 25a) indicates that for sizes exceeding ~350 atoms, {311}s are expected to transform into faulted and perfect DLs which exhibit a lower formation energy, in agreement with the experiments reported in the previous subsection. When comparing the formation energy of perfect and faulted DLs (Figure 25b), it appears that for dislocation loops of the same size, FDLs are more energetically stable than PDLs for sizes lower than 80000 atoms (corresponding to a radius of ~40 nm) and vice versa. In practice, for a given implant and annealing condition, the two defect families generally exhibit different size distributions, so that the stability inversion can occur either below or above this threshold value, depending on the experimental conditions and in a way that is difficult to predict.

We therefore calculated the formation energy of observed DLs populations for a variety of experiments [55], including *(i)* conservative DL ripening with different values of the initial concentration of excess Si_{int} atoms and *(ii)* non-conservative

ripening induced by either surface proximity (decrease of the number of atoms contained in the DLs during annealing, N_b) or by oxidizing annealing conditions (increase of N_b). In all cases we showed that all these experiments can be explained using the concept of Ostwald ripening of two coexisting populations of interstitial defects, provided the formation energies of the defects are known.

In most technologically relevant cases for USJ fabrication (very low implant energies and high temperature anneals), FDLs appear to be the "dominant" DL family. In view of extending the predictive model for defect and TED evolution to the formation of large DLs, only FDLs were therefore considered.

The calculation of the capture efficiency $\frac{A_n}{R_{eff}}$ for FDLs was based on the work of Bonafos [56]. The dislocation line surrounding the stacking fault can be represented by a torus with a core radius r_c (usually taken equal to the Burgers vector, $\boldsymbol{b}$, of the dislocation) and a loop radius r. $\frac{A_n}{R_{eff}}$ can therefore be written as

$$\frac{A_n}{R_{eff}} = 4\pi r_{eff} \qquad \text{with} \qquad r_{eff} = \frac{\pi(r^2 - r_c^2)^{\frac{1}{2}}}{ln\left(\frac{8r}{r_c}\right)} \approx \frac{\pi r}{ln\left(\frac{8r}{r_c}\right)} \tag{17}$$

for $r >> r_c$ [14].

The resulting $\frac{A_n}{R_{eff}}$ for FDLs is shown in Figure *26* (cyan squares, *n>100*), together with the capture efficiency of small ICs (red circles) and {311} defects (green triangles) discussed in section 1.3.2. The discontinuities in the "global" $\frac{A_n}{R_{eff}}$ curve (blue line) correspond to the formation energy transitions from small interstitial clusters to {311}s (n=10, cf. Figure 16) and from 311s to FDLs (n~350, cf. Figure 25b).

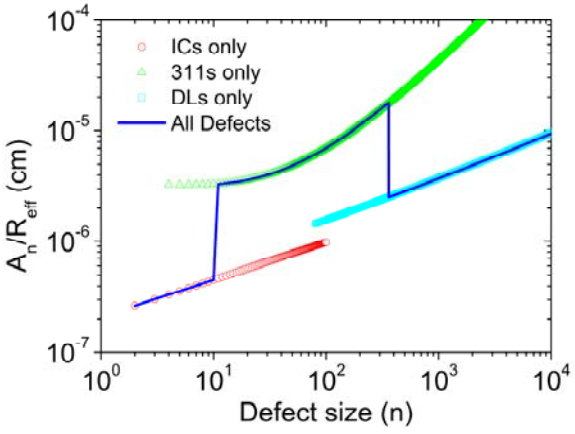

Figure 26 – Variation of the capture efficiency A_n/R_{eff} of clusters, {311} defects and dislocation loops as a function of the number of Si atoms they contain.

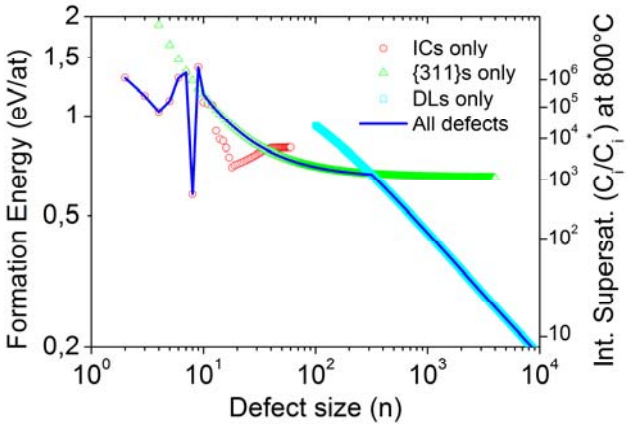

Figure 27 – Formation energy (left axis) of the different types of extended defects as a function of their size and corresponding values of the Si_{int} supersaturation in equilibrium with the defects, cf. eq. 9 (right axis).

Once the values of $\frac{A_n}{R_{eff}}$ and $E_f(n)$ were determined for the DLs, it was possible to test the model against existing studies on the evolution of TED in their presence during annealing [25]. Figure 28 reports the Si_{int} supersaturation measured during the transformation of {311} defects into DLs (cf. Figure 22), from the diffusion enhancement of Boron marker layers located in the vicinity of the defect layer. The Si_{int} supersaturation is found to continuously decrease during annealing (Figure 28a) to values largely lower than those expected in the presence of {311} defects (~250 in the time interval 200-300 s) and still higher than equilibrium. In Figure 28b, the experimental data are compared to simulations that include the {311}s-to-DLs transformation for sizes above 350 atoms (black dashed line). This experiment is perfectly reproduced, once the average diffusion enhancements corresponding to the experimental time intervals are calculated (red circles). For comparison, Figure 28b reports the simulation curve obtained without including DLs in the model. In this case the Si_{int} supersaturation should remain at high level for much longer time before the dissolution of {311} defects.

Further successful tests of the TED prediction in the presence of dislocation loops were run in the case of ultra-shallow junctions fabricated by low energy Boron implantation (1 keV) into pre-amorphised Si [57,58] and annealed at high temperatures (from 950°C to 1050°C), when the measured Si_{int} supersaturation is much lower (between 5 and 10) but still controlled by the extended defects induced by the implant.

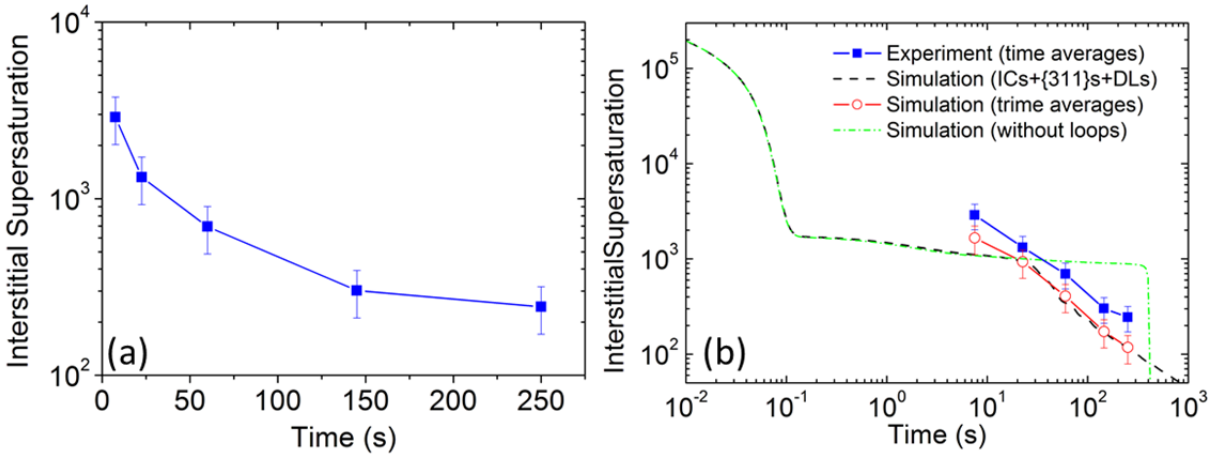

Figure 28 – (a) Diffusion enhancement of B marker layers as a function of annealing time, following Si implantation at 100 keV to a dose of $2x10^{14}$ cm^{-2} and annealing at 850°C. (b) Comparison with simulations. Squares: experiment. Black line: simulation (time dependence). Circles: simulations (average values corresponding to the experimental time intervals). Green line: simulation (without including dislocation loops).

1.5. Predictive simulations of extended defects and TED

Previous sections 1.2-1.4 have shown how it was possible, on the basis of the Ostwald ripening mechanism, to explain *(i)* the formation and evolution of all different types of extended defects as a function of the experimental conditions, and *(ii)* Boron TED evolution in the presence of extended defects.

As discussed in section 1.1.3 (p.11), the main physical parameter describing the link between TED and defect evolution is the defect formation energy (cf. eq. 10). A "global" description of the formation and evolution of all defect types, based on this parameter and its implications in TED evolutions will be summarised in section 1.5.1.

A similarly important aspect for the interpretation of defects and TED experiments, already mentioned in previous sections, is the proximity of the surface to the damage region. A dedicated experiment for the direct measurement of this effect will be recalled in section 1.5.2.

Finally, we will briefly describe in section 1.5.3 how this model was improved in view of its integration into state-of-the-art commercial TCAD simulators. This included its coupling with 1-D dopant and point defect diffusion and the reduction of the computing time.

1.5.1. Global description of defect evolution

The formation energies of all defect types are plotted in Figure 27 (left axis), according to the calculations described in sections 1.2-1.4. These curves allow to explain why, for extremely small defect sizes (less than 10 atoms), the {311} defect configuration (green triangles in Figure 27) is not energetically favourable compared to small interstitial clusters with an "oscillating" formation energy (red circles). From these curves it is also evident why large {311} defects are expected to transform into more stable dislocation loops (cyan squares). All the intriguing characteristics of the concomitant thermal behaviour of all these defects can be understood from this figure. For example, a {311} defect of 2000 atoms can be a sink for Si_{int} atoms emitted by a small interstitial cluster but also a source of interstitials for a dislocation loop of the same size.

For a given annealing temperature, the Ostwald ripening of such defects maintains in the region a supersaturation which decreases as the formation energy of the extended defects decreases (cf. eq. 9). For example, we have plotted on the right vertical axis of Figure 27 the supersaturation S_I of Si_{int} atoms in dynamical equilibrium with these defects at 800°C. Keeping in mind that the enhanced diffusivity of an "interstitial" dopant such as Boron is directly proportional to this supersaturation (cf. eq. 2), this curve also shows a hierarchy of levels of non-equilibrium diffusion, ranging from diffusion enhancements of ~10^6 in the presence of small clusters through ~10^4 in the presence of {311} defects and down to less than 10^3 when dislocation loops are finally formed.

1.5.2. Surface effect

As mentioned in section 1.2.2 the atomistic model for defect evolution assumes that the silicon surface is an efficient recombination site for Si interstitial atoms diffusing out from the defect region. This implies that a gradient of the depth distribution of the Si interstitial supersaturation exists between the defect region and the surface, as schematically shown in Figure 29. The consequent interstitial flux from the defects to the surface is finally responsible for the complete defect dissolution during thermal annealing. This picture is based on previous experiments in which the presence of such gradient was assumed to explain the evolution of extended defects [59] or the time behaviour of boron diffusion [29]. We therefore carried out a dedicated experiment to provide a direct experimental evidence of the existence of this gradient [60]. For this, we used Si structures containing several boron marker layers, in order to evaluate the Si interstitial supersaturation at different depths in the substrate.

Figure 30a shows boron profiles measured in the as-grown structure and after annealing at 850°C for 15 s and 300 s, following a Si^+ implantation at 100 keV to a dose of $2x10^{14}$ cm^{-2}. Of the four boron marker layers, only the second one at 0.4 μm is located within the defect region. A qualitative analysis of the SIMS profiles clearly indicates that the deep marker layers (at 0.7 μm and 1 μm, respectively) diffuse more than those located closer to the surface. A fitting method based on the interstitial kick-out mechanism of B diffusion [6] was then used to extract the diffusion enhancement, D_B/D_B^*, corresponding to each B marker layer for all the investigated annealing time intervals. The results are reported in Figure 30b, where the variation of the diffusion enhancement is reported as a function of depth for each time interval. It was found that for all annealing times the diffusion enhancement is highest for the two deepest delta layers (located below the defect band) and gently decreases towards the surface. Considering eq. 2 (p. 9), this figure therefore represents a direct measurement of the interstitial supersaturation gradient between the defect band and the surface. In addition, the extrapolation of the Si_{int} supersaturation level above the silicon surface (cf. Figure 29) allowed the estimation of the surface recombination length, L_{surf}, i.e. the mean free path travelled on the surface by a Si interstitial atom before recombining. Our results indicated an upper limit of about 200 nm for the surface recombination length at an annealing temperature of 850°C, in agreement with the values proposed by previous TED simulation studies [58,61]

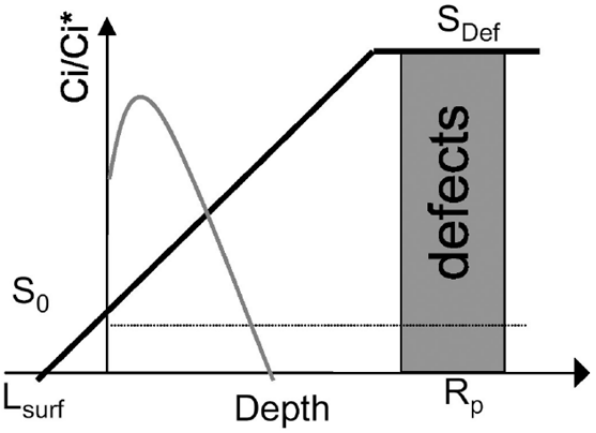

Figure 29 – Expected depth variation of the amplitude of the Si_{int} supersaturation in the region between the defect layer and the surface.

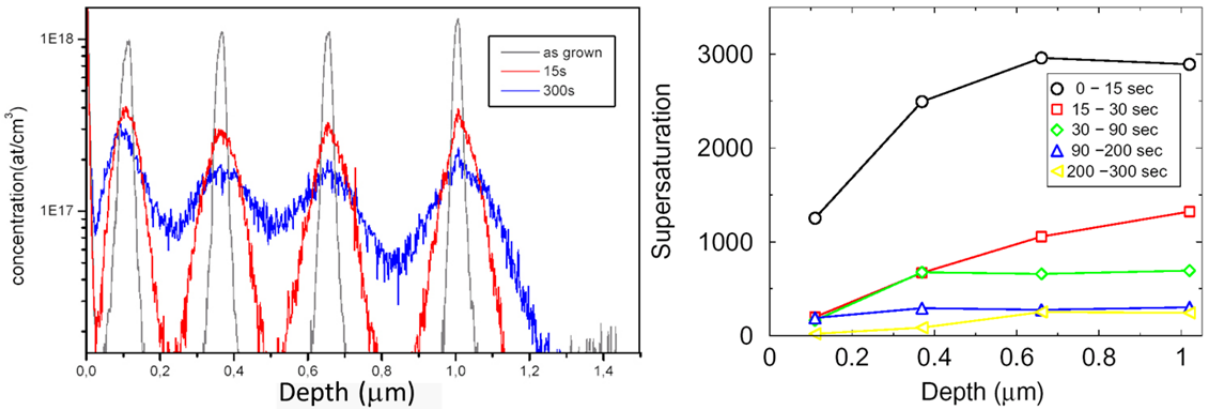

Figure 30 – *(a)* Boron depth distribution profiles following Si^+ implantation at 100 keV to a dose of $2x10^{14}$ cm^{-2} and annealing at 850°C. *(b)* Diffusion enhancement of B marker layers during annealing at 850°C following Si^+ implantation at 100 keV to a dose of $2x10^{14}$ cm^{-2}. (From Ref. 60)

1.5.3. Implementation into a commercial simulator

On the basis of the successful simulations of defects and Boron TED evolution rendered possible by the atomistic model presented in section 1.2.2, further work was carried out within the European project FRENDTECH (2001-2004) by several collaborators in order to implement it into the commercial simulator ISE-FLOOPS (today SYNOPSYS-Sentaurus Process [62]). The main aspects of this "optimisation" activity are briefly summarised in this section for the sake of completeness in the presentation of the outcomes of this research activity.

First of all, it is important to note that, although it correctly takes into account the surface recombination length (as shown in previous section), the model remained a 0-dimensional one, whereby the totality of the defects is located in a single point. While allowing to successfully simulate the Boron diffusion enhancement in various experiments, the model needed to be coupled to point defect and dopant diffusion equations in order to provide a direct comparison with experimental Boron concentration profiles obtained by SIMS.

A first demonstration of the coupling between the defect model and diffusion simulations was provided by Lampin *et al.* [58] who used the process simulator IMPACT (developed at IEMN-CNRS Lille) to reproduce the Boron TED experiment discussed in previous section (cf. Figure 30). The comparison between the measured and simulated Boron concentration profiles of the four marker layers, after a 30 s anneal at 850°C is shown in Figure 31a. The agreement between the calculated and measured profiles is evident. The calculated depth concentration profile of free Si_{int} atoms is also reported in the figure. Its flat shape below the defect region (located at ~300 nm) is the result of the assumption that no Si_{int} traps are present in the bulk of the high-quality CVD layers used in this experiment. The good agreement with the measured B profiles clearly justifies this choice. On the other hand, the gradient in the Si_{int} concentration profile between the defect region and the surface exhibits a

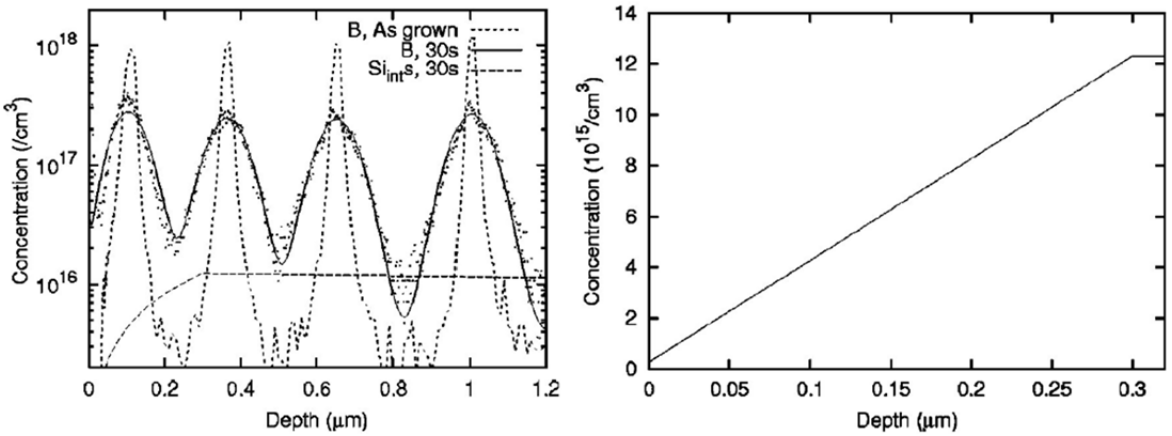

Figure 31 – *(a)* Boron depth distribution profiles following Si^+ implantation at 100 keV to a dose of $2x10^{14}$ cm^{-2} and annealing at 850°C. *(b)* Diffusion enhancement of B marker layers during annealing at 850°C following Si^+ implantation at 100 keV to a dose of $2x10^{14}$ cm^{-2}. (From Ref. 58)

linear decrease (see Figure 31b plotted using a linear concentration scale), therefore validating our description for the surface recombination mechanism (cf. Figure 29).

A similar coupling of the defect model presented above with a 1-D Boron and point defect diffusion simulation was also carried out at FhG-IISB Erlangen by Christophe Ortiz and Peter Pichler, using the PDE solver PROMIS 1.5 [26]. In addition to several Boron diffusion experiments, this 1-D model was used to simulate the depth distribution of {311} defects presented in section 1.3.1 (cf. Figure 14 p. 21), which is impossible to simulate with the 0-D model. As evidenced by Figure 32, the 1-D model is able to predict the overall defect density decrease due to Ostwald Ripening of the defects, but also the shift of the defect depth distribution towards larger depths for long annealing times. This last result is a consequence of the preferential dissolution of defects located near the surface, where interstitials rapidly recombine.

The final issue to be solved prior to the transfer of the defect model to a commercial process simulator consisted in the reduction of the computation time for the simulation of the extended defect evolution. As shown in section 1.2.2, the calculation of the defect size distribution and of the supersaturation of free Si_{int} atoms at any time during annealing requires the solution of a system of $n+1$ differential equations, where n is the maximum defect size (typically equal to 10^4 for a reliable calculations that includes large dislocation loops). In the method proposed by Lampin *et al.* [63], it was assumed that for {311} defects and dislocation loops, that exhibit a monotonically slow decrease of the formation energy as a function of defect

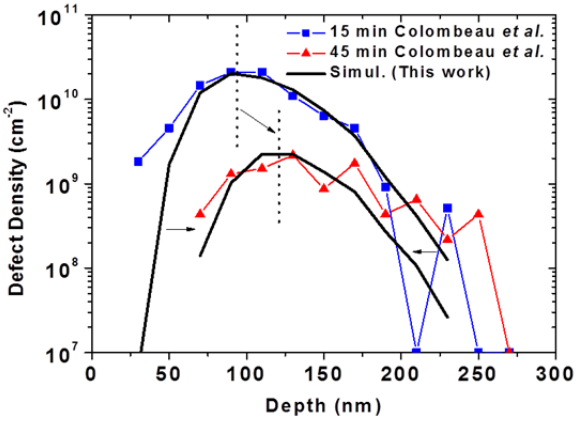

Figure 32 – Time evolution of the mean depth of the defects formed by 40 keV, $6x10^{13}$ cm^{-2} Si implant annealed at 740 °C. The mean depth increases with time. (From Ref. 26)

size, the discrete nature of the defect growth mechanism (dynamic equilibrium between capture and emission of free Si_{int} atoms) is unimportant and the whole process described by the master equation 4 (p. 15) can be accurately approximated by a Fokker-Planck equation, based on the truncated Taylor expansion of the master equation. By keeping only the first two terms, it was shown that the size of the system could be reduced from 10,000 to 32 equations keeping not only an accurate description of the Si_{int} supersaturation maintained by the extended defects but also the more ''reduction sensitive'' values of the density of defects and of the total number of atoms trapped in the defects.

The model optimisations described above finally allowed in 2004 the transfer of the defect model towards the commercial TCAD simulator FLOOPS-ISE (today Synopsys Sentaurus Process [62]) where it is available as the "FRENDTECH defect model", together with a "moment"-based model [64,65] in which the number of differential equations has been further reduced to seven.

1.6. Conclusions

The results presented in this chapter cover a period going from 1998 to 2005. They were obtained in close collaboration with the "ion implantation" group at CEMES that I first joined as a post-doctoral researcher and with which I continued to collaborate by co-supervising three PhD students and coordinating the work of two post-doctoral researchers.

Our contribution to the understanding and modelling of dopant Transient Enhanced Diffusion in the presence of implantation-induced extended defects was twofold and can be summarised as follows:

- On the experimental side, we succeeded in providing a **unified description of implantation-induced defect evolution**, explaining why, depending on the implant and annealing conditions, a given defect type is formed, why it dissolves during annealing or transforms into a larger defect with different crystallographic characteristics and how it evolves in the presence of different defect types.
- Concerning **defect and dopant diffusion modeling**, our work on the calculation of the defect formation energy and the capture efficiency allowed to improve the existing models by extending them to all defect families, including a correct TED dependence on the defects' size distributions.

Finally, our work strongly contributed to establish the state-of-the-art in this domain and served as a reference for the development of simplified models, compatible with the computing time requirements of commercial TCAD simulators.

1.7. References

[1] J.W. Mayer, L. Eriksson, J.A. Davies: Ion Implantation in Semiconductors (Academic Press, New York, London 1970

[2] W.K. Hofker, H.W. Werner, D.P. Oosthoek, H.A.M. de Grefte, Appl. Phys. 2 (1973) 265

[3] S. J. Pennycook, J. Narayan and O. W. Holland, Mat. Res. Soc. Symp. Proc., 27 (1983) 293

[4] A.E. Michel, W. Rausch, P.A. Ronsheim, R.H. Kastl, Appl. Phys. Lett. 50 (1987) 416

[5] P.M. Fahey, P.B. Griffin, J.D. Plummer, Rev. Mod. Phys, 61 (1989) 289

[6] N.E.B. Cowern, K.T.F. Janssen, G.F.A. van de Walle, and D.J. Gravesteijn, Phys. Rev. Lett., 65 2434 (1990)

[7] H.-J. Gossmann, Proc. Of the Electrochem. Soc. V. 98-1 (1998) p. 884

[8] J.W. Corbett, J.P. Karins, T.Y. Tan, Nucl. Instr. and Meth. B, 182–183 (1981) 457

[9] A.F. Leier, L.N. Safranov, G.A. Kachurin, Semiconductors 33

(1999) 380

[10] N.E.B. Cowern, G.F.A. van de Walle, P.C.Zalm, and D.W.E. Vandenhoudt, Appl. Phys. Lett., 65 (1994) 2981

[11] D. J. Eaglesham, P. A. Stolk, H.-J. Gossmann, and J. M. Poate, Appl. Phys. Lett., 65 2305 (1994)

[12] C.S. Rafferty, G.H.Gilmer, M. Jaraiz, D. Eaglesham and H.-J. Gossmann, Appl. Phys. Lett. 68 (1996) 2395

[13] C. Bonafos, M. Omri, B. de Mauduit, G. Ben Assayag, A. Claverie, D. Alquier, A. Martinez and D. Mathiot, J. Appl. Phys. 82 (1997) 2855

[14] C. Bonafos, D. Mathiot and A. Claverie, J. Appl. Phys., 83 (1998) 3008

[15] L.H. Zhang, K.S. Jones, P.H. Chi, D. S. Simons, Appl. Phys. Lett. 67 (1995) 2025

[16] E. Napolitani, A. Carnera, E. Schroer, V. Privitera, F. Priolo, S. Moffatt, Appl. Phys. Lett. 75 (1999) 1869

[17] E. Napolitani, A. Carnera, V. Privitera, E. Schroer, G. Mannino, F. Priolo, S. Moffatt, Mat. Res. Soc. Symp. Proc., 610 (2000) B5.2

[18] H.G.A. Huizing, C.C.G. Visser, N.E.B. Cowern, P.A. Stolk, R.C.M. de Kruif, Appl. Phys. Lett. 69 (1996) 1211

[19] N. Cowern, G. Mannino, P. Stolk, F. Roozeboom, H.Huizing, J. van Berkum, W. de Boer, F. Cristiano, A.Claverie, M. Jaraiz, Phys. Rev. Lett., 82 (1999) 4460

[20] G. Hobler and C.S. Rafferty, Mat. Res. Soc. Symp. Proc., 568 (1999) 123

[21] L. Kampmann, M. Kahlweit, Ber Bunsenges Physik. Chem., 72 (1970) 456

[22] M. Flynn; Point Defects and diffusion. Clarendon Press, Oxford (1972)

[23] C. Bonafos, B. Colombeau, A. Altibelli, M. Carrada, G. Ben Assayag, B. Garrido, M. Lopez, A. Perez-Rodriguez, J.R. Morante, A. Claverie, Nucl. Inst. Meth. Phys. Res. B 178 (2001) 17

[24] P. A. Stolk, H.-J. Gossmann, D. J. Eaglesham, D. C. Jacobson, C. S. Rafferty, G. H. Gilmer, M. Jaraiz, J. M. Poate, H. S. Luftman, and T. E. Haynes, J. Appl. Phys., 81 6031 (1997)

[25] Y. Lamrani, PhD thesis, University of Toulouse, 2005

[26] C.J. Ortiz, P. Pichler, T. Fühner, F. Cristiano, B. Colombeau, N.E.B. Cowern and A. Claverie, J. Appl. Phys., 96 (2004) 4866

[27] A. Claverie, B. Colombeau, B. de Mauduit, C. Bonafos, X. Hebras, G. Ben Assayag, F. Cristiano, Appl. Phys. A, 76 (2003) 1025

[28] K. Moller, K. Jones, and M. Law, Appl. Phys. Lett., 72 (1998) 2547

[29] D. Lim, C. Rafferty and F. Klemens, Appl. Phys. Lett., 67 (1995) 2302

[30] S. Takeda, M. Kohyama and K. Ibe, Phil. Mag. A, 70 (1994) 287

[31] A.H. Gencer and S.T. Dunham, J. Appl. Phys., 81 631 (1997)

[32] M. Jaraiz, L. Pelaz, E. Rubio, J. Barbolla, G.H. Gilmer, D.J. Eaglesham, H.J. Gossmann and J.M. Poate, Mat. Res. Soc. Symp. Proc., 532 (1998) 43

[33] M. Seibt, J. Imschweiler and H.A. Hefner, Mat. Res. Soc. Symp. Proc., 316 (1994) 167

[34] F. Cristiano, N. Cherkashin, X. Hebras, P. Calvo, Y. Lamrani, E. Scheid, B. de Mauduit, B. Colombeau, W. Lerch, S. Paul, A. Claverie, Nucl. Inst. Meth. B, 216 (2004) 46

[35] N. Cherkashin, P. Calvo, F. Cristiano, B. de Mauduit and A. Claverie, Mat. Res. Soc. Symp. Proc., 810 (2004) 103

[36] B. Colombeau, N.E.B. Cowern, F. Cristiano, P. Calvo, N. Cherkashin, Y. Lamrani and A. Claverie, Appl. Phys. Lett., 83 (2003) 1953

[37] B. Colombeau, PhD Thesis, University of Toulouse, 2001

[38] C.A. Ferreira Lima and A. Howie, Phil. Mag. 34 (1976) 1057

[39] S. Takeda Jpn. J. Appl. Phys. 30, L639 (1991).

[40] P. Calvo, PhD Thesis, University of Toulouse, 2004

[41] F. Cristiano, B. Colombeau, Y. Lamrani, B. de Mauduit and A. Claverie, Deliverable D306, FRENDTECH EU Project, August 2002

[42] A.H. Gencer, S.T. Dunham, J. Appl. Phys. 81 (1997) 631

[43] B. Colombeau, F. Cristiano, A. Altibelli, C. Bonafos, G. Ben Assayag, A. Claverie, Appl. Phy. Lett., 78 (2001) 940

[44] R. Bicknell, J. of Microsc. 98 (1973) 165

[45] M.L. Jenkins, D.J.H. Cockayne, M.J. Whelan, J. of Microsc. 98 (1973) 155

[46] B. de Mauduit, L. Laânab, C. Bergaud, M.M. Faye, A. Martinez, A. Claverie, Nucl. Inst. and Meth. in Phys. Res. B 84 (1994) 190

[47] M. Seibt, J. Imscheliweiller, and H. A. Hefner, Mater. Res. Soc. Symp. Proc. 316 (1994) 167.

[48] R. Raman, M. E. Law, V. Krishnamoorthy, and K. S. Jones, Appl. Phys. Lett. 74 (1999) 700

[49] J. Li and K. S. Jones, Appl. Phys. Lett. 73 (1998) 3748

[50] P. Calvo, A. Claverie, N. Cherkashin, B. Colombeau, Y. Lamrani, B. de Mauduit, and F. Cristiano, Nucl. Instrum. Methods Phys. Res. B 216 (2004) 173

[51] S. Boninelli, N. Cherkashin, A. Claverie and F. Cristiano, Appl. Phys. Lett. 89 (2006) 161904

[52] G. Z. Pan, K. N. Tu, and A. Prussin, J. Appl. Phys. 81 (1997) 78

[53] D. Skarlatos, M. Omri, A. Claverie, and D. Tsoukalas, J. Electrochem. Soc. 146 (1999) 2276

[54] M. Omri, C. Bonafos, A. Claverie, A. Nejim, F. Cristiano, D. Alquier, A. Martinez, and N. E. B. Cowern, Nucl. Instr. and Meth. Phys. Res. B 120 (1996) 5

[55] F. Cristiano, J. Grisolia, B. Colombeau, M. Omri, B. de Mauduit, A. Claverie, F. Giles, N.E.B. Cowern, J. Appl. Phys. 87 (2000) 8420

[56] C. Bonafos, PhD Thesis, University of Toulouse, 1996

[57] F. Cristiano, B. Colombeau, C. Bonafos, J. Aussoleil, G. Ben Assayag and A. Claverie, Proc. SISPAD 2001 Int. Conf., D.Tsoukalas and C.Tsamis ed., Springer-Verlag Wien, 2001, p. 30

[58] E. Lampin, F. Cristiano, Y. Lamrani, A. Claverie, B. Colombeau and N.E.B. Cowern, J. Appl. Phys., 94 (2003) 7520

[59] M. Omri, B. de Mauduit and A. Claverie, Mat. Res. Soc. Symp. Proc., 568 (1999) 219

[60] Y. Lamrani, F. Cristiano, B. Colombeau, E. Scheid, P. Calvo, H. Schafer and A. Claverie, Nucl. Instr. Meth. in Phys. Res. B, 216 (2004) 281-285

[61] N.E.B Cowern, D. Alquier, M. Omri, A. Claverie and A. Nejim, Nucl. Instr. Meth. in Phys. Res. B, 148 (1999) 257-261

[62] Sentaurus Process User Guide, (Synopsys, Inc., Mountainview, CA, 2010)

[63] E. Lampin, C. J. Ortiz, N. E. B. Cowern, B. Colombeau, F. Cristiano, Solid State Electronics, 49 (2005) 1168

[64] C. Zechner, N. Zographos, D. Matveev, A. Erlebach, Mat. Sci. Eng. B 124-125 (2005) 401

[65] N. Zographos, C. Zechner, I. Avci, Mat. Res. Soc. Symp. Proc., 994 (2007) 297

Chapter 2

Implant defects and dopant activation anomalies

As it was presented in the Introduction, the figures of merit of source/drain shallow junctions are the junction depth, x_j, and the sheet resistance, R_S, that are required to be sufficiently low to reduce the short channel effects and the transistor external resistance, respectively. These two parameters are not independent, as indicated by the following equation describing the sheet resistance of an ideal box-like junction:

$$R_S = \frac{1}{q\, x_j N_A \mu} \qquad (1)$$

In previous chapter, we discussed the role of defect-dopant interactions at the origin of diffusion anomalies that represented a major roadblock for the reduction of the junction depth, x_j. Here, we will focus on the defect-dopant interactions causing dopant activation anomalies, which have a strong impact on the active dose, N_A, and is some cases, also on the carrier mobility, μ. In the case of p^+-n junctions formed by Boron implantation, these anomalies are due to the formation of small Boron-Interstitial Clusters (BICs), which are the object of the studies presented in this chapter. For this activity, the experimental techniques of SIMS and TEM, which were extensively used in previous chapter, have been accompanied by the systematic use of electrical characterisation methods, mainly for the measurement of the sheet resistance or for the measurement of carrier mobility and active dose.

After recalling some previous results that describe the context in which our research was carried out, we will present our investigations on the dopant deactivation phenomenon induced by defect dissolution (section 2.2) and on the methods for reducing it (section 2.3). The trapping of Boron atoms by End-of-Range (EOR) defects will be discussed in section 2.4, while in section 2.5 we will report the impact of high concentrations of BICs on hole mobility. Finally, we investigated (section 2.6) the conditions under which BICs can grow up to large sizes that allow them to be directly observed by TEM analysis.

2.1. Background

2.1.1. Dopant activation: BICs formation and Boron precipitation

Dopant atoms need to occupy substitutional sites in the silicon lattice in order to be electrically active, i.e. by providing electrons or holes for conduction. This is schematically shown in Figure 1 (a), where the impurity atom (red sphere) occupies a

lattice position. However, after an ion implant step, the silicon lattice is highly damaged and most of the impurities occupy interstitial (electrically inactive) positions (cf. Figure (b), while a high amount of both Si self-interstitials (Si_{intS}) and vacancies are also generated during the implant (cf Figure 1 (c) and (d)). This is why an annealing step is necessary to recover the damage and activate the dopant atoms by placing them in substitutional position.

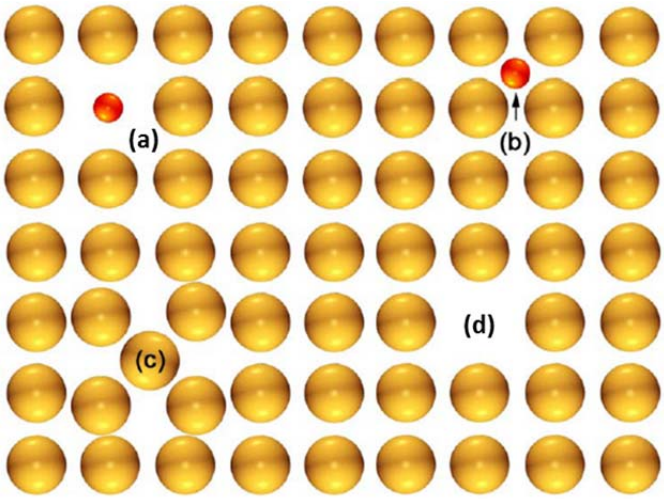

Figure 1 – Schematic illustration of the elementary point-defects existing in cristalline silicon: (a) substitutional impurity, (b) interstitial impurity, (c) self-interstitial, (d) vacancy.

According to equation (1), the increase of active dose N_A is one of the solutions allowing a reduction of the junction sheet resistance. This is simply achieved by increasing the implant dose. However, it was clear since the earliest 1970s [1,2] that, depending on the implant and annealing conditions, a critical concentration value, C_{el}, exists above which the implanted dopant is not electrically active.

This is shown in Figure 2 for the case of p^+-n junctions obtained by B^+ implantation. The figure (top row) reports Boron SIMS profiles measured after implant at 70 keV with three different doses (grey highlighted curves) and after annealing for 35 min at different temperatures. The highlighted annealed curves (800°C red, 900°C blue) clearly indicate that Boron atoms are immobile at the highest concentrations, while they rapidly diffuse at lower ones. The two profile regions are separated by a "kink".

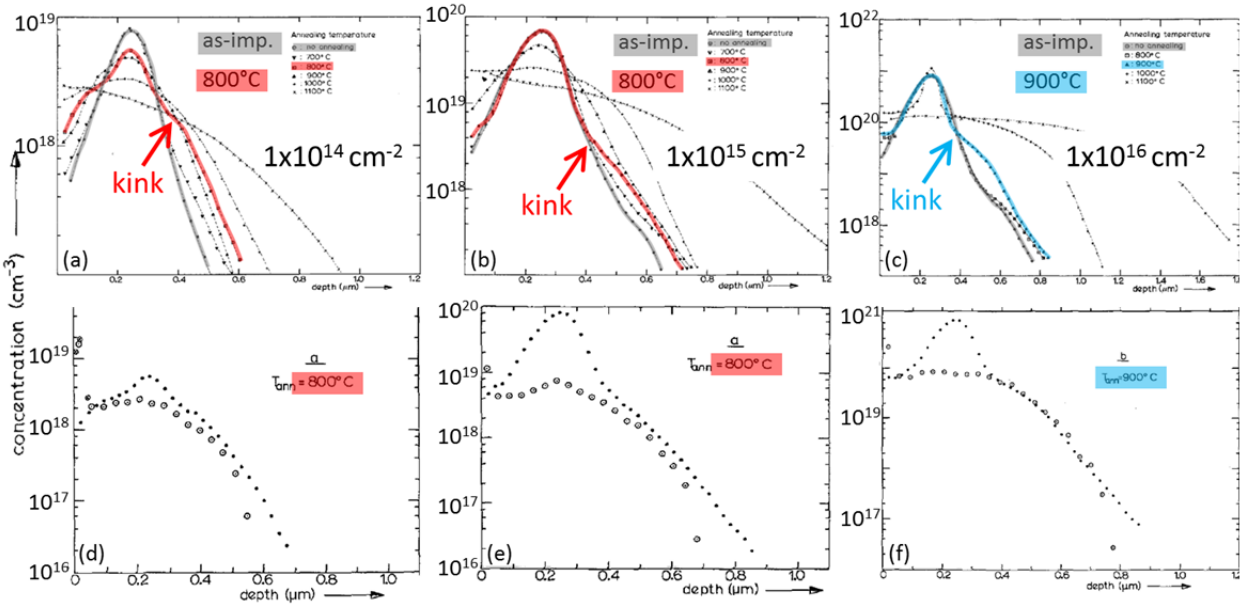

Figure 2 – SIMS profiles of 0.5 keV boron, after 650°C for 5 s annealing (SPEG) followed by post-annealing at 800°C: (a) 10–120 s; (b) 120–900 s.

Subsequent measurements of dopant electrical activation by differential Hall effect (see Figure 2 bottom row) finally demonstrated that the Boron atoms contained in the immobile peak are electrically inactive, i.e. none of them occupies a substitutional lattice position after annealing, so that the kink observed in SIMS profiles can be used to provide a good estimation of the "maximum electrical concentration", C_{el}.

It was initially proposed [1] that the immobile boron fraction consists of precipitated boron, although it occurred at relatively low concentrations (~3×10^{18} cm^{-3} at 800°C) compared to the higher known solid solubility values [3]. Later investigations [4,5] confirmed that, at low annealing temperatures, C_{el} values are lower than solid solubility ones (measured at thermodynamical equilibrium), as shown in Figure 3 (from ref. [6]). While at high temperature (> 900°C) most reported data are in agreement with the solid solubility values determined by Armigliato et al. [7] (solid line), the low temperature ones are instead well fitted by the intrinsic carrier concentration, n_i (dotted line in Figure 3), suggesting that the Boron "trapping reaction" responsible for its deactivation might be accelerated by a change in the Fermi level [5]. In any case, it was always found that after sufficiently long annealing times, the static peak gradually dissolves until the "maximum electrical activation" values converge towards the solid solubility limit.

Concerning the chemical composition of the defects responsible for Boron deactivation, it was initially proposed [1] that the electrically inactive part of the Boron profiles consisted of precipitates containing only Boron atoms, as no evidence for Boron compound formation (BN or Si_xB_y) was found. Later works of Michel *et al.* [4] and Cowern *et al.* [5] mentioned above contributed to establish that the static peak is instead due to the trapping of Boron atoms within some form of implantation-related defects, such as the "Intermediate Defect Configurations" (IDCs) proposed by Tan [8]. In particular, Cowern *et al.* developed a model in which IDCs were treated as small clusters containing both Boron and Si self-interstitial atoms.

The confirmation that Si_{int}s originating from the implant damage caused the

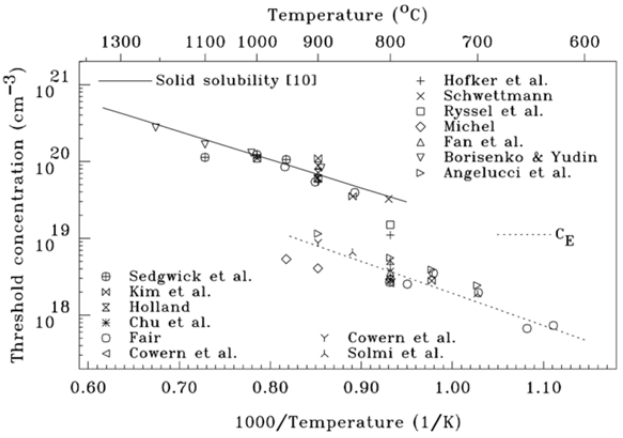

Figure 3 – Threshold concentration below which Boron is mobile during post-implantation annealing. (From ref. [6])

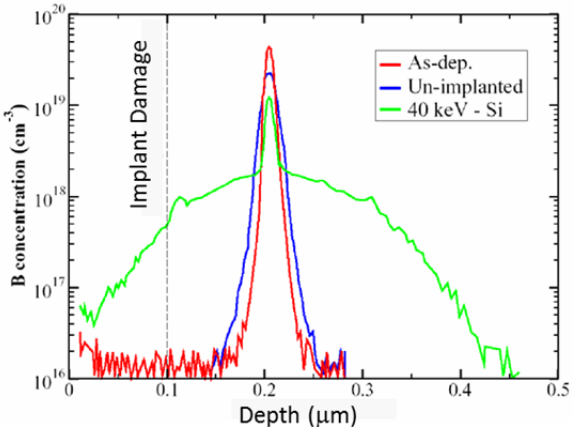

Figure 4 – SIMS measurements of a Boron doping spike in MBE-grown Si layers in the "as-grown" state (red) and after diffusion at 810°C for 15 min without (blue) or with (green) a Si^+ implant at 40 keV prior to the anneal (From ref. 9).

clustering of immobile and electrically inactive Boron came from a different class of experiments which allowed to spatially separate the source of $Si_{int}s$, generated by a near-surface Si^+ implant, from the Boron atoms, introduced in substitutional position (by CVD or MBE growth) in the form of deep marker layers (commonly known as *spikes* or *δ-layers*). Indeed, as shown in Figure 4 (from ref. [9]), experiments indicated that significant Boron immobile fractions were observed also in regions remote from the original implantation damage. In addition, it was found that the immobilisation reduced with distance from the implant damage.

Finally, the works of Pelaz *et al.* [10,11] established a comprehensive physical model in which individual reactions between Boron-Silicon clusters (today known as BICs [12]), diffusing Boron interstitials and $Si_{int}s$ were explicitly taken into consideration.

2.1.2. Open questions

Although the origin of inactive boron in ion-implanted USJs (as well as the conceptual difference between BICs formation and Boron precipitation) can be considered as fully understood on the basis of the works reported in the previous section, several open questions remained at the end of the 1990s about the formation and evolution of BICs and especially about their interaction with "pure-Si" extended defects, discussed in previous chapter, which "compete" with BICs during annealing. Some of these issues, listed below, have therefore been the subject of our researches that we will report in this chapter.

On the one hand, still today, most of the state-of-the-art USJs fabrication processes involve the formation of an amorphous surface layer before or during the dopant implant step, with the inherent advantage of reducing ion channeling during implantation and improving dopant activation [13]. In the case of Boron p^+-n junctions, these methods range from Ge^+[14] or low-temperature C^+ [15] pre-amorphisation, through F^+ co-implantation [16], molecular BF_2^+ and cluster implants [17], to BF_3 plasma implantation technology [18]. Amorphising implants create a large amount of damage in the Silicon lattice just beyond the amorphous/crystalline (a/c) interface, which upon annealing precipitates into the so-called end-of-range (EOR) defects, largely discussed in previous chapter. Two phenomena, both responsible for Boron deactivation, occur in the presence of EOR defects, namely *(i)* when point defects diffuse from EOR defects towards regions containing Boron, giving rise to the "reverse annealing" effect [19] or *(ii)* when Boron diffuses towards the EOR defects and decorate them, giving rise to the "Boron trapping" effect [20]. Our investigations of the "reverse annealing" effect, including one of the proposed solutions to reduce it through Fluorine co-implantation, will be presented in sections 2.2 and 2.3, while the "Boron trapping" effect will be discussed in section 2.4.

On the other hand, the question of the impact of BICs on the figures of merit of USJs has also been the subject of debates. Do they simply result in a reduction of the

Boron active dose or may they also impact the carrier mobility by acting as additional scattering centers? These aspects will be discussed in section 2.5.

Finally, most of the experimental studies that led to the development of physical models for the formation and evolution of BICs (presented in previous section) were carried on B marker layers with peak concentrations in the range 10^{19}-10^{20} B/cm^3, i.e. much lower than the concentration values typically attained during *source/drain* (S/D) fabrication. Indeed, in such experiments, no defects were observed that could be related to BICs. The question therefore arose whether or not BICs formed after high-dose boron-supersaturated S/D implants can evolve up to much larger sizes and eventually towards stable precipitates, such as the SiB_3 and SiB_4 borides predicted by the Si-B phase diagram [21]. In other words, can BICs be bigger than generally assumed? This will be the subject of the last section (2.6) of this chapter.

2.2. Boron deactivation : EOR-Induced BICs formation

One of the most used methods for the realisation of ultra-shallow p^+-n junctions consists in the pre-amorphisation of the substrate prior to dopant implantation followed by a low temperature Solid Phase Epitaxial Growth process (SPEG). SPEG has the advantage of allowing a high electrical activation [13] (above equilibrium solid solubility), with minimum dopant diffusion. Unfortunately, the activation achieved during SPEG appears to be metastable, so that upon subsequent thermal treatments (post-anneals) that follow the junction formation in a typical CMOS process flow, Boron deactivation is observed [19,22]. In this section, we present the main results of some of our research studies [14,23,24] that contributed to the understanding of the mechanism responsible for the electrical deactivation and reactivation of boron in pre-amorphised structures, together with a simple model that allows to simulate the evolution of the active dose during a post-anneal [25], which takes into account the evolution of both the End Of Range (EOR) defects induced by the pre-amorphisation step, and of the Boron-Interstitial Clusters (BICs) formed in the high-concentration Boron doped region. These works were carried out within the PhD thesis of Younes Lamrani and in collaboration with Mattson Thermal Products, Germany.

2.2.1. Experimental studies

In this study, USJs were obtained by implantation of 0.5 keV B ions to a dose of $1x10^{15}cm^{-2}$ into a Si substrate previously amorphised to a depth of ~50 nm by a Ge^+ implant (30 keV, $1x10^{15}$ cm^{-2}). After achieving recrystallisation of the whole wafer (SPEG) at 650°C for 5 s, several samples were then cut and re-annealed at different temperatures ranging from 250°C up to 1050°C. Figure 5 shows the B SIMS profiles obtained from the as-implanted sample (grey curve labelled "A") and the sample recrystallised at 650°C for 5 s (red curve labelled "B"). The typical kink that separates the immobile peak from the diffusing tail occurs at a concentration of ~$2x10^{20}cm^{-3}$,

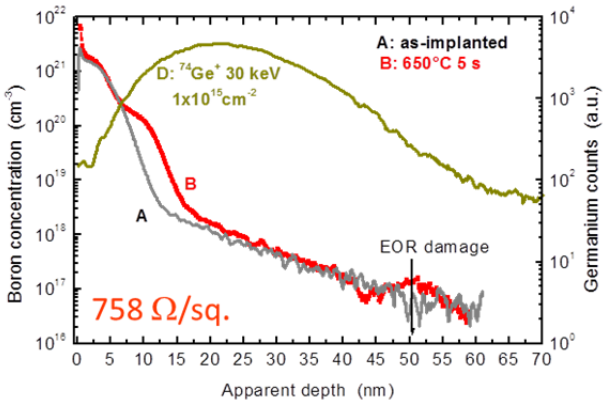

Figure 5 – SIMS profiles of as-implanted (labelled "A") and SPEG processed (650°C 5 s, labelled "B") boron distribution (0.5 keV, 1x10^{15} cm^{-2}). Also shown is the Ge^+ 30 keV 1x10^{15} cm^{-2} as-implanted profile.

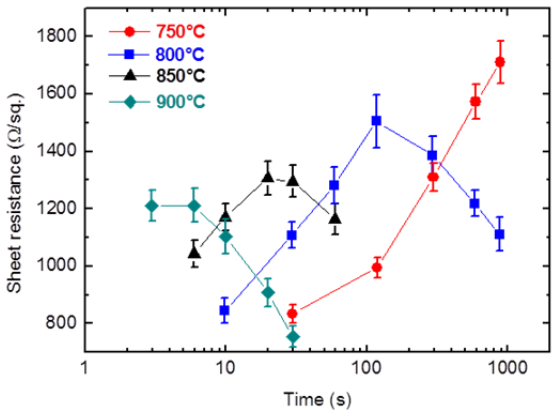

Figure 6 – Sheet resistance versus annealing time for SPEG activated junctions (650°C 5 s) after post-annealings at different temperatures ranging from 750°C to 900°C.

well above the solid solubility of Boron at this temperature (~1.5x10^{19} cm^{-3}), while the junction depth at 5x10^{18} cm^{-3} is as low as 15 nm, confirming the advantages of the low

SPEG process. The sheet resistance values of the SPEG activated junctions, measured after post-annealing at temperatures ranging from 750°C to 900°C, are reported in Figure 6 as a function of the annealing time. Results obtained at 800°C and 850°C indicate that a whole deactivation/re-activation process occurs at these temperatures with the sheet resistance increasing up to a maximum value before starting to decrease. The process kinetics speeds up when increasing the temperature, so that at 900°C deactivation occurs since the shortest investigated annealing times, while at 700°C sheet resistance is always found to increase within the investigated time range.

Additional SIMS, TEM and Hall-effect measurements were carried out on these samples to further investigate this phenomenon. For example, it was found that during deactivation at 800°C, the kink that separates the immobile peak from the diffusing tail progressively shifts towards lower concentration values (cf. Figure 7a) until stabilising at about 3x10^{19} cm^{-3} (cf. Figure 7b), corresponding to the Boron solid solubility at this temperature. As a consequence, the Boron active dose is expected to decrease during the early stages of the anneal, as confirmed by the Hall-effect

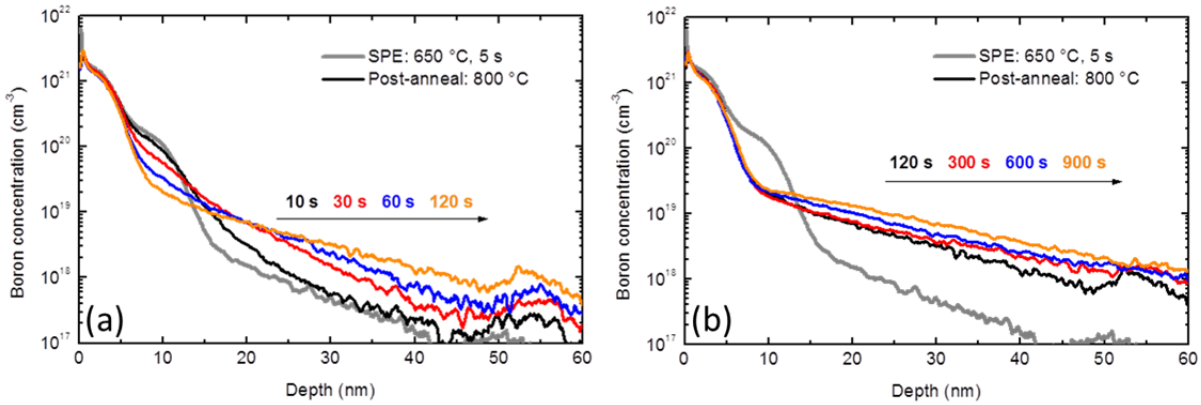

Figure 7 – SIMS profiles of 0.5 keV boron, after 650°C for 5 s annealing (SPEG) followed by post-annealing at 800°C: (a) 10–120 s; (b) 120–900 s.

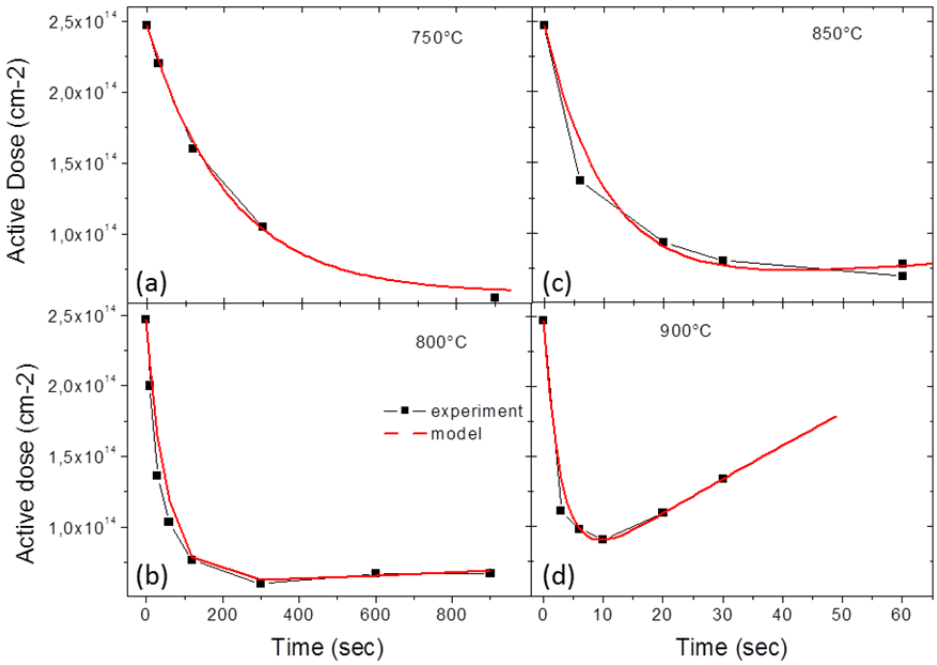

Figure 8 – Total active dose versus annealing time for SPEG activated junctions (650°C 5 s) after isothermal post-anneal steps at different temperatures. Symbols: experimental data. Lines: simulations. (a): 750°C. (b): 800°C. (c): 850°C. (d): 900°C.

measurements (cf. black squares in Figure 8b). Finally, TEM analysis from the same samples (not shown) indicated that the EOR defects undergo the usual non-

conservative Ostwald ripening process during annealing, during which the total number of atoms stored in the defects decreases while {311} defects progressively transform into dislocation loops. The similar time scales of these two phenomena (shift of the "kink" towards low concentration values and progressive dissolution of the EOR defects) therefore allowed to conclude that the deactivation process is due to the formation of BICs induced by the flow of free interstitials diffusing out of the EOR defect region during annealing, as schematically shown in Figure 9. This scenario was further confirmed by the physical model that will be presented in the next section.

On the other hand, the reactivation phase observed after longer annealing times (decrease of sheet resistance during annealing), was found to result from the combination of two phenomena: *(i)* the dissolution of BICs during annealing, leading to an increase of the Boron active dose (especially visible at higher annealing temperatures, cf. Figure 8d) and *(ii)* the progressive diffusion of the Boron profile tail (cf. Figure 7b), leading to an increase of the junction depth and of the average carrier mobility, both inducing a decrease of the sheet resistance (cf. eq. 1).

2.2.2. Modeling

The last part of this section presents a simple model that quantitatively accounts for the role of the defect evolution (EORs and BICs) in the deactivation/reactivation process. A full description of the mode developed with the help of Pierre Temple-

Boyer from LAAS, l is given at the end of this manuscript (cf. Appendix). Here, we report the equation that describes the evolution of the active dose, N_A, during the post-annealing step that follows the SPEG process:

$$N_A(t) = \Phi - \left\{ N_{BIC}(0) + \alpha \cdot N_{EOR}(0) \left[1 - \exp\left(-\frac{t}{\tau_{EOR}}\right) \right] \right\} \exp\left(-\frac{t}{\tau_{BIC}} \right) \qquad (2)$$

where Φ is the total implanted dose measured by SIMS, $N_{BIC}(0)$ is the initial concentration of BICs (i.e. after the SPEG process), $N_{EOR}(0)$ is the number of atoms in the EOR defects at the beginning of the post-anneal, α is interstitials deactivation efficiency, that is the number of deactivated B atoms per each incoming Si interstitial, τ_{EOR} and τ_{BIC} are the dissolution times of the EORs and BICs, respectively. During annealing, Si interstitial atoms emitted by the dissolving EOR defects, with a decay time τ_{EOR}, make the number of inactive B atoms contained in the BICs increase by $\left\{ \alpha \cdot N_{EOR}(0) \left[1 - \exp\left(-\frac{t}{\tau_{EOR}}\right) \right] \right\}$. In turn, similarly to the EOR defects, the total population of BICs also dissolves with its own decay time τ_{BIC} and a pre-exponential term that includes the continuous clustering due to the dissolution of the EOR defects.

Figure 8 reports the comparison between the calculated (red lines) and the measured (black symbols) values of the active dose. Among the various parameters needed for the calculation, Φ and $N_{BIC}(0)$ where extracted from SIMS, while $N_{EOR}(0)$ was directly measured by TEM. The interstitial deactivation efficiency, α, was extracted from the experimental data at 900°C using an approximation for eq. (2) at short annealing times ($t \ll \tau_{EOR}$, cf. Appendix) and then fixed for all other annealing temperatures. Finally, τ_{EOR} and τ_{BIC} were the only free parameters in the fitting procedure. We notice from Figure 8 that for all post-annealing temperatures the model allows an excellent fit to all of the experimental data. A value close to 2 was found for α (1.8), similar to what previously reported by Pawlak et al. [14]. This result indicates that one silicon interstitial atom escaping from the EOR defect band deactivates on average two

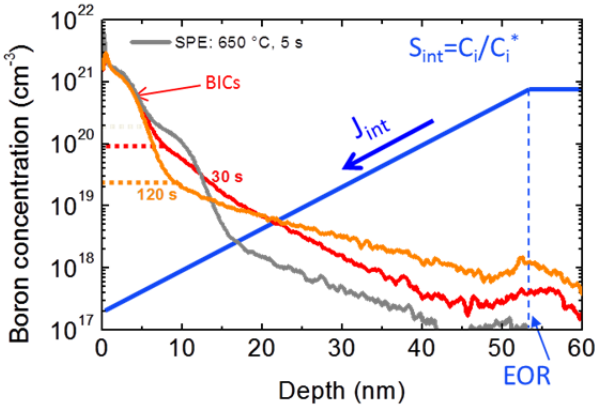

Figure 9 – Schematic representation of the Si_{int} supersaturation gradient (blue line) existing between the EOR defects and the surface. The consequent flux of interstitials, J_{int} is responsible for the deactivation of Boron (cf decrease of the kink position at increasing annealing times).

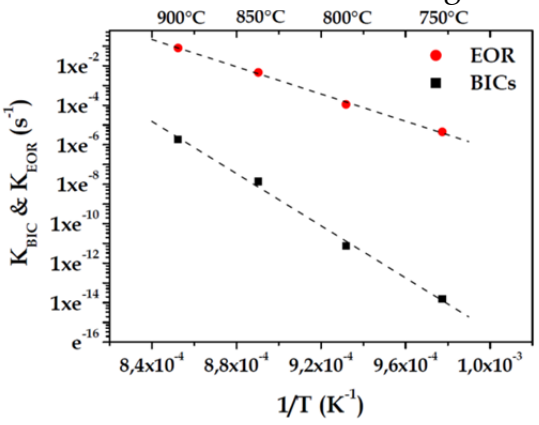

Figure 10 – Arrhenius plots of the EOR dissolution decay time ($1/\tau_{EOR}$) and the BIC dissolution decay time ($1/\tau_{EOR}$) extracted from simulations calculated in this work.

boron atoms by forming mainly B_2I clusters.

An Arrhenius plot of the extracted values of τ_{EOR} and τ_{BIC} (Figure 10) confirms that these two parameters are thermally activated, with activation energies of (3.0±0.1) eV and (5.7±0.3) eV, respectively. Although these values are based on a simple zero-dimensional model and their absolute values are to be considered as indicative, they suggest some considerations. First of all, the activation energy of τ_{EOR} is compatible with that found for the dissolution of {113} defects [26], which are the dominant defect type during the deactivation process (short annealing times). Secondly, the much larger value found for the activation energy of τ_{BIC}, E_{act} *(BIC)*, confirms that BICs are more stable than EORs, and need more time to dissolve, in agreement with the observation that dopant reactivation is effective only at very long annealing times. Finally, the very high value of E_{act} *(BIC)* (5.7 eV) is difficult to associate to a specific phenomenon, as the electrical dopant reactivation that we have measured is this experiment is the results of several mechanisms: BIC dissolution, migration of the generated mobile species (*BI*) and reaction with a vacancy to generate a substitutional dopant atom. In particular, it is known that several sizes may exist for the BICs (B_nI_m with several values for n and m [10]), so that the generation of mobile *BI* pairs can require different amounts of energy depending of the size of the dissolving cluster.

2.3. Reduction of BICs formation by Fluorine Co-implantation

The use of impurity co-implantation for the improvement of USJs figures of merit (junction depth and sheet resistance) has been the subject of several studies. In particular, Carbon [27,28,29,30,31] and Fluorine [32,33] were investigated for their impact on Boron diffusion and activation. In the case of Fluorine, a long controversy concerned its effect on B diffusion during SPE regrowth [34,35,36], and on B diffusion and deactivation during post-regrowth annealing [34,37,38,39]. In this section, we will first present an experimental study that contributed to resolve this controversy (section 2.3.1). In this study, we initially demonstrated the benefits of a F co-implant for the control of both B Transient Enhanced Diffusion (TED) and deactivation during annealing in a pre-amorphised USJ [16]. We then investigated the impact of a Fluorine co-implant on the evolution of the end-of-range (EOR) defects created by a standard Ge^+ pre-amorphisation step [25,40]. The results showed that the modification of the EOR population by a F co-implant has little effect on the reduction of B deactivation during annealing, therefore supporting the formation of independent F-related Si_{int} traps as the main mechanism responsible for the stabilisation of B activation. These F-related defects are located between the EOR defects and the B doped layer and trap Si_{int} atoms as they flow from the EOR band towards the surface. The nature of the F-related traps was investigated in subsequent studies that will be summarised in section 2.3.2. They revealed the presence of F-V clusters (in the form of open volume defects [41] or large cavities [42,43]), as well as

F-I clusters (in the form of SiF_4 molecules [44]) in F^+-implanted silicon. These results were obtained within the post-doctoral activity of Simona Boninelli.

2.3.1. Experimental evidence

The experimental setup is described in Figure 11a. A Si wafer was initially amorphised to a depth of ~50 nm by a 30 keV Ge^+ implant ($1x10^{15}$ cm^{-2}), then implanted with 0.5 keV B^+ to a dose of 1×10^{15} cm^{-2}. Subsequently, F^+ ions at 10 and 22 keV with doses in the range 1×10^{14}–1×10^{15} cm^{-2} were implanted. The F energies were set at different values in order to place the F respectively between the projected range of boron implant and the amorphous-crystalline interface, where the EOR defects are formed (10 keV) or at this interface (22 keV). Finally, all samples were annealed at 800°C for different times ranging from 1 to 2700 sec.

The B SIMS profiles measured after annealing at 800°C for 2700 sec are reported In Figure 11b. The annealed profile of the reference sample (without F) exhibits the usual features of such experimental conditions, i.e. a static peak, 'kink' and fast-diffusing tail. The kink concentration ($3x10^{19}$ cm^{-3}) corresponds to the equilibrium Boron solid solubility at 800°C. This indicates that although the PAI step allows to activate the dopants above the solid solubility limit, the extremely long annealing anneal time has induced a return to thermodynamical equilibrium. On the other hand, the exponential shape of the diffusing tail is typical of the TED mechanism, which is controlled by the Si_{int} atoms diffusing from the EOR region towards the B implanted layer. In contrast, when Fluorine is co-implanted either at 10 keV or 22 keV, the kink concentration is 'blocked' at the high value (~$1x10^{20}$ cm^{-3}) typically allowed by pre-amorphisation, while the tail diffusion is strongly reduced.

In Figure 12a, the sheet resistance values R_s are reported, respectively, for the "no F" and for the F co-implanted samples with a fluence of $1x10^{15}$ cm^{-2}. It is evident that after the 10 keV and 22 keV co-implants the sheet resistance stays constant

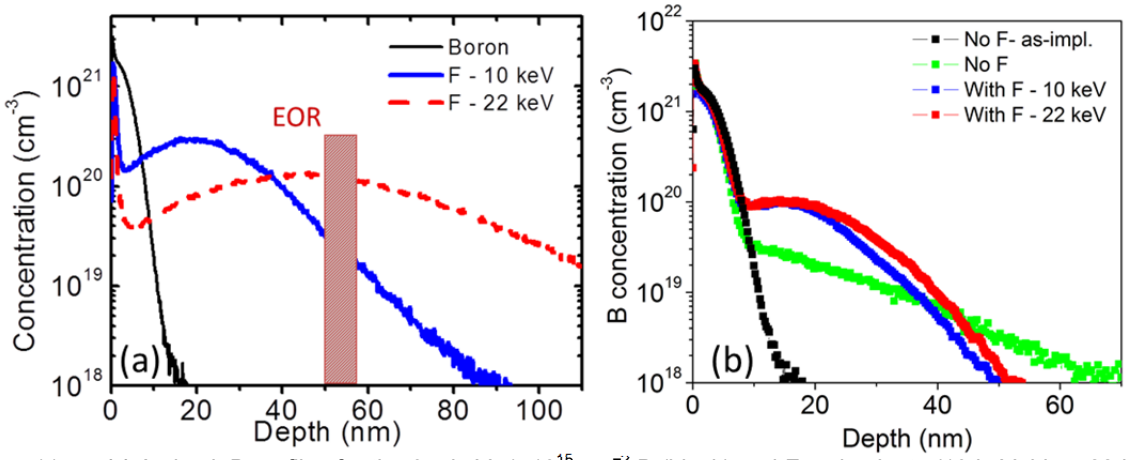

Figure 11 – *(a)* As-impl. B profiles for the 0.5 keV, $1x10^{15}$ cm^{-2} B (black) and F co-implants (10 keV, blue; 22 keV, red). Also shown is the expected depth of the EOR defects from the 30 keV Ge PAI implant (hatched area). *(b)* B annealed profiles (800°C, 2700 s) in reference (green) and F^+ co-implanted samples (10 keV, blue; 22 keV, red).

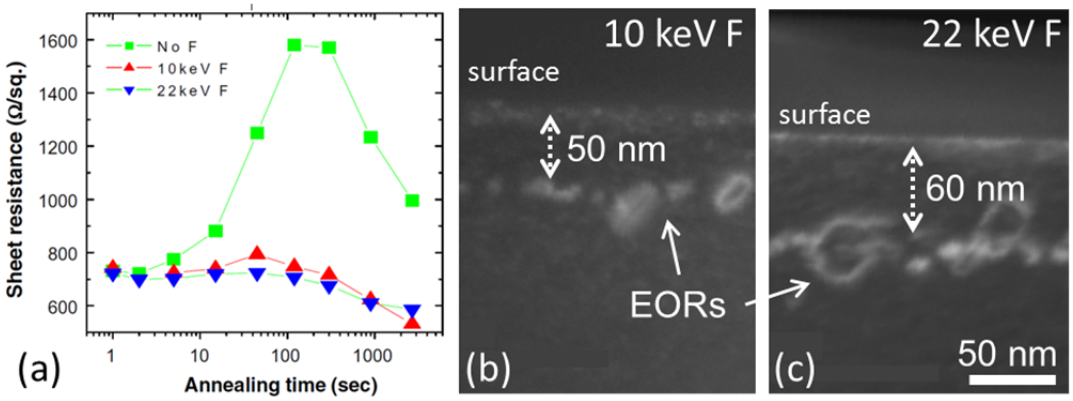

Figure 12 – *(a)* Sheet resistance values for a 0.5 keV B implant in Ge^+ preamorphised silicon after annealing at 800°C, without F co-implant, (green curve) or with 10 keV (red) and 22 keV (blue) F^+ co-implants to a dose of $1\times10^{15}cm^{-2}$. *(b)-(c)* WBDF cross-section micrographs from the samples co-implanted with 10 keV (b) or 22 keV (c) F and annealed for 300 sec at 800°C.

throughout the anneal, therefore providing excellent protection against deactivation[#]. Indeed, in the "no F" sample, R_s rises to a peak value of 1580 Ω/sq. and then falls at longer annealing times. This behaviour is expected from earlier work (cf. section 2.2) and can be understood in terms of Si_{int} trapping to form B-I clusters, followed by reactivation of the clusters and diffusion of B. The SIMS and electrical measurements therefore indicate that, in the presence of Fluorine, some mechanism is preventing the interstitial-driven processes of deactivation and enhanced diffusion.

Among the possible explanations for the beneficial effect of Fluorine in the stabilisation of B activation in USJs, it was proposed that F forms F-vacancy (F-V) clusters during SPE, thus providing traps for Si_{int}s that would otherwise flow toward the surface from the EOR band [37]. Alternatively, it was proposed that that F directly interacts with Boron, thus reducing B diffusion [45]. It was also suggested that F might increase the stability of the EORs, thereby reducing the supersaturation of free Si_{int} atoms in the EOR region and, thus, their flux toward the B profile [39]. Finally, the evolution of the EOR in the presence of F was studied by Downey et al. [34], where it was concluded that the presence of F does not affect their evolution. Since the 10 keV and 22 keV F^+ implants used in our experiment have different overlap with the EOR defect band, we therefore studied their evolution as a function of the F^+ implant conditions in order to resolve this controversy.

The cross section TEM micrographs shown in Figure 12 (b and c) show that after 10 keV F^+ implant, the EOR defects are located at the same depth, ~50 nm, as the "no-F" reference sample (not shown). In contrast, after 22 keV F^+ implant, the EOR defects are located deeper (~60 nm), indicating that the damage induced by the higher energy F implant extends more deeply than the one produced by the initial Ge^+ implantation, with the consequence of pushing down the c-a interface. This suggests

[#] The effect of Fluorine was found to be still effective even after high temperature anneals [S. Paul, W. Lerch, B. Colombeau, N.E.B. Cowern, F. Cristiano, S. Boninelli and D. Bolze, J. Vac. Sci. and Tech. B, 24 (2006) 437]

in turn that after the 22 keV F^+ implant, the number of Si_{int}s involved in the EOR defect formation process might be much higher than in the reference "no-F" case. This last point was verified by plan view TEM analysis (cf. Figure 13 for an anneal time of 15 s). The "no F" and the 10 keV F co-implanted samples exhibit similar defect populations, with a slight increase of the defect density in the 10 keV sample, while the defect population essentially consists of {311} defects in both cases. In contrast, for the 22 keV F sample, the defect population has drastically changed. Not only the apparent defect size is larger than in the other cases (while the density stays to similar values) but it contains a much higher DLs fraction (~80%). Moreover, the quantitative analysis of the defect populations, supported by simulations of defect evolution showed that, with respect to the "no F" and the 10 keV F samples, the number of Si atoms stored in the EORs in the 22 keV F sample is 5 times higher than in the 10 keV F one after 15 sec. On the other hand, no dissolution occurs between 15 and 300 s, in contrast with the two other cases.

These results indicate that the high concentration of excess Si_{int}s introduced by the 22 keV F implant, while being responsible for the displacement of the a/c interface, also accelerates the kinetics of the transformation of {311}s into DLs. As discussed in section 1.4.1, this transformation is thermally activated and takes place through a reaction barrier, with the transformation rate being proportional to the density of {311} defects. We therefore suggested that the observed increase of the DLs fraction in the 22 keV F sample was due to the increased number of Si_{int}s induced by the F implant. However, subsequent simulations showed that this mechanism could only partially explain the observed results, indicating that an additional "chemical effect" should be considered to explain the enhanced DLs formation in the presence of F.

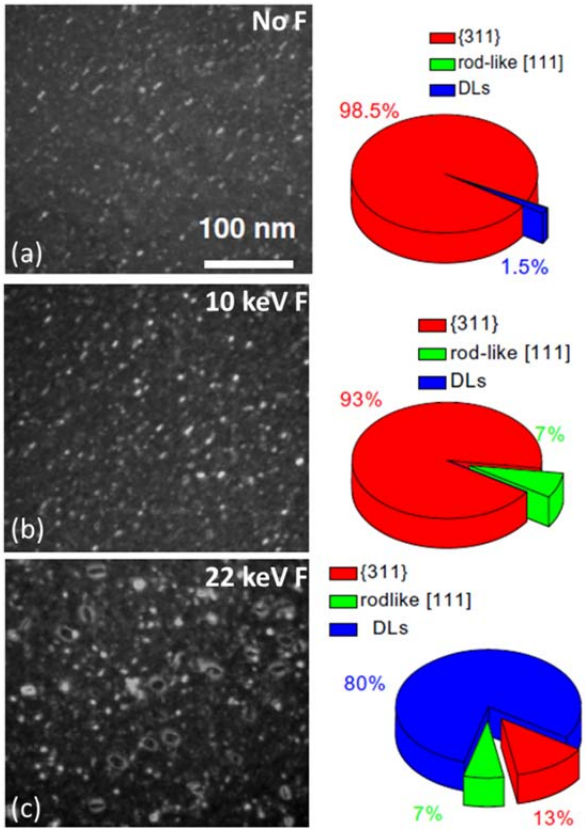

Figure 13 – *(left column)* WBDF plan-view micrographs of preamorphised Si samples (30 keV Ge^+, $1\times10^{15}cm^{-2}$) implanted with 0.5 keV B^+, $1\times10^{15}cm^{-2}$ with and without F^+ co-implantation (*a*: no F, *b*: 10 keV F, *c*: 22 keV F) after annealing for 15 sec at 800°C. *(right column)* Corresponding normalised densities of the observed defects according to their nature.

In summary, our results allowed to unambiguously conclude that the beneficial effect of F for the reduction of both B TED and deactivation cannot be explained in terms of a stabilisation of the EOR defects. Indeed, even when the F implant stabilises the EOR defects (22 keV F, with early

formation of DLs and quasi-conservative defect ripening), the reduction in B TED and deactivation is virtually identical to that obtained at lower F energy (10 keV), which has almost no impact on the EOR defect population. Instead, our results supported the idea that F-related Si_{int} traps form during SPE and act as trapping centres for Si interstitial atoms flowing from the EOR defects, so that to stabilize B doping profiles against deactivation and enhanced diffusion.

2.3.2. Nature and thermal evolution of F-related $Si_{int}s$ traps

The formation of large vacancy-related clusters has been largely reported in literature. Early evidence of "fluorine bubbles" in Si structures implanted with Fluorine was provided by TEM analysis [46,47], while "open volume" defects were later observed by Positron Annihilation Spectroscopy (PAS) [48,49]. Subsequent PAS studies [50] established that F retards recombination between vacancies and interstitials, favouring the formation of vacancy clusters (close to the projected range of the implanted F) and interstitial clusters at deeper positions. In addition, the dangling bonds of such vacancy clusters are a preferential site for the precipitation of Fluorine, explaining the F accumulation in the region containing the large open volume defects observed by PAS. These results were later supported by theoretical investigations [38] in which it was proposed that F precipitation occurs in the form of F_nV_m complexes, with F_3V, F_4V and F_6V_2 being the most stable configurations. However, recent investigations based on x-ray absorption spectroscopy [44], revealed that none of the proposed F_nV_m clusters could explain the experimental XANES and EXAFS spectra measured from Fluorine implanted samples. Instead, it was shown that the vast majority of the implanted Fluorine precipitates in the form of SiF_4 molecules, whose atomic structure (including the Si-F bond length) allows to perfectly reproduce the experimental results.

Apart from the difference in the proposed form of the F precipitates that fill the vacancy clusters (F_nV_m complexes or SiF_4 molecules), it is agreed in all these studies that, in the case of amorphising implants, the F-precipitate filled cavities should form

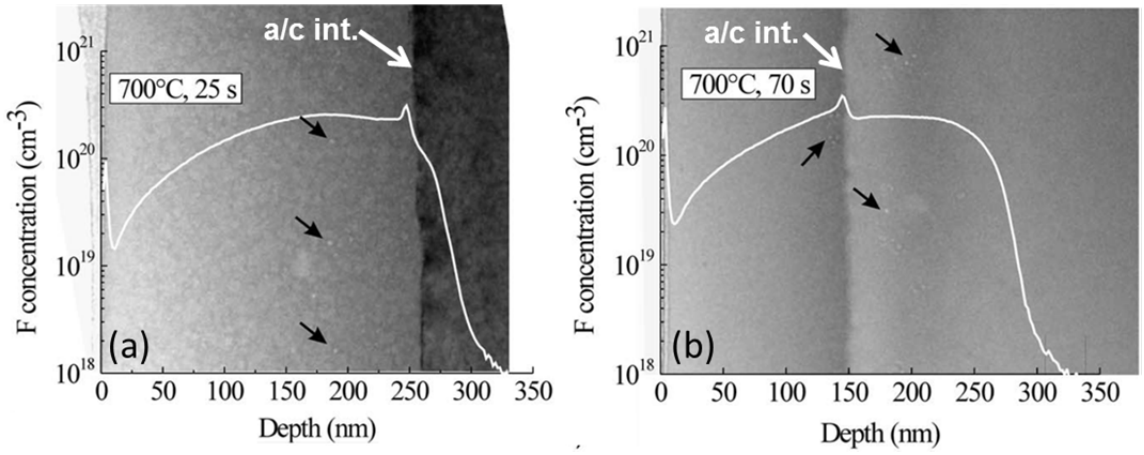

Figure 14 – SIMS *F* concentration profiles (white curves) overlapped with TEM cross-sectional view of samples implanted with F and partially regrown by SPE at 700 °C for 25 s *(a)* and 70 s *(b)*.The black arrows point to some F-related bubbles.

in the amorphous phase and be "transferred" without modification into the crystalline phase during SPEG, where there can finally act as traps for free Si_{int} atoms diffusing out of the EOR defect region, therefore reducing Boron TED and deactivation during subsequent annealing.

This scenario, initially predicted on the basis of theoretical studies [38] was later confirmed by the experimental investigations of Boninelli *et al.* [42,43], as shown in Figure 14, where Fluorine-related cavities (black arrows) are observed both in amorphous regions at the early stages of recristallisation (Figure 14 a) as well as in recristallised areas (Figure 14 b, below the a/c interface) after longer annealing times. In the same studies, it was also demonstrated that upon further annealing at higher temperature, Fluorine is lost from the cavities, inducing a reduction of the total volume they occupy (in agreement with PAS investigations, [41]), which accompanied by a change in their shape (from spherical to cylindrical). Finally, the beneficial effect of Fluorine in trapping free Si_{int} atoms was demonstrated by the inhibition in the formation of implantation-induced {311} defects in Si samples containing Fluorine.

2.4. Boron trapping in pre-amorphised USJs

In addition to the dopant deactivation phenomenon discussed in the two previous sections, another phenomenon typically occurs in preamorphised USJs that also leads to local dopant deactivation. Indeed, it has been often observed that is such structures the tail of the Boron concentration profiles shows an anomalous peak [14,51,55] in correspondence with the EOR defects after annealing, which is generally associated to the "trapping" of Boron by the defects. In addition, it is generally accepted that the boron atoms contained in the so-called "trapping peak" are immobile and electrically inactive. As shown in previous chapter, EOR defects are known to exist under various kinds: small ICs, {311} defects, {111} rod-like and DLs, and it is therefore important to understand which of these defects are more effective in trapping boron atoms in order to reliably simulate this phenomenon. In addition, the defect formation itself can be modified in the presence of impurities, as it was shown for instance for Boron [52] and Carbon [30,53,54] and this can also have an impact on the Boron trapping mechanism. In a previous model [55], it was assumed that the capture of boron atoms depends only on the density of small ICs. Due to the intrinsic nature of the Ostwald ripening mechanism of the defect evolution, this model systematically predicted a decrease of the boron trapping peak when increasing the thermal budget. However, some experimental data [56,57] show that the boron trapping peak can have a different behaviour, i.e. it can increase in the early stages of annealing.

In this section we will therefore summarise one of our research activities, carried out within the PhD thesis of Mehdi Bazizi [58,59] that I co-supervised with Ardechir Pakfar from STMicroelectronics, Crolles and the post-doctoral activity of

Pier Francesco Fazzini, that contributed to improving the understanding of this phenomenon. For this, we first used dedicated test structures to study the boron trapping at EOR defects, by a combination of SIMS and TEM measurements. Based on the experimental results, we then developed (and implemented in a commercial process simulator) a boron-trapping model that takes into account the nature of the extended defects on the Boron trapping efficiency.

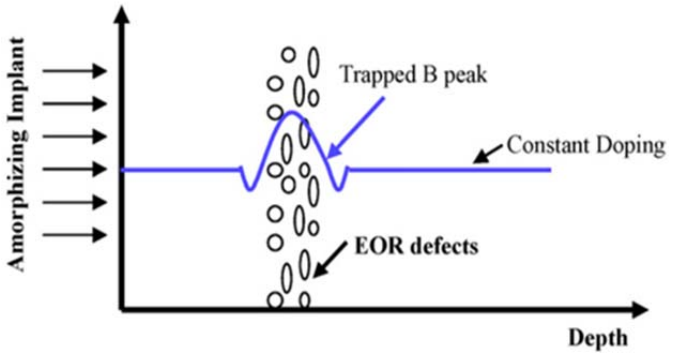

Figure 15 – Schematic illustration of the structure used in this experiment for the investigation of boron trapping at EOR defects.

2.4.1. Experimental investigations

The experiment was based on three different wafers. All of them were amorphised to a depth of ~50 nm by a 30 keV Ge^+ implant ($1x10^{15}$ cm^{-2}). The first two wafers, schematically represented in Figure 15, had a nominal constant concentration of B (~$2x10^{18}$ cm^{-2} in wafer I, ~$1x10^{20}$ cm^{-2} in wafer II), while the third one was implanted with 0.5 keV B^+ to a dose of $1x10^{15}$ cm^{-2}. The as-implanted boron profile in wafer III is entirely contained in the amorphous layer, so that the EOR defect formation and evolution is not affected by the presence of Boron. Similarly, the doping concentration in wafer I (~$2x10^{18}$ cm^{-2}) was chosen to avoid any modification of the defect evolution, as previously suggested [52]. Several specimens were then annealed in Nitrogen at 700 °C, 800 °C, and 900 °C for times ranging from 3 to 1000 s and Boron concentration profiles measured by SIMS.

Figure 16a reports the results from wafer I, where the Boron concentration at the trapping peak (measured by SIMS) is reported as a function of annealing time for different temperatures (cf. dashed lines). At 700°C (blue triangles), the maximum boron concentration in the trapping peak is found to increase with increasing

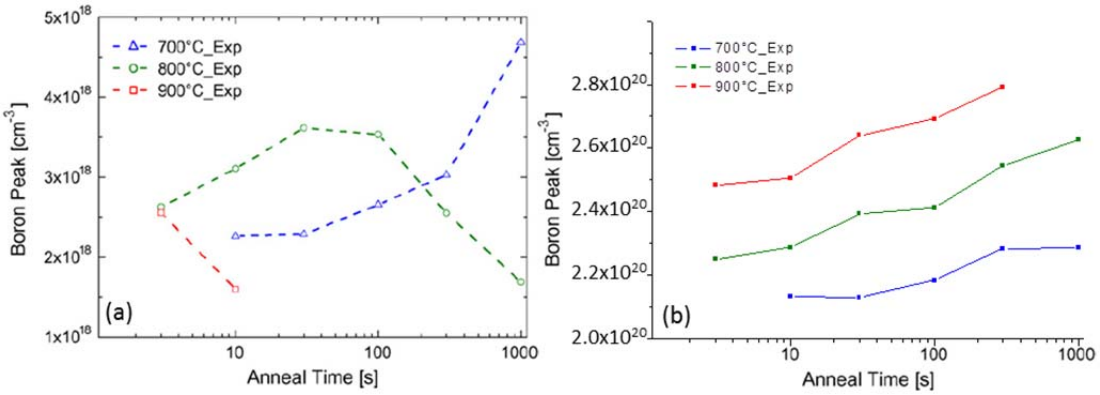

Figure 16 – Time evolution of the Boron concentration at the trapping peak (measured by SIMS) for various annealing temperatures in Ge^+ pre-amorphised wafers containing a uniform concentration of B doping. (a) Wafer I (~$2x10^{18}$ cm^{-2}). (b) Wafer II (~$1x10^{20}$ cm^{-2}).

annealing time. TEM analysis performed on the same samples (not shown) indicates that at this temperature only {311} defects are formed, which undergo the usual Ostwald ripening (i.e. increase in size, decrease in density). This clearly suggests that {311} defects actively contribute to the formation of the trapping peak. In contrast, at 900°C, the boron trapping peak quickly disappears after few seconds of annealing (red squares), although DLs were still observed after annealing times up to several hundreds of seconds. This result suggests that the DLs contribution to trapping is less pronounced than that of {311}s. In fact, the boron trapping peak, that is visible for small annealing times, could be associated to the initial presence of {311}s, which are not entirely replaced by loops after a few seconds anneal at 900°C. This hypothesis is compatible with the 800°C trend (green circles) in which the peak value starts to decrease at a later time during annealing. This can be understood considering that the transformation of {311}s into loops takes place at longer annealing times for 800°C anneals with respect to 900°C, therefore confirming that the trapping of boron is mainly driven by the evolution of {311} defects.

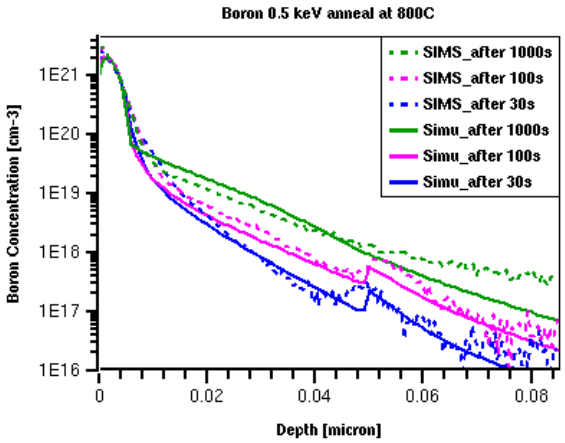

Figure 17 – Comparison between measured (dashed lines) and simulated (solid lines) Boron concentration profiles from wafer III (implanted with 0.5 keV B^+, 1×10^{15} cm^{-2}) after annealing at 800°C.

SIMS data relative to wafer III (implanted B profile) after annealing at 800°C are shown in Figure 17 (dashed lines). As mentioned above, defect evolution is not influenced by the presence of Boron, similarly to wafer I. In addition, it can be observed that the B trapping peak, formed at the EOR defects layer position, increases at short times and begins to decrease after 100 s annealing, which is the same trend as for Wafer I. The same agreement between wafers I and III was also found for 700°C and 900°C (not shown), which confirms the higher efficiency of {311} defects in trapping Boron, compared to DLs.

A completely different behaviour of the Boron concentration at the trapping peak was found in the highly-doped wafer II ($1x10^{20}$ B/cm^3), as shown in Figure 16b, where the amount of trapped boron is much higher than in the low-concentration wafer I (with a maximum increase of $7x10^{19}$ cm^{-3} for the peak concentration, compared to $3x10^{18}$ cm^{-3} in wafer I), while the peak magnitude constantly increases with annealing time for all temperatures. In addition, only a small concentration of defects was revealed by TEM analysis, in agreement with previous reports on the impact of B doping on {311} defect formation [52]. In such case, the concentration of Boron largely exceeds its equilibrium solid solubility limit at the investigated annealing temperatures. The observed defects might therefore correspond to large Boron precipitates that have grown from smaller BICs. The possibility (for BICs) of reaching

such stable configurations in heavily Boron-doped silicon has been the subject of several studies which will be discussed in section 2.6. In any case, the observed increase of the Boron trapping peak in wafer II is certainly associated with the continuous growth of Boron precipitates (in the form of either small BICs or larger defects).

2.4.2. Modelling

In order to model the boron trapping at EOR defects accurately and efficiently, the model was developed directly within the Sentaurus Process TCAD commercial simulator [60]. For the whole extended defect evolution, the "moment"-based model (cf. section 1.5.3) was used. In addition, some further simplifying assumptions were required. We therefore assumed that only neutral BI pairs (B–I+) can be captured and emitted from either {311} defects or DLs. It was also assumed that the trapped BI pairs are located along the defects' perimeter.

The aim of the model is to calculate the concentration of Boron atoms trapped at {311} defects (C_{B311}) and DLs (C_{BDL}). For this, we first define the "BI capture efficiency" of a defect, $\alpha_{Bdifect}^{\max}$, as the ratio between the number of available traps along the edges of the defect and the total number of interstitial atoms in the defect. This will give, for {311}s and DLs:

$$\alpha_{B311}^{\max} = \frac{2 \cdot \sqrt{\rho_{311}} \cdot (L_{311} + w_{311})}{w_{311} \cdot L_{311} \cdot \rho_{311}} \quad \text{and} \quad \alpha_{BDL}^{\max} = \frac{2\pi \cdot R_{DL} \cdot \sqrt{d_{111}}}{\pi R_{DL}^{\ 2} \cdot d_{111}} = \frac{2}{R_{DL} \cdot \sqrt{d_{111}}} \tag{3}$$

where w_{311} is the {311} width, L_{311} is the average {311} defects length (as calculated by the "moment"-based defect model), ρ_{311} is the interstitial density in a {311} defect, R_{DL} is the radius of dislocation loops and d_{111} is the density of atoms in a {111} silicon plane. More details on the values of these physical parameters are given in [59].

Assuming that all capture rates are diffusion limited and proportional to the concentration of free trap sites for BI at {311} defects and DLs edges, respectively, the capture rates can be expressed as

$$K_{311}^{cap} = 4\pi \cdot r_{B311}^{cap} \cdot D^{BI} \cdot C_{BI} \cdot C_{B311}^{*} \quad \text{and} \quad K_{DL}^{cap} = 4\pi \cdot r_{BDL}^{cap} \cdot D^{BI} \cdot C_{BI} \cdot C_{BDL}^{*} \tag{4}$$

where r_{B311}^{cap} and r_{BDL}^{cap} are the defect capture radii (expected to be close to the interatomic distance in the Si lattice), while D^{BI} and C_{BI} are the diffusivity and concentration of BI pairs. C_{B311}^{*} and C_{BDL}^{*} represent the concentration of free trap sites for BI on {311}s and DLs perimeters, respectively, and are given by:

$$C^{*}_{B311} = \alpha^{\max}_{B311} \cdot C_{311} - C_{B311} \quad \text{and} \quad C^{*}_{BDL} = \alpha^{\max}_{BDL} \cdot C_{DL} - C_{BDL} \tag{5}$$

where C_{311} and C_{DL} are the {311} and DLs concentration as calculated by the "moment"-based defect model. Finally, the emission rates of trapped BI from {311}s and DLs are assumed to be simply proportional to the number of trapped BI:

$$E^{BI}_{311} = e^{BI}_{311} \cdot C_{B311} \quad \text{and} \quad E^{BI}_{BDL} = e^{BI}_{BDL} \cdot C_{BDL} \tag{6}$$

e^{BI}_{311} and e^{BI}_{BDL} are the most important parameters for the calibration of the model. Since the emission process involves a reaction barrier, it should be possible, at least in principle, to express these coefficients as an Arrhenius function of the temperature.

In conclusion, the model has four calibration parameters: r^{cap}_{B311}, r^{cap}_{BDL}, e^{BI}_{311} and e^{BI}_{BDL}, whose values must be determined by comparison with the experimental data.

The model was initially calibrated against the experimental results obtained in the low-concentration Boron-doped wafer (wafer I) in which the defect evolution was not affected by the presence of Boron. The simulation results are summarized in Figure 18a, which presents the evolution over time of the boron-trapping peak at 700, 800 and 900°C. The various trends of the peak concentration at different temperatures are perfectly reproduced, including the continuous peak concentration increase at 700°C and its decrease at 900°C (as well as after 100 s at 800°C, when most of the {311} defects have been transformed into DLs. A similar excellent agreement was obtained in the case of wafer III (implanted B profile) as shown in Figure 17 (solid lines). Also in this case, the defect evolution was not affected by the presence of Boron. In has to be noted that, in addition to the trapping peak at the EOR defect region, the implanted Boron profiles also exhibit an immobile peak closer to the surface, which is correctly simulated by the BICs formation model available in the Sentaurus Process TCAD

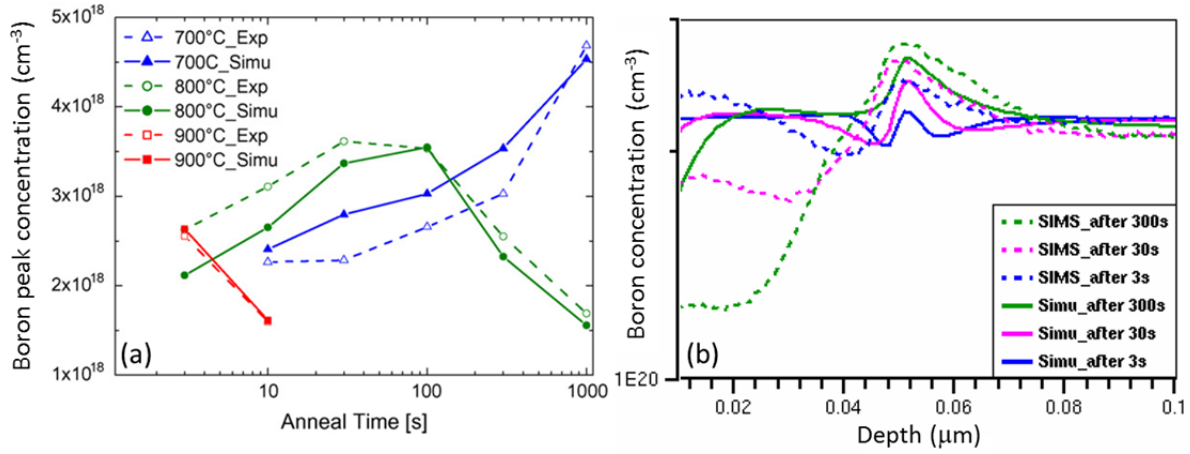

Figure 18 – Comparison between experimental data (dashed lines) and simulation results (solid lines) of Boron trapping for various annealing conditions in Ge^{+} pre-amorphised wafers containing a uniform concentration of B doping. (a) Wafer I (~$2x10^{18}$ cm^{-2}): time evolution of the Boron concentration at the trapping peak. (b) Wafer II (~$1x10^{20}$ cm^{-2}): Boron concentration profiles in the EOR defect region measured after different annealing times at 800°C.

simulator. These results confirm that when Boron trapping in the EOR region occurs in the presence of the known implantation-induced extended defects ({311}s and DLs), the observed phenomenon can be correctly modeled taking into account only the capture and release of boron atoms by the {311} defects formed in the EOR region. This model has been implemented in the commercial SProcess TCAD simulator [10] since 2009.

Finally, in the case of the highly-doped wafer II ($1x10^{20}$ B/cm^3), the Boron peak evolution, is well reproduced only qualitatively, as shown in Fig. Figure 18b for an annealing temperature of 800°C (i.e. the trapping peak continuously increases with annealing time, unlike the lower B concentration case). As discussed in previous section, the observed increase of the Boron trapping peak in this wafer is due to the continuous growth of Boron precipitates (in the form of either small BICs or larger defects). Indeed, it is interesting to note that although both the Boron-trapping and BICs formation models are activated, the simulated Boron peaks are due only to BICs formation, in agreement with experimental data (extended defect formation was inhibited). This indicates that the existing BICs model requires either a better calibration or a more "profound" modification to allow the formation of much larger Boron precipitates, as it will be discussed in section 2.6

2.5. Impact of BICs on carrier mobility

The assessment of the electrical dopant activation (total active dose or maximum active concentration) of a junction is often based on the combination of the chemical dopant concentration profile (measured by secondary-ion-mass spectroscopy (SIMS)) and junction sheet resistance (obtained by four point probes measurements) [61,62,63] in which it is systematically assumed that the mobility vs. concentration relations [64,65] are valid. However, as mentioned in section 2.1.2, state-of-the-art ultra-shallow junctions usually contain large amounts of BICs that may act as additional scattering centers and have an impact on the carrier mobility. Indeed, as shown in Figure 19, several works [25,66,67,68] reported hole mobility values systematically lower than expected, when considering the corresponding carrier concentration. Clarysse *et al.* [69] compared several characterisation techniques to investigate Boron activation in USJs. They confirmed that some deviations between theoretical and measured mobilities existed in various samples containing BICs and suggested that inactive boron could be responsible for this difference.

All the cited works used Hall-effect measurements for the determination of the carrier mobility. It is therefore important to know whether the measurement itself is affected by the presence of high concentrations of inactive Boron clusters. For example, Clarysse *et al.* [69] assumed that, while affecting mobility, the presence of inactive Boron would not have any impact on the Hall scattering factor, r_H. We investigated this issue in detail within the PhD research project of F. Severac [70] that I co-supervised with Elena Bedel from LAAS. The main results of this activity will be

summarised in the following sections. We will first present in section 2.5.1 an empirical method for the self-consistent interpretation of SIMS and Hall effect measurements of boron-doped ultra-shallow junctions that allows (i) to estimate the activation level of the doped layers (maximum active dopant concentration, active dose fraction) and, for the case of partially activated structures, (ii) to assess whether or not the carrier mobility is affected by the electrically inactive BICs. The main experimental results obtained in this study will be presented in section 2.5.2.

2.5.1. Method of analysis

For a boron doped *p+ /n* junction, this method consists in the calculation, of the electrical parameters measured by Hall-effect (sheet resistance R_S, Hall dose $\langle N_H \rangle$, and Hall mobility $\langle \mu_H \rangle$) on the basis of the dopant chemical concentration profile measured by SIMS and of the dopant mobility vs. concentration relation [64]. As schematically shown in Figure 20, we first define from the chemical dopant profile measured by SIMS, $C(x)$, the active dopant concentration profile, $C_a(x)$, as follows:

$$C_a(x) = \begin{cases} C_{el} & for \quad C(x) \geq C_{el} \\ C(x) & for \quad C(x) < C_{el} \end{cases} \tag{7}$$

where C_{el} is the maximum active dopant concentration. In addition, we also assume that $C_a(x)$ is identical to the carrier concentration profile, $p(x)$. Starting from the hole concentration profile, $p(x)$, it is then possible to calculate the sheet resistance, R_S, of the *p+/n* junction, if the hole drift mobility vs. concentration relation, $\mu_p[p(x)]$, is known:

$$R_S = \frac{1}{q \int_0^{x_j} p(x) \mu_p[p(x)] dx} \tag{8}$$

where q is the electron charge and x_j the junction depth. From $p(x)$ and μ_p, it is also possible to calculate the Hall dose $\langle N_H \rangle$ and Hall mobility $\langle \mu_H \rangle$ obtained from Hall

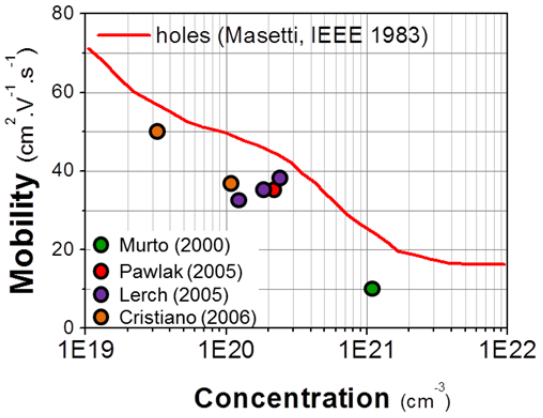

Figure 19 – Comparison between experimental hole mobility values (symbols) measured from heavily Boron-doped USJs and corresponding theoretical values (solid line).

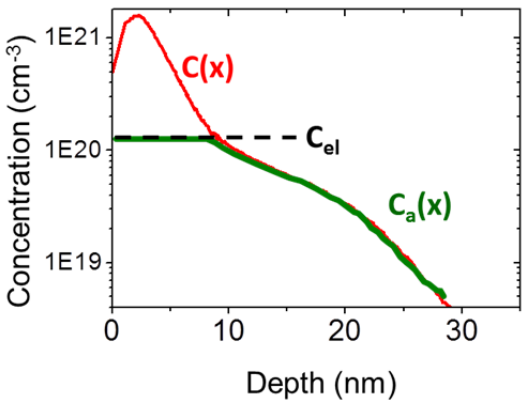

Figure 20 – Schematic description of the active dose profile (green) defined from the measured SIMS profile (red). All atoms located in regions with a concentration lower than C_{el} are assumed to be electrically active.

measurements [71]:

$$\langle N_H \rangle = \frac{\left[\int_0^{x_j} p(x)\mu_p[p(x)]dx\right]^2}{r_H \int_0^{x_j} p(x)\mu_p{}^2[p(x)]dx} \tag{9}$$

$$\langle \mu_H \rangle = \frac{r_H \int_0^{x_j} p(x)\mu_p{}^2[p(x)]dx}{\int_0^{x_j} p(x)\mu_p[p(x)]dx} \tag{10}$$

where r_H is the Hall scattering factor.

Finally, and in order to take into account the possible impact of BICs on the carrier mobility, we make the assumption that the presence of BICs induces an additional scattering center that reduces the hole mobility. We therefore define the effective drift mobility, μ_{eff}, as

$$\mu_{eff} = \alpha \cdot \mu_p \quad with \quad \alpha \leq 1 \tag{11}$$

where α is the mobility degradation coefficient. For a totally activated junction, α=1; while in the presence of a high concentration of BICs, we expect to find, for α, a value lower than unity. According to all previous assumptions, the equations above can therefore be rewritten substituting $p(x)$ by $C_a(x)$ and μ_p by μ_{eff}. In this way, from the SIMS profiles of the investigated samples and the mobility vs. concentration curves, the sheet resistance, Hall dose, and Hall mobility can be calculated from these equations and matched to the measured values using two fitting parameters: C_{el}, the maximum doping profile concentration, and α, the mobility degradation coefficient.

The actual active dose $\langle N_A \rangle$ and average mobility $\langle \mu \rangle$ are finally given by the following equations:

$$\langle N_A \rangle = r_H \langle N_H \rangle = \int_0^{x_j} C_a(x)dx \tag{12}$$

$$\langle \mu \rangle = \frac{\langle \mu_H \rangle}{r_H} = \frac{\int_0^{x_j} C_a(x)\mu_{eff}(x)dx}{\int_0^{x_j} C_a(x)dx} \tag{13}$$

2.5.2. Mobility degradation

We initially tested our model to investigate the possible impact of inactive Boron clusters on the Hall effect measurements. We started using some references structures expected to be fully electrically active, whose characteristics are therefore close to those used in literature for the determination of r_H, i.e. with flat concentration profiles and free from any defects [72]. An example is shown in Figure 21a, where the chemical dopant profile (obtained by SIMS) and the carrier concentration profile

(obtained by SCM[#]) are compared for a CVD-grown Boron-doped layer with a concentration of $3x10^{19}$ cm^{-3}. The superposition of the two profiles confirms that the dopant is fully activated. The ratio of the active dose determined by SCM to the measured Hall dose, yielded a value of 0.73 +/-0.1 for r_H, in good agreement with those reported in literature, which vary between 0.7 and 0.8 [73].

We then applied the same approach to ion implanted samples containing a high dose of inactive Boron atoms, to measure their impact on the value of r_H [72]. The example shown in figure Figure 21b refers to a 0.5 keV Boron implant ($1x10^{15}$ cm^{-2}) followed by a spike anneal at 1000°C. The SIMS B profile after annealing shows the typical static peak of such heavily doped junctions, a "kink" (indicated by an arrow) and, below this concentration level, a diffused tail. The kink indicates the concentration level above which B forms the BICs. In contrast to the case of fully activated structures, The SCM profile exhibits a flat region (over the first 10 nm) located below the static peak in the SIMS profile. The dopant in this structure is therefore not fully electrically active. In addition, the carrier concentration profile below the kink clearly follows the SIMS profile, indicating that all the boron atoms of the diffused tail are electrically active. The ratio of the active dose (determined by SCM or estimated by SIMS[##]) to the measured Hall dose, yielded in this case a value of 0.93 +/-0.1 for r_H, higher than in fully activated samples. Similar values (between 0.93 and 0.99) were found other highly doped structures, including pre-amorphised junctions annealed with either spike RTA, Flash or non-melt laser anneals.

The high density of BICs in high-dose boron-implanted USJs therefore has a

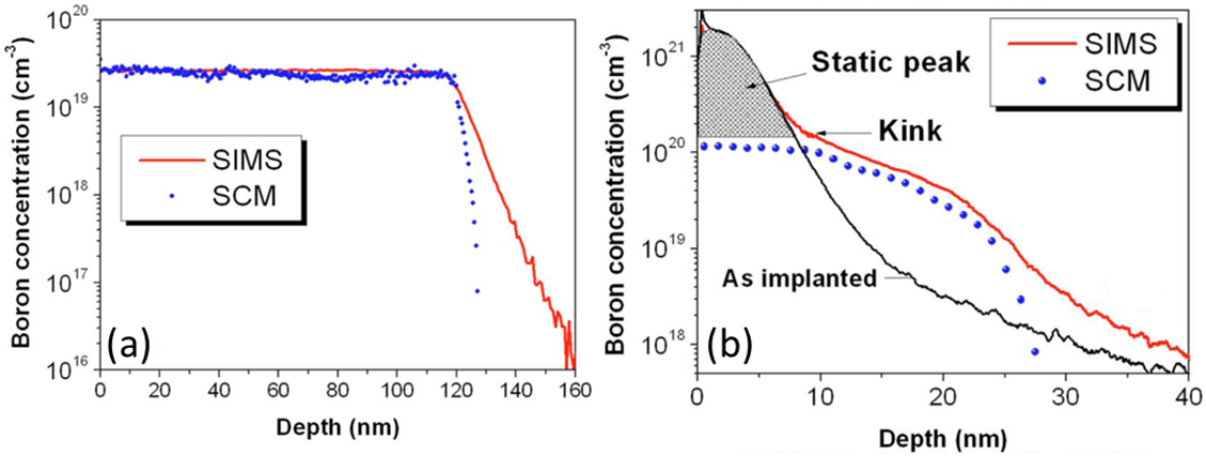

Figure 21 – Comparison between chemical Boron profiles obtained by SIMS (red lines) and carrier concentration profiles obtained by SCM (blue symbols) in B-doped junctions fabricated using different methods. (a) CVD-grown boron-doped sample. The good agreement between SCM and SIMS profiles confirms that all deposited dopant atoms are electrically active. (b) B-doped USJ obtained by low-energy ion implantation (0.5 keV B^+, $1x10^{15}$ cm^{-2}) and spike anneal at 1000°C. The Boron atoms contained in the immobile peak are electrically inactive.

[#] Scanning Capacitance Microscopy. Measurements were done by Filippo Giannazzo at the CNR-IMM laboratory of Catania

[##] It is possible to calculate the active dose of a boron-implanted sample which exhibits a kink in its SIMS profile, by calculating the total area below the kink concentration level.

strong impact on the r_H value for holes. Although the exact structure of BICs is not perfectly known, it has been shown that, for a successful simulation of B diffusion and activation in USJs, BICs must be assumed to exist in both neutral and charged state, with the majority of them being in the latter category [74]. It is also known that the r_H values of neutral and ionized impurities are equal to 1 and 1.93, respectively [75]. If the scattering centers associated to neutral and charged BICs are assumed to have the same impact on r_H as that of neutral and charged impurities, it is therefore expected that in the presence of BICs, the average r_H value must be higher than in the case of defect-free doped layer, in agreement with our results.

The second part of this activity was dedicated to the investigation of the mobility degradation in highly-doped USJs [76,77]. The investigated junctions were realized using the same pre-amorphisation and implantation conditions (30 keV Ge $1x10^{15}$ cm^{-2}) but different annealings, in order to obtain various fractions of Boron atoms contained in electrically inactive BICs (from 20% to 90% of the implanted dose). They also included a reference sample, realized by chemical vapor deposition (CVD) with low Boron concentration to minimise BICs formation.

Using the method of analysis described in section 2.5.1, we first calculated the Hall dose of all the investigated junctions, using the appropriate values of r_H (i.e. r_H=0.95 for all the implanted samples containing high densities of Boron inactive clusters and r_H=0.75 for the reference sample) and C_{el} as a fitting parameter (cf. eq.7) in order to match the measured Hall dose values. In all cases it was found that the C_{el} values were in good agreement with the position of the "kink" in the SIMS profiles. The second free parameter of our method of analysis (the mobility degradation coefficient, α, cf. eq. 11) was finally used to fit the measured values of sheet resistance and Hall mobility. It is important to note that for each investigated junction, a single value of α is found to allow a perfect matching of both measured values of sheet resistance and Hall mobility. Figure 22 reports the variation of α as a function of the density of Boron atoms contained in BICs, Φ_{BICs}. Error bars were taken equal to 15%

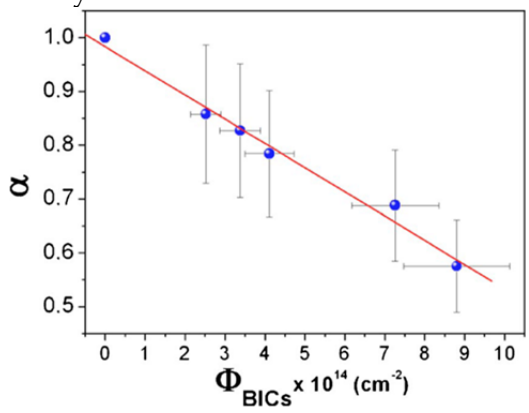

Figure 22 – Mobility degradation coefficient α as a function of BICs dose. The point found for the reference samples, free from any residual defects (Φ_{BICs}=0) and without mobility degradation (α=1) is also reported. Improvement of mobility is clearly observed when the BICs dose decreases.

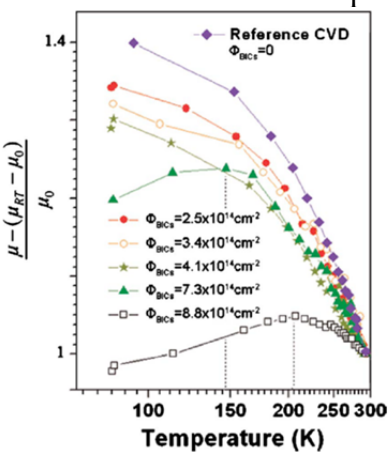

Figure 23 – Normalized curves of hole mobility vs temperature for the five studied samples containing various concentrations of BICs and the CVD-grown (BICs-free) reference sample.

for both α and Φ_{BICs}. The mobility degradation linearly increases (i.e., α decreases) when Φ_{BICs} increases, which confirms the direct impact of BICs on carrier mobility. In the case of the reference CVD-grown sample, no mobility degradation was measured and so α was found equal to unity. Considering that BICs dissolution occurs during annealing in highly-doped USJs, it is therefore expected that carrier mobility progressively approach the "standard" values as measured in samples without BICs.

We finally realized on these samples temperature-dependent Hall mobility measurements (from LN_2 to RT), which allow to experimentally isolate the different scattering mechanisms. Figure 23 reports the measured values normalized with respect to the one obtained at RT from the sample containing the maximum dose of inactive Boron atoms (black squares in Figure 23). Starting from RT, we can observe an initial increase of mobility for all samples when the measurement temperature decreases, typical of a dominant phonon scattering mechanism. This mobility increase is less effective in samples containing the highest densities of inactive Boron, suggesting that a second scattering mechanism is responsible for a decrease of the mobility. In fact, in these samples, the trend is inversed below a certain temperature (i.e. 200 K in the samples containing the maximum concentration of inactive Boron), where the mobility is found to decrease with decreasing temperature, which typical of a Coulomb scattering mechanism from ionised impurities.

All the observed behaviours discussed so far (temperature dependence of the mobility, increase of the mobility degradation and of the Hall scattering factor with BICs concentration) therefore indicate that BICs can be considered as independent scattering centers, which limit the holes mobility together with the other scattering mechanisms like phonon scattering and Coulomb scattering. These conclusions were also confirmed by other investigations where Hall measurements were compared to atomistic kinetic Monte Carlo simulations [78].

2.6. Formation of large BICs

As it was shown at the beginning of this chapter (cf. section 2.1.1), Boron deactivation is associated to the formation of Boron-Interstitial Clusters (BICs) typically evidenced by the presence of an immobile peak in annealed SIMS profiles [10]. Such profiles were successfully simulated assuming that cluster size remains small during annealing (less than 5 boron atoms) [6,11 and references therein]. However, most of the experimental studies on which these conclusions are based were carried on B delta-doped layers with peak concentrations in the range 10^{19}-10^{20} B/cm^3, i.e. much lower than the concentration values typically attained during *source/drain* (S/D) fabrication. The question therefore arose whether or not BICs formed after high-dose boron-supersaturated S/D implants can evolve up to much larger sizes and eventually towards stable precipitates, such as the SiB_3 and SiB_4 borides predicted by the Si-B phase diagram [21].

We will therefore summarise in the following sections the main findings of the research studies we have carried out over the last ten years in close collaboration with the CEMES laboratory, including the PhD thesis of Xavier Hebras [79], that I co-supervised with Alain Claverie and the post-doctoral activities of Nikolay Cherkashin, Simona Boninelli and Pier Francesco Fazzini. We investigated the crystallographic characteristics of the large Boron clusters (section 2.6.1), as well as their evolution during annealing (section 2.6.2).

2.6.1. Structure of large BICs

In our earliest experiment [80], Si (100) Si wafers were implanted with 500 eV Boron ions to a fluence of $1x10^{15}$ ions/cm^2 and annealed at 650°C and 750°C for times ranging from 2 to 160 sec in flowing N_2 or O_2. SIMS profiles (see Figure 24a) indicate that the boron peak concentration clearly exceeds the solubility limit value at the investigated temperatures. After a low thermal budget anneal (650°C 10 s, red curve in Figure 24a), it is not possible form the SIMS data to distinguish any (electrically inactive) immobile part of the profile from the (electrically active) mobile one, as typically found after higher thermal budget anneals (i.e. 1050°C, blue curve in Figure 24a). However, electrical measurements (4PP and SRP) indicate that the maximum Boron active concentration at 650°C does not exceed $2x10^{19}$ cm^{-3}, confirming that Boron clustering actually occurs at this temperature. In addition, high resolution analysis (Figure 24b) demonstrated that extended defects form at a depth corresponding to the Boron peak concentration (~3 nm) and that they consist of small dislocation loops lying on {100} planes with an interstitial character (Figure 24c). They are therefore different from the typical extended defects formed after precipitation of implantation induced excess Si_{int} atoms (cf. Chp. I). In addition, WBDF TEM analysis (not shown) indicated that during annealing they evolve following an Ostwald ripening mechanism, while upon oxidation the average size of the clusters increases. These results prove that the observed clusters are of the Boron-Interstitial type, i.e. BICs can be much bigger than generally assumed.

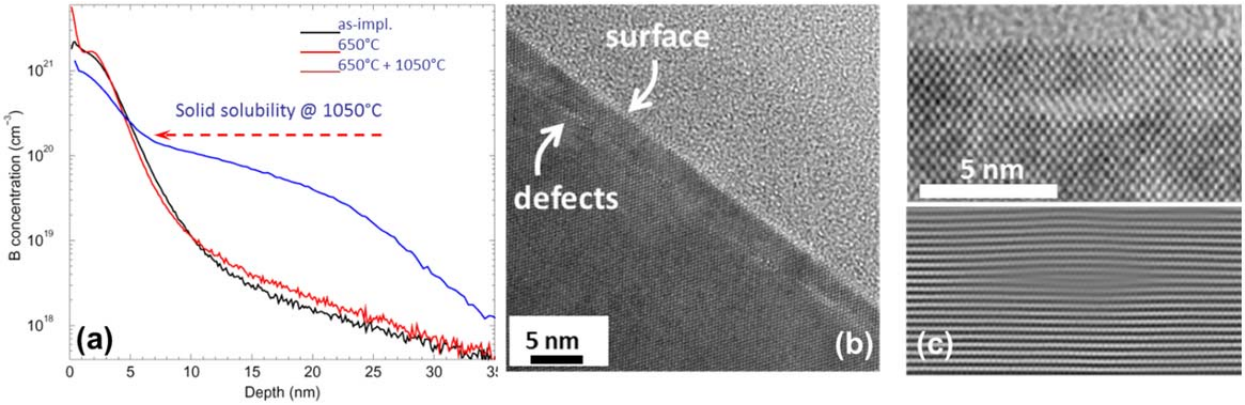

Figure 24 – *(a)* B SIMS profiles after implantation at 500 eV to a dose of $1x10^{15}$ cm^{-2}. Black: as-implanted. Red: annealed at 650 °C for 10 s. Blue: annealed at 650 °C for 10 s + spike anneal at 1050°C. *(b)* HREM cross-sectional image showing defects position at 2.5 nm below the surface. *(c)* Original HREM image of a defect (top) and Fourier filtered image (bottom) obtained using {200} diffracted spots.

Conventional TEM contrast analysis of dislocation loops (in WBDF conditions) was then used by Cherkashin to determine the crystallographic features of the large Boron clusters [81]. Figure 25 shows two typical WBDF images from the same area taken under different zone axes, ***B***, and diffracting vectors, ***g***. It is clear that the apparent density of clusters can vary by as much as a factor 100 depending on the imaging conditions. This implies that several variants of these defects must exist, with different habit planes and/or Burgers vectors, ***b***, that exhibit different contrast when changing the imaging conditions. The detailed TEM investigations indicated that five variants of these defects exist, all lying on a (001) habit plane. Four of them have a Burgers vector parallel to the [1 0 1], [-1 0 1], [0 1 1] and [0 -1 1] directions, respectively, while the fifth one has a Burgers vector parallel to the [0 0 1] direction, i.e. it is a pure edge dislocation. For this last defect variant, it has also been possible to determine the amplitude of the Burgers vector [81] by using the Geometric Phase Analysis (GPA) of HRTEM images [82], which was found equal to ~1/3 [001]. This is a smaller value than expected if the analysed defect was a pure Si platelet in the (0 0 1) plane (in such case the displacement associated to the defect would be ½ [0 0 1]). This result suggests that, indeed, atoms smaller than Si are contained in the defect (i.e. with a smaller covalent radius), therefore supporting all previous indications that the observed defects are large Boron-Silicon precipitates (BICs) containing several hundreds of atoms.

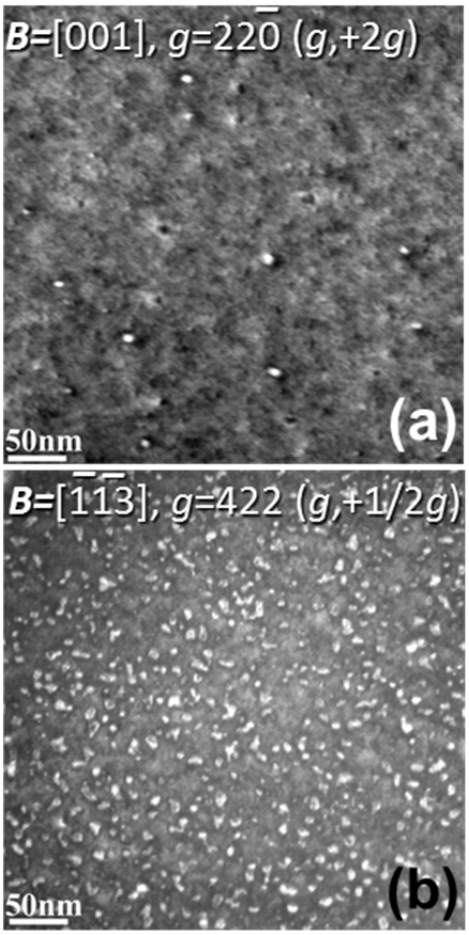

Figure 25 – WBDF plan-view micrographs of a Si sample implanted with 0.5 keV B^+, $1x10^{15}cm^{-2}$ after annealing at 650°C. The images are taken from the same area using different zone *axes*, ***B***, and diffracting vectors, ***g***.

A further confirmation about the origin of these large BICs came from a different experimental setup [83], in which a deep layer of substitutional Boron was grown by MBE ($2x10^{20}cm^{-3}$, located at 220 nm below the surface) and followed by a shallow Si^+ implant (R_p ~30 nm) and anneal at 815°C. During annealing, the Si_{int} atoms diffusing out from the Si^+ implant region, interacted with the Boron layer, resulting in the formation of large BICs evidenced again in the form of dislocation loops. In all these studies, the exact chemical composition of the observed clusters could not be determined. More recently, the development of the atom probe tomography (APT) technique [84] has made possible to measure the chemical composition of B-Si precipitates in boron supersaturated systems. For instance, recent experiments [85,86] showed that for annealing temperatures below 800°C, the boron concentration in the observed precipitates

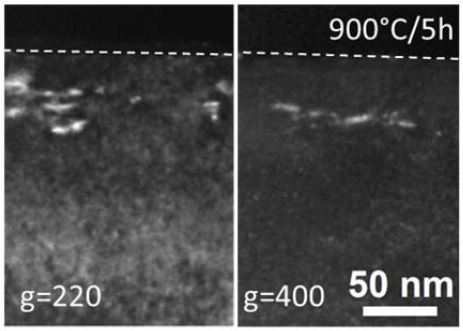

Figure 26 – Cross-section TEM micrographs (taken in WBDF imaging conditions) from a Si sample implanted with 10 keV B^+, $5x10^{15}$ cm^{-2} and annealed at 900°C for 5h: only elongated defects parallel to the (001) plane are observed independently of the diffracting vector (**g**=(220) or **g**=(400)).

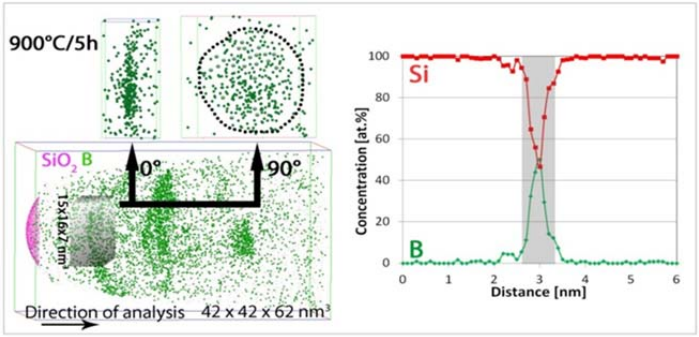

Figure 27 – (left) 3D elemental map of boron (green) taken from a Si sample implanted with 10 keV B^+, $5x10^{15}$ cm^{-2} and annealed at 900°C for 5h. B rich precipitates are observed with a platelet shape (see the side and the bottom view of one of these precipitates) and parallel to the surface, i.e. (001) plane. (right) B^{11} concentration profile through the precipitate shown in the zoomed areas using a sampling box of about 7x7x0.1 nm^3.

remains well below the expected value in "stable" boride phases (SiB3, SiB4 [21]). However, no direct evidence has yet been given that the various defects observed using different techniques (TEM, APT) actually correspond to the same objects. In a very recent experiment that we run in collaboration with the University of Rouen, where the APT technique has been developed [87], the experimental conditions were therefore carefully chosen (10 keV B^+, $5x10^{15}$ cm^{-2}, annealing up to 900°C 5 h) in order to investigate the Boron precipitation phenomenon by SIMS, TEM and ATP. As shown in Figure 26, large (001) loops are observed at a depth corresponding to the Boron peak concentration after annealing at 900°C for 5 h, while 3D boron reconstruction maps obtained by APT analysis (Figure 27) reveal the presence of boron-enriched zones at the same depth. Combining top and side views of the precipitates it results that they have a circular platelet shape, and lye parallel to the (001) surface plane, therefore corresponding to the (001) loops observed by TEM.

2.6.2. Thermal evolution of large BICs

In all the investigations discussed in previous section, the crystallographic characteristics of large BICs have been obtained after annealing at temperatures below 900°C. However, typical thermal cycles needed for the fabrication of USJs are run at much higher temperatures, as in RTA spike anneals (between 1000 and 1100°C) or ultra-fast Flash and Laser anneals (>1300°C).

In order to study the thermal stability of the defects during high temperature annealing, we initially investigated the case of a shallow 500 eV Boron implant (cf. Figure 24) subjected to an RTA 1050°C "spike" anneal. To this purpose, a series of samples was analysed, where the ramp-up that follows the pre-stabilisation step at 650°C was stopped at various intermediate temperatures between 800°C and 1050°C, as shown in Figure 28a. The corresponding TEM micrographs for a peak temperature of 800°C, 850°C and 950°C are reported in Figure 28b-d, respectively. They show that the defect density progressively decreases when increasing the peak temperature, while,

starting from temperatures higher than 850°C, also the apparent defect size is found to decrease, until their complete dissolution at peak temperatures of 1000°C and higher, when no defects have been observed. These results indicate that, when large BICs are located close to the surface (~3 nm), they cannot "survive" a typical RTA spike anneal cycle, after which only small "conventional" BICs containing few atoms (therefore undetectable by TEM) exist, as suggested by the immobile Boron peak observed in SIMS profiles even after long anneals at high temperatures (cf. Figure 24a).

Later works [88] investigated by SIMS the thermal evolution (up to 1000°C) of boron immobile peaks in high B-content systems (i.e. above solid solubility) located at 200 nm below the surface and showed that two B cluster dissolution regimes exist: a "fast" one, supposed to be associated to small BICs formed at low B concentrations and a "slow" one, associated to "larger and more stable" clusters. Indeed, the presence of large BICs in these structures, even at the highest annealing temperatures, was later proven by TEM investigations [83]. Moreover, their dissolution kinetics estimated from TEM images was found to be fully compatible with the slow regime identified by SIMS analysis. On the bases of all these results, physical models for the formation of BICs have recently been extended to include such large clusters, and have been used to provide successful simulations of boron diffusion and activation experiments [89,90].

Finally, in our latest experimental study [87], the experimental conditions were chosen in order to favor the formation of stable Boron precipitates at high annealing temperature (10 keV B^+, $5x10^{15}$ cm^{-2}, annealing up to 900°C 5 h, cf. Figures Figure 26 and Figure 27 in previous section). In this case, the maximum boron concentration (~$8x10^{20}$ cm^{-3}) exceeds the boron solubility limit in silicon for all the investigated temperatures. Boron is therefore expected to precipitate into immobile clusters. This is clearly visible at high temperature 900°C (see Figure 29a), showing that for concentration lowers than the solid solubility at this temperature ($7x10^{19}$ cm-3), Boron atoms have strongly diffused. In contrast, concentration profiles overlap with the as-implanted profile for higher concentrations (i.e. boron atoms are immobile at these concentrations). In addition, Atom Probe analysis showed that the Boron

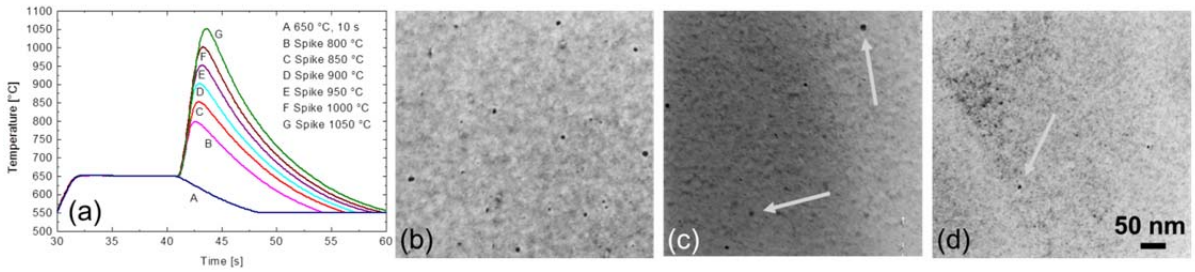

Figure 28 – *(a)*: Time-temperature profiles of several "spike" anneals with different peak temperatures (from 800°C to 1050°C) applied to samples implanted with 0.5 keV B^+, $1x10^{15}cm^{-2}$. All thermal cycles have the same pre-stabilisation step (650°C 10 sec) and the same ramp-up rate to the peak temperature (250°C/sec). *(b)-(d)*: Weak-Beam Dark-Field TEM micrographs (negative images) from samples with a peak temperature of 800°C, 850°C, and 950°C, respectively.

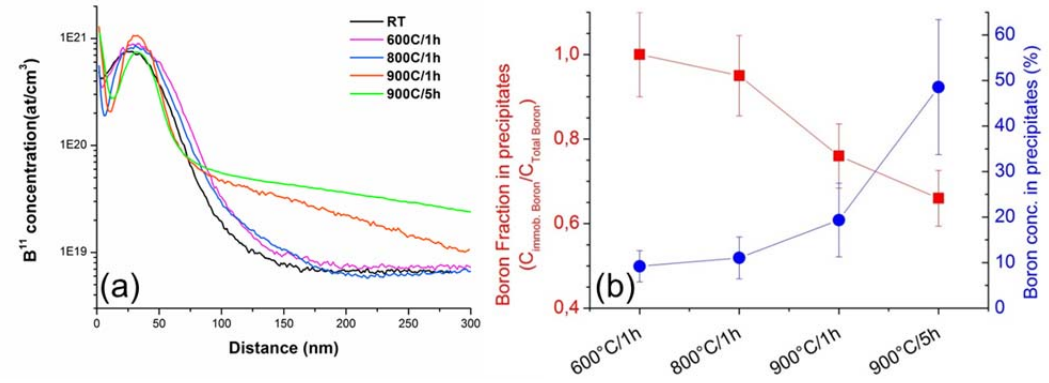

Figure 29 – (a) Boron SIMS profiles from samples implanted with 10 keV B^+, $5x10^{15}$ cm^{-2} and annealed for 600°C/1h, 800°C/1h, 900°C/1h, and 900°C/5h. (b) Fraction of boron atoms contained in the precipitates (red squares, left axis) and average Boron content in the precipitates (at. %, blue circles, right axis) as a function of the different annealing conditions.

concentration in the precipitates is found to continuously increase with increasing thermal budget (cf. Figure 29b, circles, right axis) up to an average value of 50 at.% at 900°C 5h, with isolated clusters reaching the stoichiometric SiB_3 composition (75 at.%). This demonstrates that precipitation induced by high-dose boron implantation can lead to the formation of the expected phase SiB_3. This result is in agreement with non-classical nucleation theories [91,92,93] predicting that coherent nuclei may precede the (incoherent) stable phase with a solute concentration (here boron) that gradually increases during annealing and finally reaches the equilibrium composition. It is important to note that earlier investigations carried out after low energy B implants (0.5 keV) indicated that (001)DLs Boron precipitates are not stable at high annealing temperature. When compared to them, the results presented here therefore demonstrate that the precipitation induced by high-dose boron implantation can indeed lead to the formation of the expected phase as given by the phase diagram (SiB_3), provided the Boron and interstitial supersaturations created by the implant are sufficiently high and far from the silicon surface to avoid (or retard) surface interstitial recombination.

2.7. Conclusions

The interactions between dopants, silicon and co-implanted impurity atoms, in the form of mobile species (BI pairs, free Si interstitials and vacancies…) or immobile clusters (silicon EOR defects, BICs, B precipitates, F-V bubbles…) give rise to several physical phenomena that affect the overall activation level of the implanted dopants. Some of these phenomena made the object of our work since 2003 and until today, with the latest investigations on the formation of large BICs in heavily p-type doped USJs. The main conclusions of our research can be summarised as follows:

- The **deactivation of Boron** atoms during post-annealing steps in pre-amorphised junctions is due to the formation of BICs induced by the flow of free interstitials diffusing out of the EOR defect region during annealing. The reactivation phase

observed after longer annealing times is due to the combination of two phenomena: the dissolution of BICs and the progressive diffusion of the Boron profile, both inducing a decrease of the sheet resistance.

- **Fluorine co-implantation** allows to reduce both B Transient Enhanced Diffusion and deactivation during annealing in pre-amorphised USJs. This beneficial effects cannot be associated to the modification of the EOR population by a F co-implant, but rather to the formation of independent F-related Si_{int} traps, including large cavities and/or SiF_4 molecules.
- **Boron trapping by EOR defects** during annealing strongly depends on the defect nature, with {311}s being more effective than DLs. On the basis of our investigations, we developed a Boron-trapping model that takes into account the nature of the trapping defects and which is today implemented in a commercial process simulators.
- The high density of **BICs** in high-dose boron-implanted USJs has a strong **impact** on the scattering value for holes, r_H, as well as **on the holes mobility**, with the mobility degradation linearly increasing as a function of the BICs concentration. BICs can therefore be considered as independent scattering centers, which limit the holes mobility together with the other scattering mechanisms like phonon scattering and Coulomb scattering.
- Finally, TEM investigations of highly doped Boron-implanted USJs showed that **BICs can be much larger than generally assumed** and, depending on the process conditions, can lead to the formation of the expected SiB_3 phase, as given by the phase diagram.

Overall, the understanding of these phenomena has contributed to the improvement of both the USJs fabrication methods and the physical models used in commercial TCAD simulators.

2.8. References

[1] W. K. Hofker, H. W. Werner, D. P. Oosthoek, and H. A. M. de Grefte, Appl. Phys. 2 (1973) 265

[2] W. K. Hofker, H. W. Werner, D. P. Oosthoek, and N. J. Koeman, Appl. Phys. 4 (1974) 125

[3] G.L.Vick, K.M.Whittle, J. Electrochem. Soc. 116 (1969) 1142

[4] A.E. Michel, W. Rausch, P.A. Ronsheim, R.H. Kastl, Appl. Phys. Lett. 50 (1987) 416

[5] N. E. B. Cowern, K. T. F. Janssen, and H. F. F. Jos, J. Appl. Phys. 68 (1990) 6191

[6] P. Pichler, Mat. Res. Soc. Symp. Proc., 717 (2002) C3.1.1; P. Pichler, *Intrinsic Point Defects, Impurities, and Their Diffusion in Silicon*, Springer Verlag, 2004

[7] A. Armigliato, D. Nobili, P. Ostoja, M. Servidori and S. Solmi, in: Semiconductor Silicon *1977*, edited by H. R. Huff and E. Sirtl, Electrochem. Soc., 1977, p.638

[8] T. Y. Tan. H. Foell, and W. Krakow. Inst. Phys. Conf. Ser. 60, I (1981)

[9] P.A. Stolk, H.-J. Gossmann, D.J. EagIesham, J.M. Poate, Nucl. Inst. Meth. B 96 (1995) 187

[10] L. Pelaz, M. Jaraiz, G.H. Gilmer, H.-J. Gossmann, C.S. Rafferty, D.J. Eaglesham, J.M. Poate, Appl. Phys. Lett. 70 (1997) 2285

[11] L. Pelaz, G. H. Gilmer, H.-J. Gossmann, C. S. Rafferty, M. Jaraiz, J. Barbolla, Appl. Phys. Lett. 74 (1999) 3657

[12] K.S. Jones, J. Liu, L. Zhang, Electrochem. Soc. Proc. Vol. 96-4 (1996) 116

[13] E. Landi, S. Guimaraes, S. Solmi, Appl. Phys. A 44 (1987) 135

[14] B.J. Pawlak, R. Surdeanu, B. Colombeau, A.J. Smith, N.E.B. Cowern, R. Lindsay, W. Vanderrvorst, B. Brijs, O. Richard, F. Cristiano, Appl. Phys. Lett. 84 (2004) 2055

[15] F.Khaja, B.Colombeau, T.Thanigaivelan, D.Ramappa, T.Henry, Proc. IIT10, ed. J.Matsuo et al., AIP 2010, p.65

[16] N.E.B. Cowern, J. Benson, A.J. Smith, W. Lerch, S. Paul, T. Graf, F. Cristiano, X. Hebras, D. Bolze, Appl. Phys. Lett. 86 (2005) 101905

[17] J.H.Kim, L.M.Rubin, J.Y.Yoon, M.S.Ameen, I.S.Jang, J.C.Cha, Y.H.Joo, A.B.Lee, S.W.Jin, Proc. IIT10, ed. J.Matsuo et al., AIP 2010, p.57

[18] F.Gonzatti, F.Milési, V.Delaye, J.Duchaine, F.Torregrosa, H.Etienne, K.Yckache, Proc. IIT10, ed. J.Matsuo et al., AIP 2010, p.27

[19] T.E. Seidel and A.U. MacRae, Prc. 1st Int. Conf. on Ion Implantation, Thousand Oaks, USA 1970. F.H. Eisen and C.S. Chadderton, eds., Gordon and Breach, London (1971), p. 169

[20] C. Bergaud, D. Mathiot, L. Lâanab, A. Claverie, A. Martinez, Porc. Of Ion Impl. Technol. Conf. 1994, Catania, p. 756.

[21] T.B. Massalski. "Binary alloy phase diagrams, 2nd edition", ASM International, Materials Park, 1996

[22] Y. Takamura, S.H. Jain, P.B. Griffin, J.D. Plummer, J. Appl. Phys. 92 (2002) 230

[23] W. Lerch, S. Paul, J. Niess, F. Cristiano, Y. Lamrani, P. Calvo, N. Cherkashin, D.F. Downey, E.A. Arevalo, J. El. Chem. Soc. 152 (2005) G787.

[24] F. Cristiano, N. Cherkashin, P. Calvo, Y. Lamrani, X. Hebras, A. Claverie, W. Lerch, S. Paul, Mater. Sci. Eng. B 114–115 (2004) 174

[25] F.Cristiano, Y.Lamrani, F.Severac, M.Gavelle, S. Boninelli*, N.Cherkashin, O.Marcelot, A. Claverie, W.Lerch, S.Paul, N.Cowern, Nucl. Inst. Meth. Phys. Res. B 253 (2006) 68

[26] P.A. Stolk, H.-J. Gossmann, D.J. Eaglesham, D.C. Jacobson, C.S. Rafferty, G.H. Gilmer, M. Jaraiz, P. Poate, J. Appl. Phys. 81 (1997) 6031

[27] S. Nishikawa, A. Tanaka, T. Yamaji, Appl. Phys. Lett. 60 (1992) 2270

[28] P.A. Stolk, D.J. Eaglesham, H.-J. Gossmann, J.M. Poate, Appl. Phys. Lett. 66 (1995) 1370

[29] N.E.B. Cowern, A. Cacciato, J.S. Custer, F.W. Saris, W. Vandervorst, Appl. Phys. Lett. 68 (1996) 1150

[30] F. Cristiano, C. Bonafos, A. Nejim, S. Lombardo, M. Omri, D. Alquier, A. Martinez, S.U. Campisano, P.L.F. Hemment and A. Claverie, Nucl. Instr. and Meth. B127/128 (1997) 22

[31] B.J. Pawlak, T. Janssens, B. Brijs, W. Vandervorst, E.J.H. Collart, S.B. Felch, N.E.B. Cowern, N. E. B., Appl. Phys. Lett., 89 (2006) 062110

[32] T. H. Huang, H. Kinoshita, and D. L. Kwong, Appl. Phys. Lett. 65 (1994) 1829

[33] H.W. Kennel, S.M. Cea, A.D. Lilak, P.H. Keys, M.D. Giles, J. Hwang, J.S. Sandford, S. Corcoran, Proc. IEDM'02 Proc, p. 875, IEEE 2002

[34] D.F. Downey, J.W. Chow, E. Ishida, K.S. Jones, Appl. Phys. Lett. 73 (1998) 1263

[35] J.M. Jacques, L.S. Robertson, K.S. Jones, M.E. Law, M. Rendon, J. Bennett, Appl. Phys. Lett. 82 (2003) 3469

[36] R. Duffy, V.C. Venezia, A. Heringa, B.J. Pawlak, M.J.P. Hopstaken, G.C.J. Mass, Y. Tamminga, T. Dao, F. Roozeboom, L. Pelaz, Appl. Phys. Lett. 84 (2004) 4283

[37] M. Diebel, S. Chakravarthi, S.T. Dunham, C.F. Machala, S. Ekbote, A. Jain, Mater. Res. Soc. Symp. Proc. 765 (2003) D6.15.1

[38] M. Diebel, S.T. Dunham, Phys. Rev. Lett., 93 (2004) 245901

[39] G. Impellizzeri, J.H.R. dos Santos, S. Mirabella, F. Priolo, E. Napolitani, A. Carnera, Appl. Phys. Lett. 84 (2004) 1862

[40] S. Boninelli, F. Cristiano, W. Lerch, S. Paul, N. E. B. Cowern, Electr. and Sol.-St. Lett., 10 (2007) H264

[41] D.A.Abdulmalik, P.G.Coleman, N.E.B.Cowern, A.J.Smith, B.J.Sealy, W.Lerch, S.Paul and F.Cristiano, Appl. Phys. Lett., 89 (2006) 052114

[42] S. Boninelli, A.Claverie, G.Impellizzeri, S.Mirabella, F.Priolo, E.Napolitani and F.Cristiano, Appl. Phys. Lett. 89 (2006) 171916

[43] S. Boninelli, G. Impellizzeri, S. Mirabella, F. Priolo, E. Napolitani, N. Cherkashin and F. Cristiano, Appl. Phys. Lett. 93 (2008) 061906

[44] D. De Salvador, G. Bisognin, E. Napolitani, M. Mastromatteo, N. Baggio, A. Carnera, F. Boscherini, G. Impellizzeri, S. Mirabella, S. Boninelli, F. Priolo and F. Cristiano, Appl. Phys. Lett. 95 (2009) 101908

[45] A. Mokhberi, R. Kasnavi, P. B. Griffin, and J. D. Plummer, Appl. Phys. Lett. 80 (2002) 3530

[46] J. Narayan, O. W. Holland, W. H. Christie, and J. J. Wortman, J. Appl. Phys., 57 (1985) 2709

[47] C. W. Nieh and L. J. Chen, Appl. Phys. Lett., 48 (1986) 1528

[48] C. Szeles, B. Nielsen, P. Asoka-Kumar, K. G. Lynn, M. Anderle, T. P. Ma, and G. W. Rubloff, J. Appl. Phys. 76 (1994) 3403

[49] P.J. Simpson, Z. Jenei, P. Asoka-Kumar, R.R. Robison, M.E. Law, Appl. Phys. Lett. 85 (2004) 1538

[50] X.D. Pi, C.P. Burrows, P.G. Coleman, Phys. Rev. Lett. 90 (2003) 155901

[51] R. Duffy, V.C. Venezia, A. Heringa, T.W.T. Husken, M.J.P. Hopstaken, N.E.B. Cowem, P.B. Griffin, C.C.Wang, Appl. Phys. Lett. 82 (2003) 3647

[52] T.E. Haynes, D.J. Eaglesham, P.A. Stolk, H.-J. Gossmann, D.C. Jacobson, and J.M. Poate, Appl. Phys. Lett. 69 (1996) 1376

[53] S. Nishikawa and T. Yamaji, Appl. Phys. Lett. 62 (1993) 303

[54] S. Lombardo, F. Priolo, S.U. Campisano and S. Lagomarsino Appl. Phys. Lett. 62 (1993) 2335.

[55] B. Colombeau, A.J. Smith, N.E.B. Cowern, B.J. Pawlak, F. Cristiano, R. Duffy, A. Claverie, C.J. Ortiz, P. Pichler, E. Lampin, C. Zechner, MRS Symp. Proc. 810 (2004) 91

[56] D. Alquier, PhD thesis, University of Toulouse, 1998

[57] J. Xia, T. Saito, R. Kim, T. Aoki, Y. Kamakura, K. Taniguchi, J. Appl. Phys. 85 (1999) 7597

[58] E.M. Bazizi, PhD thesis, University of Toulouse, 2010

[59] E.M. Bazizi, P.F. Fazzini, C. Zechner, A. Tsibizov, H. Kheyrandish, A. Pakfar, L. Ciampolini, C. Tavernier, F. Cristiano, Mat. Sci. Eng. B154-155 (2008) 275

[60] Sentaurus Process User Guide, (Synopsys, Inc., Mountainview, CA, 2010)

[61] A. D. Lilak, M. E. Law, L. Radic, K. S. Jones, and M. Clark, Appl. Phys. Lett. 81 (2002) 2244

[62] A. Mokhberi, P. B. Griffin, J. D. Plummer, E. Paton, S. McCoy, and K. Elliott, IEEE Trans. Electron Devices 49 (2002) 1183

[63] B. J. Pawlak, R. Surdeanu, B. Colombeau, A. J. Smith, N. E. B. Cowern, R. Lindsay, W. Vandervorst, B. Brijs, O. Richard, and F. Cristiano, Appl. Phys. Lett. 84 (2004) 2055

[64] G. Masetti, M. Severi, and S. Solmi, IEEE Trans. Electron Devices 30 (1983) 764

[65] W. R. Thurber, R. L. Mattis, Y. M. Liu, and J. J. Filliben, *The Relationship Between Resistivity and Dopant Density for Phosphorus- and Boron-Doped Silicon* (U.S. Dept. of Commerce, National Bureau of Standards, Washington, D.C., 1981)

[66] R. Murto, K. Jones, M. Rendon, S. Talwar, Proc. IIT 2000 Intern. Conf., IEEE (2000) p. 182.

[67] B. J. Pawlak, W. Vandervorst, A. J. Smith, N. E. B. Cowern, B. Colombeau, X. Pages, Appl. Phys. Lett. 86 (2005) 101913

[68] W. Lerch, S. Paul, J. Niess, S. McCoy, T. Selinger, J. Gelpey, F. Cristiano, F.Severac, S. Boninelli and P. Pichler, Mat. Sci. and Eng. B, 124-125 (2005) 24-31

[69] T. Clarysse, J. Bogdanowicz, J. Goossens, A. Moussa, E. Rosseel, W. Vandervorst, D. H. Petersen, R. Lin, P. F. Nielsen, O. Hansen, G. Merklin, N. S. Bennett, and N. E. B. Cowern, Mater. Sci. Eng., B 154-155 (2008) 24

[70] F. Severac, PhD thesis, University of Toulouse, 2009

[71] R. Baron, G. A. Shifrin, O. J. Marsh, and J. W. Mayer, J. Appl. Phys. 40 (1969) 3702

[72] F. Severac, F. Cristiano, E. Bedel-Pereira, P. F. Fazzini, W. Lerch, S. Paul, X. Hebras, and F. Giannazzo, J. Appl. Phys. 105 (2009) 043711

[73] Y. Sasaki, K. Itoh, E. Inoue, S. Kishi, and T. Mitsuishi, Solid-State Electron. 31 (1988) 5

[74] P. Pichler, C. Ortiz, B. Colombeau, N. Cowern, E. Lampin, S. Uppal, M.S.A. Karunaratne, J.M. Bonar, A.F.W. Willoughby, A. Claverie, F. Cristiano, W. Lerch, S. Paul, Phys. Scr. T126 (2006) 89

[75] P. Blood, J.W. Orton, The electrical characterization of semiconductors: majority carriers and electron states, Academic Press, London, 1992

[76] F. Severac, F. Cristiano, E. Bedel-Pereira, W. Lerch, S. Paul, and H. Kheyrandish, Mater. Sci. Eng., B 154-155 (2008) 225

[77] F. Severac, F. Cristiano, E. Bedel-Pereira, P.F. Fazzini, J. Boucher, W. Lerch and S. Hamm, J. Appl. Phys., 107 (2010) 123711

[78] M. Aboy, L. Pelaz, P. Lo pez, E. Bruno, S. Mirabella, Int. J. Numer. Model., 23 (2010) 266

[79] X. Hebras, PhD thesis, University of Toulouse, 2003

[80] F. Cristiano, X. Hebras, N. Cherkashin, A. Claverie, W. Lerch and S. Paul, Appl. Phys. Lett. 83 (2003) 5407

[81] N.Cherkashin, M.Hytch, F.Cristiano and A.Claverie, Solid State Phenomena, 108-109 (2005) 303

[82] M. Hytch, J.- L. Putaux, J.- M. Pénisson, Nature 423 (2003) 270

[83] S. Boninelli, S. Mirabella, E. Bruno, F. Priolo, F. Cristiano, A. Claverie, D. De Salvador, G. Bisognin, and E. Napolitani, Appl. Phys. Lett. 91 (2007) 031905

[84] B. Gault, F. Vurpillot, A. Vella, M. Gilbert, A. Menand, D. Blavette, and B. Deconihout, Rev. Sci. Inst.. 77 (2006) 043705

[85] M. Ngamo, S. Duguay, F. Cristiano, K. Daoud-Ketata, P. Pareige, J. Appl. Phys., 105 (2009) 104904

[86] O. Cojocaru-Mirédin, D. Mangelinck, and D. Blavette, J. Appl. Phys. 106 (2009) 113525

[87] O. Cojocaru-Mirédin, F. Cristiano, P-F. Fazzini, D. Mangelinck and D. Blavette, to be published

[88] D. De Salvador, E. Napolitani, G. Bisognin, A. Carnera, E. Bruno, S. Mirabella, G. Impellizzeri and F. Priolo, Appl. Phys. Lett. 87 (2005) 221902

[89] M. Aboy, L. Pelaz, P. López, E. Bruno, S. Mirabella, E. Napolitani, Mat. Sci. Eng. B, 154-155 (2008) 247

[90] M. Aboy, L. Pelaz, E. Bruno, S. Mirabella, S. Boninelli, J. Appl. Phys. 110 (2011) 073524

[91] J. W. P. Schmelzer, J. Schmelzer, I. Gutzow, J. Chem. Phys. 112 (2000) 3820

[92] T. Philippe and D. Blavette, J. of Chem. Phys. 135 (2011) 134508 1-3

[93] T. Philippe and D. Blavette, Phil. Mag. 91 (2011) 4606-4620

Chapter 3

New materials and processes for Ultra-Shallow Junctions

With the progressive introduction of advanced annealing processes and new substrate materials during the years 2000s, we dedicated some of our work to the investigation of implant-induced defects formation and their impact on USJ fabrication under these new conditions. This work, started in 2005 thanks to a direct collaboration with Mattson Thermal Products, who developed a Flash-RTP tool, was subsequently carried out mainly within the EU projects ATOMICS and PullNANO, where SOI and SiGe test wafers were provided Soitec and CEA-LETI, respectively.

A description of the general background leading to the introduction of advanced processes and materials in the semiconductor industry, together with the related open questions, relevant for our research, is presented in section 3.1. The following sections will then be devoted to our contributions in the field of millisecond Flash annealings (section 3.2), Silicon on Insulator (section 3.3) and Ge-based substrates (section 3.4).

3.1. Background

3.1.1. Advanced annealing processes

During the last four decades, device scaling allowed to continuously improve the MOS transistor performances on the basis of the "classic" Dennard model [1], where gate length, oxide thickness and junction depth are decreased by a constant factor in order to provide an improvement of transistor speed at a constant electric field.

Source/drain fabrication schemes have therefore evolved over the years to meet the increasingly challenging requirements associated with this model, both in terms of junction depth and dopant activation. Ultra-low energy implantation (<1 keV) is the today standard for the introduction of dopants by beamline implantation [2], with the option of combining it with a pre-amorphisation step and/or impurity co-implantation (as seen in Chp.2), while further improvements might come from the implementation of alternative doping technologies, such as molecular, cluster, cold and plasma implants.

Similarly, thermal annealing has evolved towards shorter cycles combined with higher temperatures, so to combine controllable diffusion with high activation [3], as expected since the early work of Michel *et al.* in 1987 [4]. According to the ITRS 2011 [5], currently used "spike" anneals, with ramping rates in the order of 250°C/s, are expected to be replaced with even faster methods operating in the millisecond scale, allowing to achieve, in planar bulk MOS, junction depths of ~10 nm (necessary to

minimise short-channel effects), while concurrently optimising the sheet resistance (~500 Ω/sq), the doping abruptness at the extension-channel junction and the extension-gate overlap. Whether these ultra-fast anneals are realised by scanning continuous wave lasers on the wafer surface (*non-melt laser anneals*) [6] or by a "flash" discharge of a high-power arc-lamp (*Flash anneals*) [7,8,9], the question arises whether these anneals are long enough to perform the intended actions (damage removal, dopant activation and diffusion to the expected depths). The difficulty comes from the different time constants of the several key physical processes occurring during junction fabrication at this timescale [10].

Within our group, we therefore investigated the evolution of implantation-induced extended defects during a msec Flash anneal in order to assess whether the basic mechanisms that control defect evolution are modified with respect to the conventional slower RTA anneals. In addition, we identified the best implant conditions than, combined to Flash anneals, allowed to improve the figures of merit of p^+-n USJs. The main results of these investigations will be reported in section 3.2.

3.1.2. New substrate materials : SOI and SiGe-based materials

However, since the early 2000s (and the 90 nm technology node), it became clear that device scaling simply based on the reduction of the feature size would not be sufficient to ensure the expected performance improvements, mainly because of the unsustainable increase of several deleterious effects associated with miniaturisation, such as the increase of parasitic capacitances between source/drain regions and the substrate (or the gate), which lead to an increase of the transistor delay time and switching power [11]. Another unwanted effect is represented by the increase of the transistor leakage current [12] (or standby current), I_{off}, due to the sum of several components: *(i)* gate leakage, due to increased direct tunneling favoured by the oxide thickness reduction below 1 nm; *(ii)* sub-threshold leakage, mainly due to threshold voltage variation at the chip level and caused by a multitude of effects, including gate length variation and random dopant distribution in the channel and *(iii)* junction leakage due to the drain-induced barrier lowering (DIBL) effect, favoured by the unbalanced reduction of gate length and junction depth.

The main consequence of these undesired effects was that the supply voltage could no longer be scaled as expected when moving from one technology node to the next, leading to a continuous increase of the transistor active power. A further consequence of this situation, known as the "power crisis" [12], was the delay of the gate length reduction [13] with respect to the ITRS predictions. Hence, transistor density increase was achieved by the aggressive scaling of the source/drain and contact size, so to compensate for the retarded gate length scaling [14]. This, in turn, further increased the already high parasitic resistances (and hence both the active and static power) associated to source/drain extension resistance, contact resistance at the silicide/silicon interface, and contact-via resistance.

In such a "catastrophic" scenario, technological progress by means other than scaling became therefore necessary for ensuring high-speed operation. Among the several proposed solutions, two were particularly interesting to us, due to their strong impact on the physical mechanisms governing the fabrication of source/drain junctions[#].

The first was the introduction of Silicon on Insulator (SOI) substrates. Indeed, the simple addition of an insulating layer between the body of the transistor and the substrate brings several advantages, including the drastic reduction of the parasitic capacitance between the source/drain junctions and the substrate, a reduced short channel effect, the absence of latch-up and the minimisation of body effect-related V_{th} variations, all leading to an improved speed and reduced power consumption in CMOS devices fabricated on SOI substrates [15].

An additional advantage of SOI is directly related to the fabrication of the source/drain regions and is given by the reduction of the number of silicon interstitial atoms created during the different implant steps, which can be directly captured in the buried oxide layer during the implant or diffuse and recombine at the buried Si-SiO_2 interface during annealing, leading in both cases to a better control of several deleterious effects, such as extended defect formation [16,17], dopant deactivation [18], and transient enhanced diffusion (TED) [19]. In the extreme case of ultra-thin SOI substrates (with a silicon overlayer thickness lower than ~10 nm), a further advantage occurs, as the junction depth is simply defined by the Si overlayer thickness rather than by the implant/anneal process parameters[##].

A particularly debated question concerned the experimental evidence of the beneficial effect of the buried Si-SiO_2 interface as well as the quantification of the interstitial recombination length at this interface. We contributed to this long-standing debate by investigating the evolution of extended defects and dopant diffusion in SOI materials through experiments and modelling. The main results of our work will be presented in section 3.3.

The second solution for the improvement of transistor performances, introduced to counterbalance the increasingly critical problems associated to device scaling, consisted in the introduction of SiGe-based materials for the increase of the channel carrier mobility, and hence the MOS "on-state" current, I_{on}. In general, carrier

---

[#] Other solutions include the introduction of new gate stack materials (high-k insulator and metal gate) or the development of new device architectures, such as double gate devices and more recently FinFETs and NW-based transistors

[##] However, when low-temperature dopant activation is achieved by pre-amorphisation, the role of the buried Si-SiO_2 interface remains critical even in Ultra-Thin SOI substrates, due to the interface's impact on the EOR defect dissolution.

mobility enhancement can be achieved using multiple methods, which can be grouped in three main families [20,21]: *(i)* strain engineering, *(ii)* hybrid-orientation technology and *(iii)* silicon replacement by high-mobility substrates.

Concerning strain engineering, SiGe-based materials are used in different ways depending on the addressed carrier type [22]. For instance, in PMOS, uniaxial compressive strain in the silicon channel is achieved by the selective epitaxial growth of pseudomorphic SiGe layers in the source/drain region, which results in the increase of the holes' mobility in the channel. In the case of NMOS, tensile biaxial strain (beneficial for the increase of electron mobility) is instead achieved in the silicon channel by epitaxially growing it on top of a relaxed defect-free SiGe layer[#].

Although it is expected that the use of strain engineering methods as a mobility enhancer will continue for several years as a key contributor to the CMOS scaling roadmap [23], some of the drawbacks associated to strain engineering methods (bandgap decrease, defect formation) may mitigate its beneficial impact in future device generations [24]. The use of new channel materials, exhibiting intrinsically higher carrier mobility than silicon, therefore represents the "ultimate" solution for the mobility enhancement issue. Among them, III-V materials and Germanium are the most promising candidates. In particular, Germanium is promising since both electron and hole bulk mobilities are improved with respect to silicon [25], while they can be further enhanced by strain [26]. Finally, the successful development of high-k/Ge gate stacks has allowed to overcome the "historical" problem related of the insufficient surface passivation provided by thermal oxidation [27], which has further renewed the interest towards Germanium as a high-mobility substrate.

The integration of SiGe (strained or relaxed) and Germanium in CMOS technology required an enormous effort in terms of research in order to achieve in few years for these materials the same level of knowledge accumulated in the case of silicon during several decades. Concerning the fabrication of source/drain junctions, the main issue to be addressed can be summarised as the need to understand how (and how much) the increasing germanium content in a SiGe alloy (up to pure germanium), and the possible strain associated to its growth on a Si substrate, modify the physical mechanisms occurring during the junction formation, including damage formation, amorphisation and recrystallization, the formation of extended defects during post-implantation annealing and the associated leakage currents, dopant activation and diffusion under equilibrium and non-equilibrium conditions.

In our group, we addressed since 2008 some of these issues which will be presented in section 3.4. In particular, we investigated the formation of extended defects in strained and relaxed SiGe alloys (section 3.4.1) and the dopant activation

---

[#] Other strain engineering solutions involve the use of different materials, such as SiC (for the uniaxial tensile strain in NMOS), or silicon nitride (for the fabrication of "dual stress liners" enveloping the gate).

stability in Germanium junctions fabricated by solid phase epitaxial regrowth (section 3.4.2).

3.2. Millisecond Flash annealing

As it was mentioned in the introduction of this chapter, the realisation of ultra-shallow junctions for future CMOS technology nodes requires, in parallel to the improvement of the implantation methods, the development of new thermal activation processes that provide maximum dopant activation with a limited thermal budget. To this respect, the annealing technology's roadmap [5] identifies millisecond anneals (flash or laser) as the most suitable potential solution to near "diffusionless" junctions. For example, in the Flash-assisted RTP process [28], a very high peak temperature (~1300°C) is reached, with a peak width of 1.6 msec.

The advantage of these ultra-fast methods was already clearly demonstrated in the mid-2000s as shown in Figure a, where several annealing methods are compared in terms of the two main USJs' figures of merit, x_j and R_S, for a fixed implantation scheme (PAI + B^+ implant). Indeed, a junction depth as shallow as 15 nm can be achieved using Low-temperature Solid Phase Epitaxial Regrowth [29]. However the corresponding sheet resistance exceeds 750 Ω/sq. On the other hand, a RTA-spike anneal [30] results into a much lower sheet resistance (~500 Ω/sq.), but induces a non-negligible Boron diffusion (x_j ~ 40nm). It appeared that the best compromises were achieved with millisecond Flash anneals [29,31] that allow sheet resistance values as low as ~350 Ω/sq. [29] or with non-melt laser anneals [32,33] that efficiently limit the dopant diffusion so that extremely shallow junctions can be fabricated (x_j <20 nm).

Concerning the implantation schemes involving the use of co-implanted impurities that were discussed in the previous chapter, several published data existed where these implants were followed by a spike RTA anneal, as shown in Figure

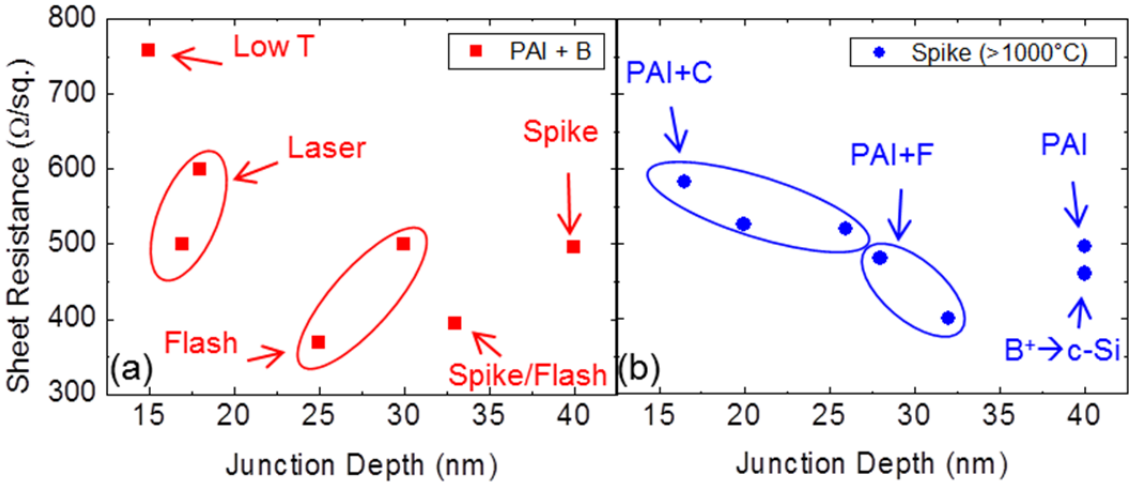

Figure 1 – x_j/R_S plots of USJs fabricated using various "Implant + RTA" methods. (a) Fixed implant method (PAI+Boron) followed by different annealing shames. (b) Fixed annealing method (Spike RTA) proceeded by different implant schemes.

b. It appeared that the sheet resistance value did not exhibit a strong dependence on the implant method used, as it ranged from 400 to 600 Ω/sq. for all the considered implants. On the other hand, the junction depth x_j was strongly affected, with the F^+ [34,35] or C^+ [36,37] co-implantation schemes resulting in the shallowest junctions, especially when C^+ co-doping is optimized.

On the basis of these known results, we therefore decided to investigate the combination of F^+ and C^+ co-implants with millisecond Flash anneals, in order to push to the limits the USJ fabrication methods based on conventional beamline implant. The results of this activity will be presented in section 3.2.2. Before that, we will present a more fundamental study on the evolution of implantation-induced defects during millisecond anneals.

Indeed, with such short annealing times achieved during Flash RTP or laser anneals, the question arose of whether this process could provide a complete dissolution of the implantation-induced defects, despite the high temperatures involved, as defects are known to have a strong impact on device leakage characteristics, if located close to the junctions, as well as on dopant diffusion and activation anomalies. Since our first investigations [29], it was clear that the EOR defects formed after a pre-amorphisation step are not fully dissolved even for Flash temperatures up to 1325°C. Similar results were obtained in the case of non-melt laser anneals [33]. We therefore decided to investigate this issue in more depth to determine if and how the defect formation mechanism is modified with respect to the slower RTA anneals. The corresponding results will be presented in section 3.2.1.

The whole activity on the implementation of millisecond Flash anneals for USJ fabrication was carried out in close collaboration with Mattson Thermal Products, Dornstadt, within two EU projects (ATOMICS and PullNANO) and involved the PhD work of Fabrice Severac [38] and Mehdi Bazizi [64].

3.2.1. Defect formation during msec Flash anneals

As mentioned in the previous section, a single Flash anneal step is not sufficient to completely dissolve the amorphisation-induced End of Range (EOR) defects. While these results led to new studies in which Flash anneals were combined with conventional spike Rapid Thermal Anneals (RTA) to achieve a complete defect dissolution [39,40], the reasons for this behaviour needed to be better understood. Indeed, on one hand, it is expected that the high temperature reached during a Flash anneal should induce a better defect dissolution, however, the very short annealing time might not be enough to activate the defect ripening. In addition, the very high ramp rates associated to the Flash anneals (~10^6 °C/sec) might even induce a modification of the defect evolution mechanism itself, as proposed by Camillo-Castillo *et al.* [41], who measured a different activation energy for the defect dissolution with respect to conventional anneals.

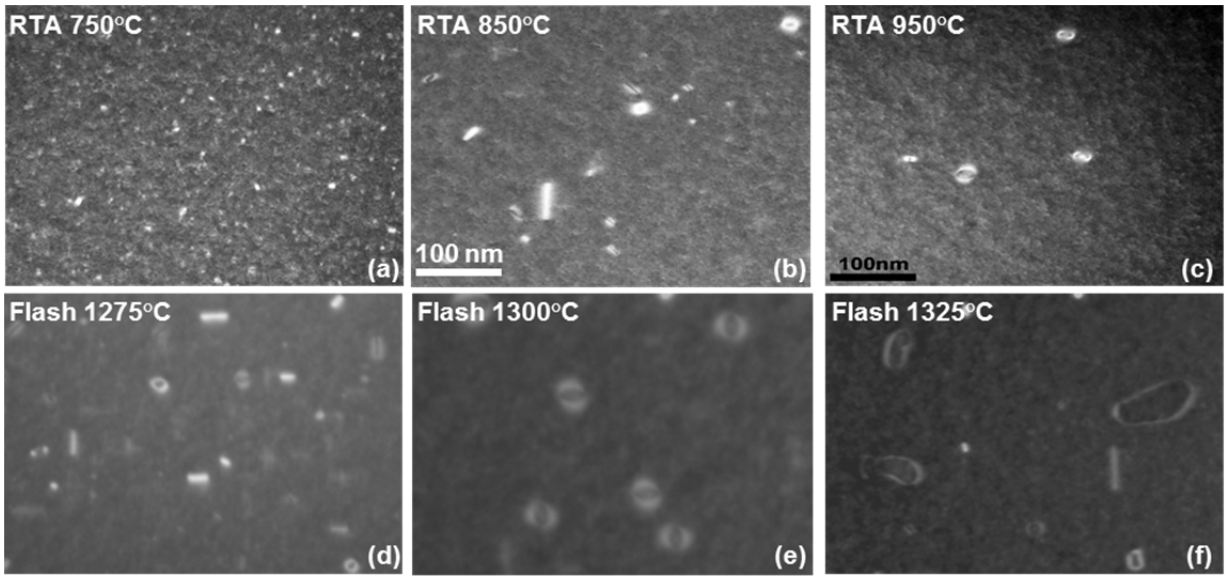

Figure 2 – Weak Beam Dark Field TEM micrographs from silicon samples amorphised with 30 keV Ge^+ ions to a dose of $1x10^{15}$ cm^{-2} and annealed using either a 30 sec "soak" RTA, (a-c), or a millisecond Flash anneal, (d-f).

In order to answer this question, we investigated a series of samples which were all amorphised with 30 keV Ge^+ ions to a dose of $1x10^{15}$ cm^{-2} and annealed using either RTA, between 750°C and 950°C, or Flash anneals, between 1275°C and 1325°C [42]. The corresponding Weak Beam Dark Field TEM micrographs are presented in Figure 2. For the 30 sec isochronal RTA anneals shown in Figure 2(a-c), the well-known defect evolution behaviour is observed, with the {311} defects formed at 750°C progressively transforming into dislocation loops of two types (perfect and faulted dislocation loops) at 850°C until, upon a further temperature increase (950°C, Figure 2c), only faulted dislocation loops are observed. At the same time, the overall defect population density progressively decreases, while the average defects size increases, which is typical of an Ostwald ripening process.

For the case of a millisecond Flash anneal (Figure 2 (d-f)) the limited investigated temperature range (1275-1325°C) does not allow to observe the complete evolution described above. However, it is evident that, similarly to the RTA annealed samples, the defect population, already consisting of dislocation loops at 1275°C, progressively decreases in density and increases in size when the Flash peak temperature is increased. In addition, a previous study [43] showed that the defect population after a Flash anneal at 1100°C consisted only of {311} defects.

These results therefore suggest that, at least qualitatively, the fast ramp-up and ramp-down rates used in msec Flash anneals do not modify the fundamental mechanisms of defect evolution. Nevertheless, if we compare for example the defect population after a 30 sec RTA anneal at 950°C (Figure 2c) with that observed after a msec Flash anneal at 1275°C (Figure 2d), we can conclude that, although the average defect size is similar in the two cases, the defect density is much lower in the RTA annealed sample (i.e. RTA is more effective in dissolving defects). The differences between the defect populations after a Flash or a RTA anneal can be understood if we consider that the overall evolution of a defect population is the result of several

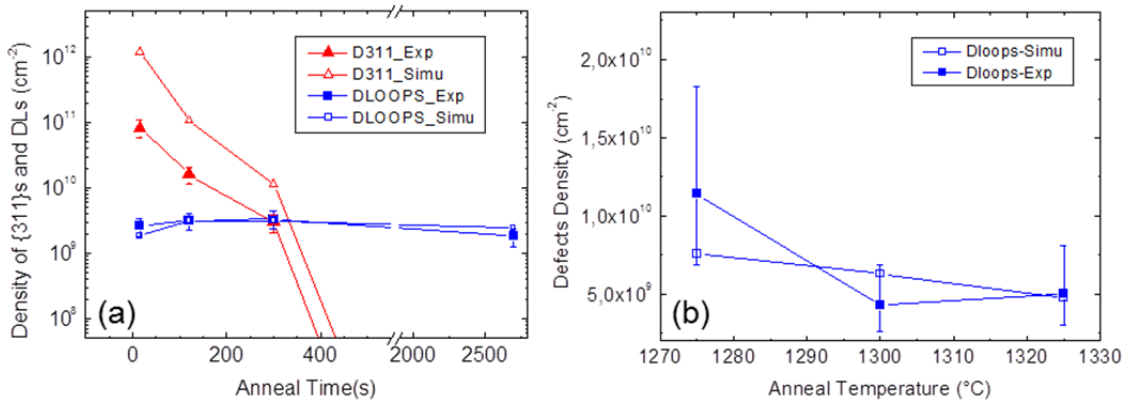

Figure 3 – Experimental (filled symbols) and simulated (empty symbols) evolution of the density of extended defects for a 30 keV Ge^+ implant to a dose of $1x10^{15}$ cm^{-2}. (a) RTA annealing at 800°C: defect evolution as a function of annealing time. (b) Millisecond Flash annealing: defect evolution as a function of peak annealing temperature.

concomitant mechanisms, which in most cases are thermally activated, such as the diffusion of the free Si interstitials that compose the defects, the interstitial capture from a given defect, the emission of interstitials from a defect and the transformation of {113} defects into dislocation loops. It is therefore not surprising that the different activation energies of each one of these mechanisms combine in a way that makes RTA and Flash anneals being "non-equivalent" in terms of defect evolution.

In order to verify this hypothesis, we used the "moment-based" defect model [44,45], already mentioned in Chp 1 (cf. section 1.5.3), in which the number of differential equations necessary to fully describe the evolution of defects size-distributions during annealing is drastically reduced with respect to the original "FRENDTECH defect model" (cf. section 1.5.3). A more detailed description of the "moment-based" model will be given in section 3.4.1 of this chapter. We first calibrated the model parameters using TEM data from silicon samples implanted with 30 keV Ge^+ to a dose of $1x10^{15}$ cm^{-2} and RTA-annealed at 800°C for various times [46]. We found that the simulations of the defect density evolution (cf. Figure 3a) perfectly reproduce most of the main features of the observed behaviour, including the transition of {113} defects into dislocation loops, and the total density of Si interstitial atoms stored in the defects. We then simulated the defect evolution in the Flash-annealed silicon samples shown in Figure 2(d-f). The experimental values of the defect densities are reported in Figure 3b (filled symbols). A very good agreement is obtained between the experimental and calculated values (empty symbols), with the simulations succeeding, within the large uncertainties of the experimental data, in predicting the observed decrease in the loop density as a function of the Flash peak temperature. It is important to note that, with the exception of the annealing temperature and time, all the simulation parameters, including all the thermally activated ones, were not modified with respect to the simulations of the RTA-annealed samples.

We could therefore reasonably conclude that, during the ultra-fast temperature ramp-up and ramp-down occurring in a msec Flash anneal, the basic mechanisms

		Fluorine				Carbon						
		Sample no.				Sample no.						
		1	2	3	4	5	6	7	8	9	10	11
Substr.	*n*-type Si wafer	X	X	X	X	X	X	X	X	X	X	X
Ge PAI	5 keV Ge – 5e14				X							X
	5 keV Ge – 1e15									X	X	
	10 keV Ge – 5e14			X					X			
	15 keV Ge – 5e14						X	X				
	20 keV Ge – 5e14	X				X						
F impl.	4 keV F– 1e15				X							
	10 keV F – 1e15	X	X	X								
C impl.	1 keV C – 1e15									X	X	X
	2 keV C – 1e15								X			
	4 keV C – 1e15						X	X				
	6 keV C – 1e15					X						
B impl.	0.2 keV B – 7e14				X			X			X	X
	0.5 keV B – 1e15	X	X	X		X	X		X	X		

Table 1 – Description of the different implant recipes used for the investigation of USJs fabricated with millisecond Flash anneals.

that control the growth and evolution of defects are not modified with respect to the relatively slower annealing processes, such as "soak" and "spike" RTA.

3.2.2. USJs optimisation with Flash anneals

The figures of merit that describe the USJs quality (sheet resistance and junction depth) depend on both the implant and anneal schemes chosen for their fabrication. The assessment of the best fabrication processes involving a millisecond Flash anneal therefore required to investigate a large amount of fabrication conditions, where several process parameters were varied, including dopant implant energy, pre-amorphisation depth, impurity co-implantation and combination of Flash and "spike"-RTA anneals. Such experiments were rendered possible within the EU Integrated Project PullNANO (2006-2009), whose objectives included the identification of suited USJs fabrication process for the 32 nm CMOS technology node. As an example, the table below summarises the different wafers investigated in this study [47].

Starting from a reference implant condition with 20 keV Ge^+ pre-amorphisation (PAI) followed by either 10 keV F^+ (wafer 1) or 6 keV C^+ (wafer 5) and a 0.5 kV B^+ implant, the energy of PAI Ge^+ ions was downscaled down to 5 keV in order to investigate the role of the position of the a/c interface on the final dopant activation. In some cases, the reduction of the PAI dose was also considered. In general, the energy of the co-implanted impurity was downscaled together with that of the Ge^+ PAI, in order to keep a constant relative location between the co-implanted impurity profile and the PAI-induced EOR defects. Finally, for the most aggressive implant schemes, the Boron implant energy was reduced from 0.5 keV to 0.2 keV. Following the implants, all wafers were annealed according to four different recipes, including

conventional Spike RTA and millisecond Flash RTA: (1) Flash RTA only at 1300°C; (2) Spike 1000°C + Flash 1300°C; (3) Spike 900°C + Flash 1300°C and (4) Spike only at 900°C.

The assessment of the various annealing recipes is presented in Figure4. In particular, Figure 4a shows SIMS profiles measured from wafer 1 (20 keV Ge^+/10 keV F^+/500 eV B^+) following the four different annealing conditions considered in this study. The best results, both in terms of junction depth[#] and sheet resistance are clearly obtained in the sample annealed only with Flash at 1300°C (black line in Figure 4a, x_j = 17.4 nm, R_S = 408 Ω/sq.). In addition, also the "kink" concentration (above which Boron atoms are immobile and electrically inactive) is highest in this sample (~4×10^{20} cm^{-3}), which corresponds to the Boron solid solubility at 1300°C. All other anneal schemes resulted in deeper junctions (determined by Boron TED occurring during the spike RTA) and higher values of sheet resistance. A very similar trend was found in samples co-implanted with C^+, as shown in Figure 4b, that reports data obtained from wafer 5 (20 keV Ge^+/6 keV C^+/500 eV B^+). Again, the best results came from the sample annealed only with Flash at 1300°C (black line in Figure 4b, x_j = 15.6 nm, R_S = 465 Ω/sq.).

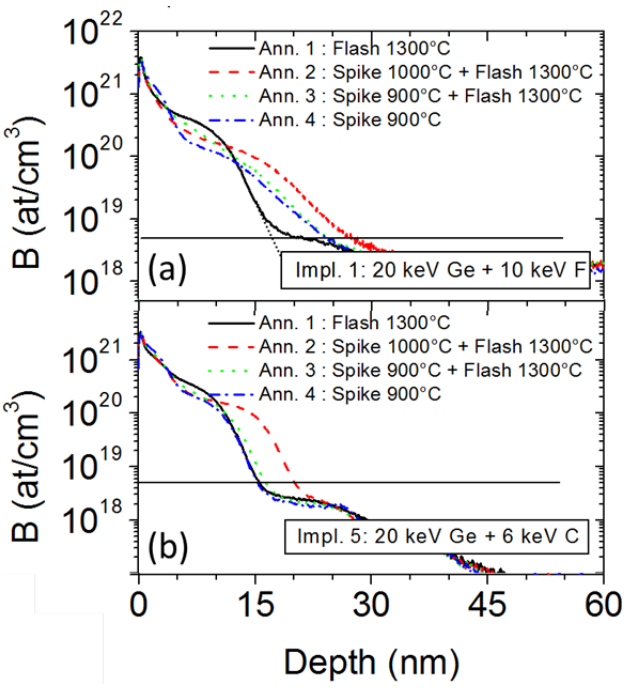

Figure 4 – Boron SIMS profiles from (a) wafer 1 (20 keV Ge^+/10 keV F^+/500 eV B^+) and (b) wafer 5 (20 keV Ge^+/6 keV C^+/500 eV B^+) following different annealing conditions: Flash only (*black*). Spike 1000°C + Flash (*red*). Spike 900°C + Flash (*green*). Spike only at 900°C (*blue*).

The results obtained from all the implanted wafers (cf. Table 1) after a "Flash-only" anneal at 1300°C are presented in Figure 5a, where the blue and green symbols correspond to the 500 eV and 200 eV B^+ implanted samples, respectively. It can be observed that, independently of the B^+ implant energy, the Carbon co-implanted structures (triangles) systematically exhibit shallower and more resistive junctions than fluorine implanted ones (circles). The reduced boron diffusion in C^+ co-implanted structures is probably due to the difference in the Si Interstitial capture efficiency of F and C (responsible for the reduction of B diffusion). As seen in previous chapter (cf. section 2.3.2), the capture of a Si interstitial atoms in a Fluorine co-implanted structure requires the implication of several Fluorine atoms, whether

[#] x_j is taken at a concentration of 5×10^{18} cm^{-3}. For this sample, the value was extrapolated from higher concentrations (see dotted black line in Figure 4a) to account for the fact that B^+ ions were implanted in deceleration mode.

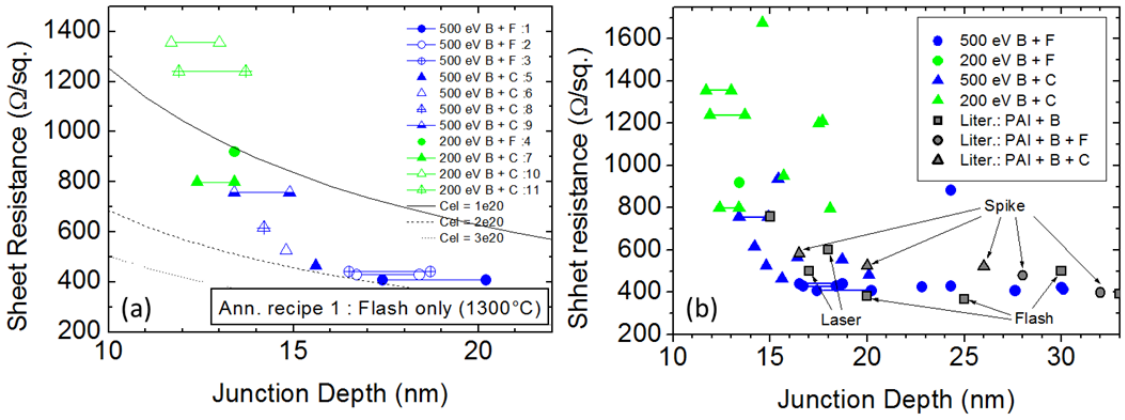

Figure 5 – R_S/x_j plots from USJs fabricated using different implantation and annealing schemes (cf. Table 1). Blue symbols: 0.5 keV B^+. Green symbols: 0.2 keV B^+. (a) All implant recipes followed by a "Flash-only" anneal at 1300°C. Black lines: R_S/x_j curves from box-like junctions with various active dopant concentrations. (b) All implant and annealing schemes. Grey symbols: Literature data

this occurs directly through the formation of SiF_4 molecules [48] or indirectly through the formation of F-Vacancy (F-V) clusters containing several F atoms (such as F_3V or F_4V [49]), i.e. the capture efficiency of F is estimated to be not higher than ~0.3 Int/F at. In contrast, the capture efficiency of C has been estimated in the order of 1.2 Int/C at. [50,51].

In a miniaturisation strategy that considers x_j as the most critical parameter, it is therefore evident that C co-implantation has to be preferred over F co-implantation, possibly coupled with a reduced B^+ implant energy, with junctions as shallow as 11.7 nm (R_S=1355 Ω/sq.) being achievable. Alternatively, if the sheet resistance is considered as the most critical parameter in the junction fabrication, then the best results are obtained from 10 keV F^+ co-implanted structures with 500 eV B^+ (blue circles in Figure 5a), with sheet resistance values around 400 Ω/sq. (and junction depths of no more than 17 nm).

Finally, Figure 5b (blue and green symbols) reports the totality of the results obtained in this work (all implant and annealing schemes) together with a selection of previously published data [29,30,31,33,34,35,36,37] (grey symbols). These results demonstrate that, when using a Flash annealing step, an improved quality of the fabricated junctions is demonstrated with respect to C co-implanted junctions annealed with Spike (refs. 36 and 37) as well as to preamorphised junctions annealed with non-melt laser (refs. 33 and 35). In addition, several of the fabrication schemes investigated in this work, satisfied the initial targets for the 32 nm CMOS technology node.

To conclude, it is important to note that, although nowadays it has become more and more difficult to achieve the USJs characteristics required by the ITRS (junctions as shallow as 7.3 nm are foreseen for the last technology node based on planar bulk MOS, i.e. 22 nm in 2015 [5]), millisecond Flash anneals remain among the most performant annealing method to be implemented in future device generations, together with Laser anneal.

3.3. Silicon On Insulator

The behaviour of the buried Si-SiO_2 interface with respect to the implant-generated interstitial excess has been a longstanding subject of research and, with the exception of few reports suggesting that the interface has no impact at all on dopant diffusion [52] or acts has a reflective boundary for interstitials [53], the vast majority of previous reports have shown that it behaves as an efficient sink for interstitials [16, 18,19,54,55,56]. Several physical phenomena have been investigated in these studies which give a more or less direct evidence of the interstitial recombination at the Si-SiO_2. In some cases, a quantitative estimation of the recombination length for interstitials at the interface, L_{int}, has also been given. However, one of these studies was based on the observation of the Boron pile-up at the Si-SiO_2 interface [55], which is difficult to measure by SIMS (Secondary Ion Mass Spectroscopy) due to the change of sputtering and ionisation rate at the interface and also strongly depends on the SOI fabrication method [57]. Others were based on the investigation of boron deactivation due to silicon interstitial atoms emitted by end-of-range defects [18,56]. This requires the concomitant use of structural and electrical measurements (TEM, SIMS, Hall-effect), and several strong assumptions for their quantitative modelling.

In our studies we decided to use two different methods to investigate this issue: The first is based on the TEM analysis of the formation and evolution of implantation induced extended defects in SOI, as the interstitials capture at the buried Si/SiO_2 interface is expected to induce a decrease in the number of Si interstitials in the defects, compared to bulk Si. This is probably the least "indirect" among all methods, as defects are precipitates of Si interstitials. However the large experimental errors associated to the counting of atoms contained inside the defects (no less of 25%) makes it difficult to achieve a fine quantitative analysis of the interface effect.

The second was based on dopant diffusion studies. In the particular case of *in-situ* grown dopant marker layers, they are expected to provide the most reliable estimation of L_{int}, as they only rely on SIMS measurements and dopant diffusion modelling. Indeed, these have been used in the past to show and quantify the interstitial recombination at the silicon surface (L_{surf}) [58,59,60,61]. However, when applied to SOI, this method was mainly used to study oxidation-enhanced diffusion [54], yielding L_{int} values (>1 µm above 800°C) much larger than those proposed in SOI studies based on different methods (L_{int} <10 nm [18,55,56]).

In the following subsections, we will therefore summarise our main investigations of the capture efficiency of the Si-SiO_2 interface based on the TEM analysis of the defect evolution [17,62] (section 3.3.1) and of the Boron TED [63] (section 3.3.2), and show that only in the second case it was possible to reliably quantify the interface recombination length. These works were carried out within the PhD thesis of Mehdi Bazizi [64] and the post-doctoral activity of Pier Francesco Fazzini.

3.3.1. Defect evolution

The presence of the Buried Oxide (BOX) in a SOI wafer can alter the interstitial concentration in the Si top layer in two ways: by reducing the initial concentration of interstitials created by the implant or acting as a sink for interstitial recombination. The first effect is connected to the 'cutting-out' of the excess interstitial profile generated by the ion implant. The part of the profile falling into the BOX is to be considered as lost when comparing the total number of initial interstitials in Bulk Silicon and SOI. The second effect is due to the fact that an interstitial can be absorbed when it reaches the buried Si-SiO_2 interface. This effect adds up to the interstitial recombination at the native SiO_2-Si top layer interface located in proximity of the wafer surface. It can thus be expected that recombination of interstitials at interfaces during post-implant anneals is higher in SOI specimens compared to Bulk specimens implanted and annealed in the same conditions.

It is commonly accepted [18,19,65,66] that the density and size of EOR defects decrease when passing from Bulk Silicon to SOI but different arguments have been used in the literature to explain this reduction. The possible effect of the buried Si-SiO_2 interface acting as a sink, for example, has been indicated by some published experimental analysis [18], and ruled out by others [66]. However, even in experiments where the buried Si-SiO_2 interface was clearly indicated as the cause for the EOR defect reduction in SOI [18], the 'cutting-off' effect could not be ruled out, so that reliable quantitative data on the influence of the buried Si-SiO_2 interface on extended defect evolution were still missing when we started to work on this subject. For our investigations, the implant conditions were therefore always chosen in order to rule out this effect.

In a first experiment ("thick SOI" [17]), two SOI wafers (with an over-layer thickness of 44 nm and 55 nm, respectively) and a bulk Si reference wafer were implanted with 13 keV Ge^+ to a dose of $1x10^{15}$ cm^{-2}, inducing the formation of a 25 nm-thick surface amorphous layer. All wafers were annealed 700°C (300 s and 1000 s) or at 800°C (30 s and 300 s).

In a second set ("thin SOI" [62]), two thinner SOI wafers were chosen (18 nm and 34 nm, respectively) in order to verify if the EOR modification by the buried Si-SiO_2 interface was still measurable in such conditions. The wafers were implanted with 3 keV Ge^+ to two different doses ($5x10^{14}$ cm^{-2} or $2x10^{15}$ cm^{-2}), leading to the formation of a surface amorphous layer of 8 nm and 9 nm, respectively. All wafers were then annealed at 600 °C for 1 hour.

In both experiments, the implant energies were chosen in order to minimize the 'cutting-off' effect. An example is given in Figure 6, showing the excess interstitial distributions (calculated by SRIM [67]) both for the low-dose and the high-dose implants of the "thin SOI" experiment. Cutting the two profiles at 18 nm (corresponding to the thinnest specimen), less than 0.5% of the interstitials are lost in

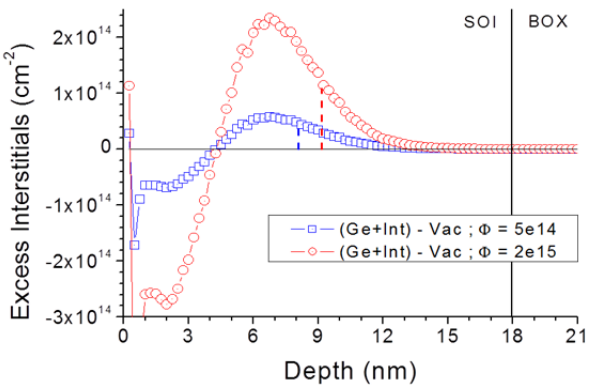

Figure 6 – SRIM Monte-Carlo simulation of excess interstitials profiles for two Ge^+ 3 keV implants having a dose of $5x10^{14}$ cm^{-2} and $2x10^{15}$ cm^{-2}. In both cases, interstitials lost in the box are less than 1% of the total number of generated interstitials for a 18 nm thick SOI (the thinnest SOI substrate used in this experiment).

the BOX allowing us to completely neglect the 'cutting-out' effect. Similarly, less than 1% of the initial interstitial distribution is lost in the buried oxide in the "thick SOI" experimental setup.

Two typical TEM images obtained on a bulk Si and on a 41 nm SOI specimen ("thick SOI" experiment) annealed at 800 ◦C for 300 s are reported in Figure 7, in which the reduction of defects density and size in SOI samples as compared to bulk Si is evident.

The detailed quantitative analysis (not shown) of all the annealed samples, in terms of defect nature, density and size, revealed that defect evolution in SOI has the same trend as in bulk Si. In particular, known facts about defects, such as the accelerated formation of dislocation loops compared to {311}s at high temperatures (cf. Chapter I), are well reproduced in SOI. In addition, all the obtained data were compatible with a non-conservative Ostwald ripening mechanism, since the total concentration of atoms trapped in the defects, N_b, was found to decrease over time. As discussed in Chapter I, this decrease is associated with the absorption of interstitials at the surfaces. We therefore concluded that the observed differences in terms of the absolute values of defect density and N_b were to be associated to a different contribution of the surfaces to the absorption of interstitials in the investigated wafers.

Figure 8 shows the total N_b (obtained by summing up the individual N_b measured for dislocation loops and {311}s) as a function of the substrate type for all the in vestigated thermal budgets. It can be clearly observed that the N_b measured in the

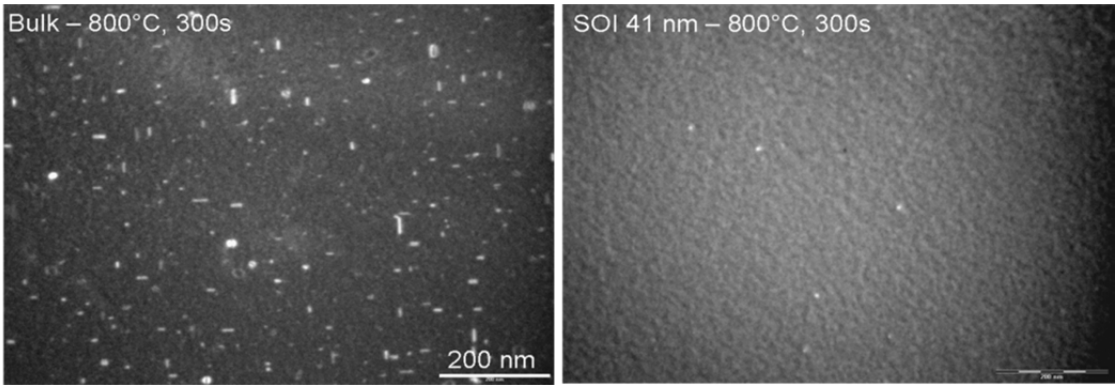

Figure 7 – Plan-view images obtained in WBDF conditions (**g**=[422]) after 13 keV Ge^+ implantation to a dose of $1x10^{15}$ cm^{-2} and annealing at 800°C for 300 s. (a) Bulk Si. (b) SOI (t_{SOI} = 41 nm).

SOI wafers is systematically lower than the one measured in the Bulk specimen. Moreover, it decreases when passing from the 55 nm SOI wafer to the 41 nm one. This is compatible with the fact that the absorption from the buried Si-SiO_2 interface increases when its distance from the EOR defects decreases, similarly to what was found for the top Si surface (cf. section 1.5.2). It can also be observed that N_b follows a different trend in the three wafers, which is again compatible with the buried interface acting as an additional sink for interstitials. As a result, the defect dissolution increases when a second interface is added (passing from bulk Si to SOI) or when it is put closer to the EOR defects (from 55 nm SOI to 41 nm SOI). This effect clearly demonstrates the advantage of SOI over bulk Si in terms of defect reduction.

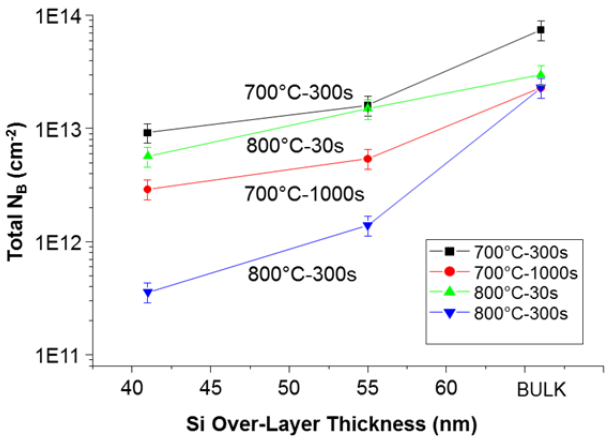

Figure 8 – Total concentration of atoms trapped in the defects, N_b, measured for different anneals as a function of the substrate type (the Bulk data are represented by the rightmost points in the plot). All wafers were implanted with 13 keV Ge^+ ions to a dose of $1x10^{15}$ cm^{-2}.

The investigation of defect evolution in thinner SOI wafers gave similar results, confirming the beneficial effect of the buried Si-SiO_2 interface in reducing the defect density, although the low annealing temperature used in this experiment (600°C) did not allow to achieve a complete quantitative analysis of the TEM data.

Typical WBDF TEM images from the reference bulk Si wafer and from the two SOI wafers are reported in Figure 9. The EOR defects are located at a distance of about 10 nm from the top surface. It is evident that the defect density decreases when passing from bulk Si to SOI and going from thick to thin SOI layers. Due to the small size of the observed defects, it was difficult in this case to estimate the defect average size with high accuracy. The comparison of the results from the different wafers was therefore limited to the defect density. The measured values are shown in Figure 10. Even if large errors were obtained in the estimates (mainly due to the small defect size), the trends are quite evident from the graph, showing that, for both implant

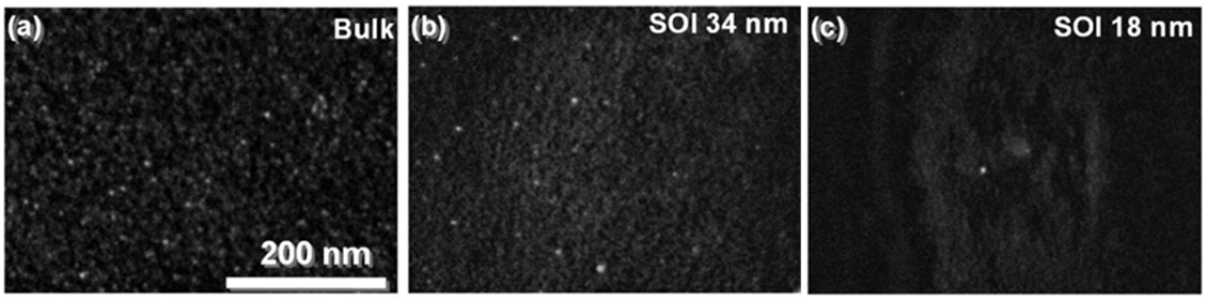

Figure 9 – Plan-view images obtained in WBDF conditions (**g**=[422]) after 3 keV Ge^+ implantation to a dose of $2x10^{15}$ cm^{-2} and annealing at 600°C for 1 h. (a) Bulk Si. (b) SOI (t_{Si} = 34 nm). (c) SOI (t_{Si} = 18 nm).

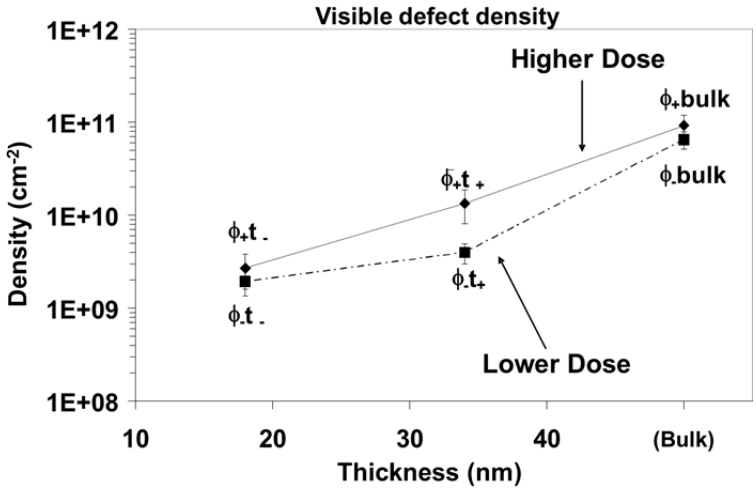

Figure 10 – Visible defect density measured from the TEM WBDF images as a function of the silicon over-layer thickness, after 3 keV Ge^+ implantation to a dose of $2x10^{15}$ cm^{-2} (Φ+) or $5x10^{14}$ cm^{-2} (Φ-) and annealing at 600°C for 1 h.

doses, there is a strong density reduction when passing from bulk Si to SOI after the anneal and that this decrease is more pronounced when the over-layer thickness is smaller, i.e. when the Si/BOX interface is closer to the EOR defects. Again, these observations are compatible with the assumption that the buried Si-SiO_2 interface plays the same role as the wafer surface, i.e. it acts as a sink for interstitials. However, in order to confirm this assumption, it was necessary to compare the data with a numerical model in which the effects of the buried Si-SiO_2 interface are taken into account.

For the simulations, we used the FRENDTECH model, already presented in Chapter I (cf section 1.5.3). To adapt this model to the case of SOI, the only expression to modify is the equation describing the supersaturation of free interstitials in dynamical equilibrium with the extended defects (eq. (5), section 1.2.2,). Assuming that the buried Si-SiO_2 interface also acts as a sink of interstitials but with a different recombination length (L_{int}) compared to the silicon surface (L_{surf}), the term describing the interstitial flux towards the surface, $\frac{1}{R_p+L_{surf}}$, is replaced by $\frac{1}{L_{eff}}$ with

$$\frac{1}{L_{eff}} = \frac{1}{R_p + L_{surf}} + \frac{1}{(t_{ox} - R_p) + L_{int}} \qquad (1)$$

where R_p is the depth at which the defects are located and t_{ox} is the SOI thickness. A schematic picture of the corresponding fluxes and interstitial concentration variation in SOI structures is presented in Figure 11. In the simulations, the recombination length associated to the Si surface, L_{surf}, was kept fixed to the value determined from previous fits of bulk Si experimental data (L_{surf} = 1 nm), while the Si/BOX interstitial

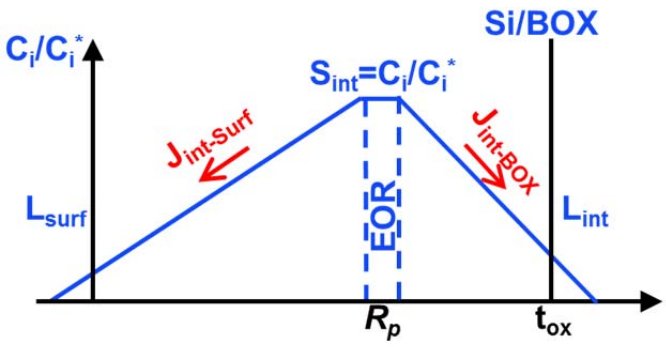

Figure 11 – Schematic illustration of the interstitial supersaturation variation and the associated interstitial fluxes in SOI in the approximated model used in the simulations.

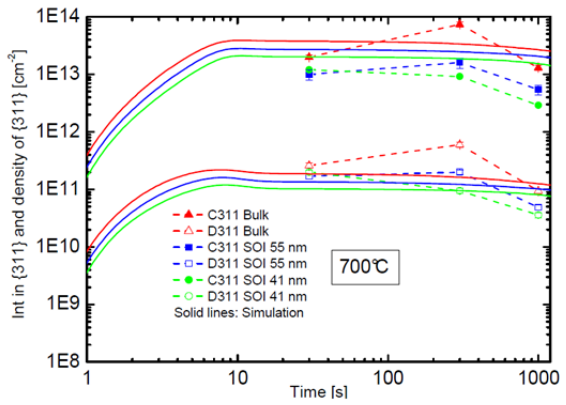

Figure 12 – Time evolution at 700°C of the density of interstitials trapped in {311} defects (C311) and {311} defect density (D311) for Silicon bulk, SOI 55 nm, and SOI 41 nm wafers implanted with 13 keV Ge^+ to a dose of $1x10^{15}$ cm^{-2}. The solid lines represent the FRENDTECH model simulations while the dotted lines represent experimental data. Si/BOX interface recombination length=1nm.

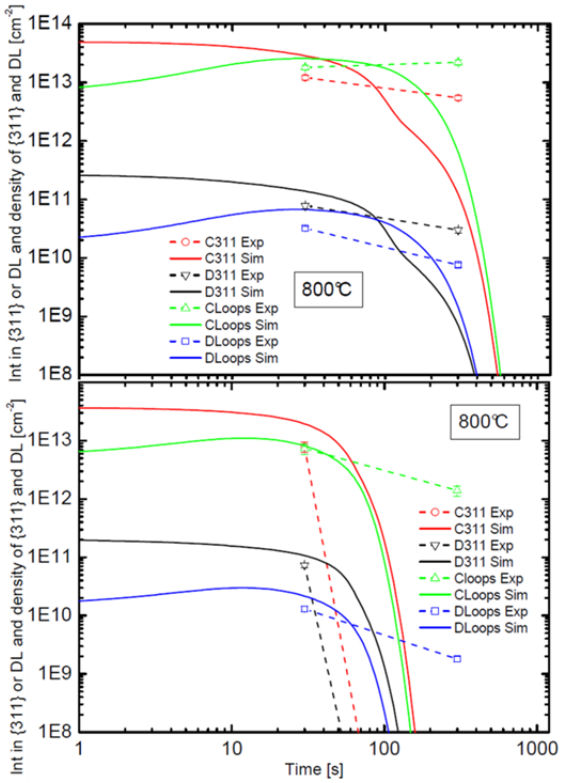

Figure 13 – Time evolution at 800°C of the density of interstitials trapped in {311} defects (C311) and in dislocation loops (D_{Loops}), {311} defect density (D311) and DL density (D_{Loops}) for Silicon bulk (*top*) and SOI 55 nm (*bottom*). Wafers were implanted with 13 keV Ge^+ to a dose of $1x10^{15}$ cm^{-2}. The solid lines represent the FRENDTECH model simulations while the dotted lines represent experimental data. Si/BOX interface recombination length=1nm..

recombination length, L_{int}, was allowed to vary between 1nm and 5 nm. Finally, concerning the distinction between the different defect types, we used a simple criterion based on the formation energy dependence on the defect size (cf. Figure 27 in Chapter I) and assumed that the simulated defects are {311}s when $30 < n < 350$ and dislocation loops when $n > 350$.

The model was applied to the data obtained from the "thick SOI" experiment, were the defect size was measured more accurately. Figure 12 reports simulated and measured data related to {311} defects (density, D_{311}, and number of atoms bound to them, C_{311}), after annealing at 700°C for the three investigated wafers. The results clearly indicate *(i)* that the model is able to well reproduce the {311} defects evolution behaviour in both bulk Si and SOI and *(ii)* that the hypothesis of considering the Si/BOX interface as an additional sink for interstitials is correct. However, it must be noted that the relatively large errors in the experimental values of the defects density and size made it impossible to carry out a more refined analysis of the impact of the L_{int} value on the simulation results. In addition, due to the "simplified" way in which the {311}-to-loops transformation is defined, this model could not be calibrated to perfectly match the {311}-to DL transformation. As a consequence, it systematically predicts an early formation of loops, which were not observed, for instance, after low temperature annealing, such as the one reported in Figure 12. A better agreement with {311} and DLs experimental data was achieved after annealing at 800°C in both bulk Si (Figure 13, top) and SOI 55 nm (Figure 13, bottom). In particular, the model succeeded in predicting the correct decrease in the interstitial and defect densities when passing from bulk Si to SOI. However, similarly to the 700°C anneal data, the experimental

errors associated with the TEM measurements as well as the model limitations mentioned above did not allow to achieve a precise quantification of the Si-SiO_2 interface recombination length. A different method, based on the investigation of Boron TED in SOI wafers, will be therefore presented in next section.

3.3.2. Dopant diffusion: the role of the buried Si/BOX interface

The experimental set up for this study consisted of one Si wafer (reference) and one SOI wafer with a Si top-layer thickness of 160 nm. A 1.5 µm-thick CVD Si layer was then grown on top of each wafer, which contained three boron marker layers with a peak Boron concentration of $2x10^{18}$ cm^{-3}, located at a depth of 0.2, 0.8 and 1.3 µm in the Si wafer and a depth of 0.1, 0.6 and 1.0 µm in the SOI wafer. Implantation damage was then introduced in both wafers by a non-amorphising Si^+ implant at 40 keV to a dose of $6x10^{13}$ cm^{-2}, followed by annealing at 740°C in flowing N_2 for times ranging from 1 sec to 2 hours. In such conditions, the implantation-induced defects (consisting of {311} defects) are located at a depth of about 100 nm. In the SOI wafer, it is therefore expected that the enhanced diffusion of the various boron marker layers during annealing will strongly depend on their relative position between the defects and the buried Si-SiO_2 interface, according to its efficiency in capturing the Si interstitial atoms diffusing out of the defect region.

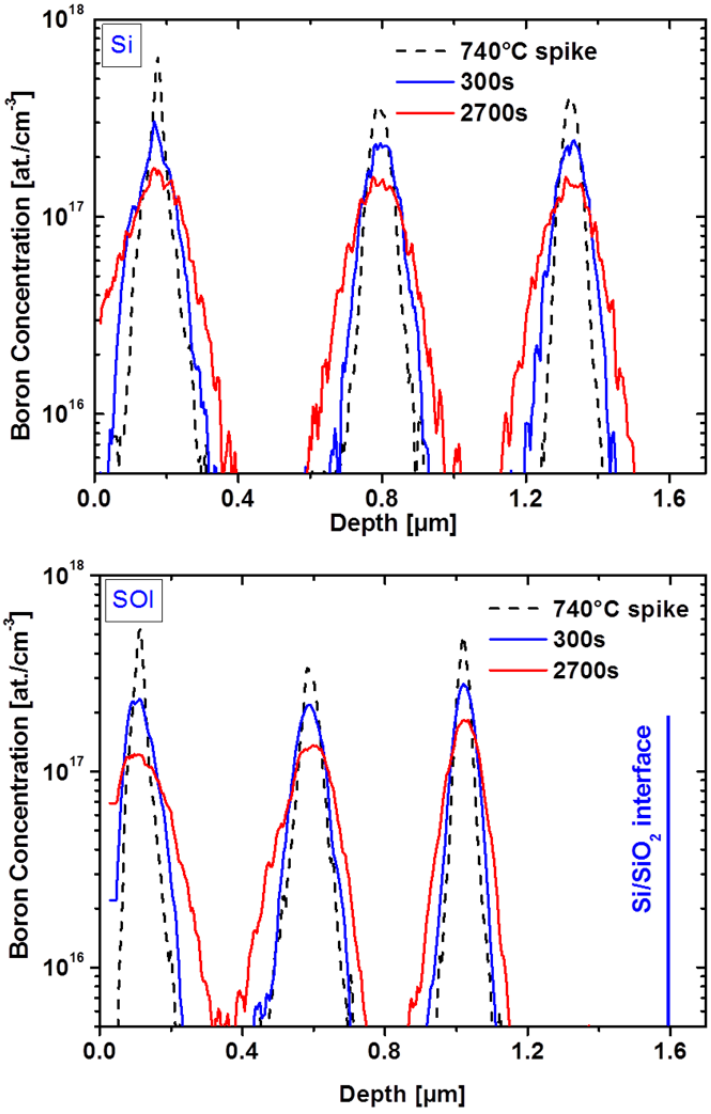

Figure 14 – Boron depth distribution profiles in (a) Si and (b) SOI structures measured by SIMS following a 40 keV Si^+ implant to a dose of $6x10^{13}$ cm^{-2} and annealing at 740 °C for various time intervals.

Selected B depth profiles measured by SIMS after annealing are shown in Figure 14. The top graph refers to the reference bulk Si, while the bottom one refers to the SOI wafer. A significant diffusive broadening is observed for all the boron marker layers after each time interval. This broadening largely exceeds what would be expected from an equilibrium diffusion process, confirming that implantation induced enhanced

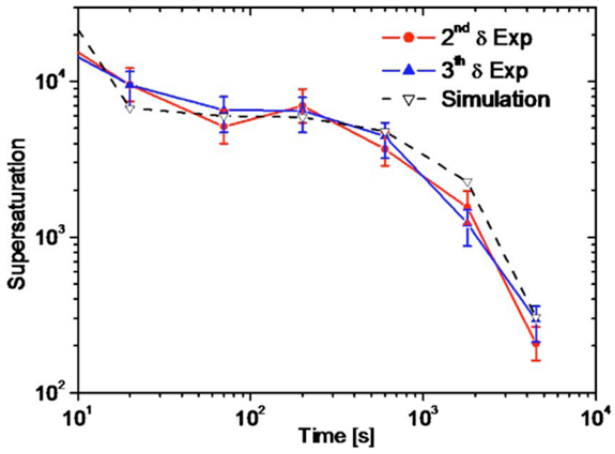

Figure 15 – Time evolution of the interstitial supersaturation in the Si reference structure following a 40 keV Si^+ implant to a dose of $6x10^{13}$ cm^{-2} and annealing at 740 °C. Filled symbols and solid lines: measured values from boron marker layers located at a depth of 780 and 1330 nm. Empty symbols and dashed line: simulated values (surface recombination length L_{surf}: 1 nm).

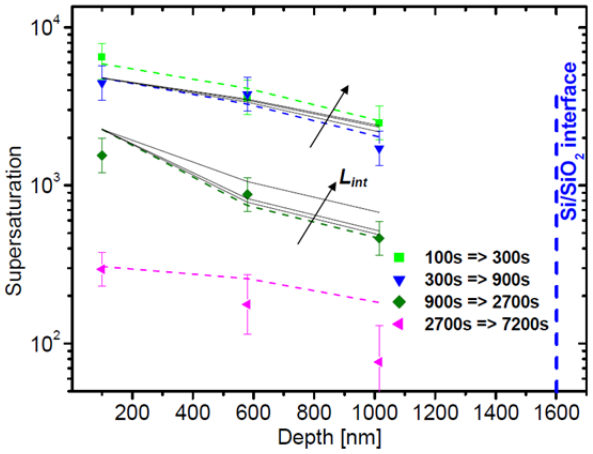

Figure 16 – Depth dependence of the average diffusion enhancement (interstitial supersaturation) of boron marker layers grown on a SOI substrate, over different time intervals during annealing at 740 °C. Damage implant: 40 keV Si^+, $6x10^{13}$ cm^{-2}. Symbols: measured values. Color dashed lines: simulated values (interface recombination length L_{int}: 1 nm). Black solid lines: simulated values with increasing values of L_{int} (5, 10, and 40 nm, see arrows).

diffusion occurred, in agreement with the presence of a defect layer in the implanted region (cf. Chp. I, section 1.1.1). In addition, it appears that the three boron marker layers in the Si wafer exhibit similar diffusion behavior independent of their depth position. In contrast, the broadening of the marker layers in the SOI wafer, while being systematically less pronounced than in the Si reference, continuously decreases when going from the shallowest to the deepest one.

These results are clearly consistent with an efficient interstitial trapping at the buried Si–SiO_2 interface, as shown in previous section in the case of defect evolution. In order to achieve a quantitative estimation of the interface trapping efficiency (i.e. its recombination length, L_{int}) it was therefore necessary, firstly, to correctly evaluate the TED levels associated to the measured profile broadenings and secondly, to simulate them using a defect-diffusion model in which the effects of the buried Si-SiO_2 interface are taken into account.

The TED levels obtained for the reference Si wafers using a fitting method [61] based on the interstitial kick-out mechanism of B diffusion [68] are shown in Figure 15 (filled symbols and solid lines). The almost constant value of supersaturation for annealing times up to 600 s corresponds to the Ostwald ripening of the {311} defects (as verified by TEM analysis on the same samples, not shown), while the final decrease is due to their dissolution. More importantly, both boron marker layers exhibit the same diffusion enhancement, independently of their depth. Considering the high diffusivity of silicon interstitials and the absence of bulk traps in this wafer, the measured interstitial supersaturation therefore reflects the one existing in the defect region. Figure 15 also reports the simulation results (empty symbols and dashed line) after annealing at 740 °C, obtained with the "moment-based" model available in the Synopsys TCAD SProcess simulator (cf. section Chp. I, section 1.5.3). Due to the

simple defect configuration in this experiment ({311} defects only), this model provides results as reliable as the "full" FRENDTECH model used in previous section, but with a much reduced simulation time. In the simulations, the surface recombination length, L_{surf}, was taken equal to 1 nm. As shown in Figure 15, after calibration, the time dependence of the interstitial supersaturation is perfectly reproduced.

The experimental results of boron TED in the SOI wafer are reported in Figure 16 (symbols). In this figure, the interstitial supersaturation is plotted as a function of the depth of the analyzed marker layers and the various curves correspond to the different time intervals investigated. The results clearly indicate that over the entire annealing time range, the interstitial supersaturation continuously decreases when approaching the buried Si–SiO_2 interface, confirming that excess interstitials diffusing out of the defect region recombine at the buried Si–SiO_2 interface, in agreement with the qualitative conclusions directly drawn from the SIMS profile.

In order to model the effect of the buried Si-SiO_2 interface on the Boron enhanced diffusion, we used the same assumption as in the investigation of the defect evolution in SOI (cf. previous section), i.e. we assumed that the buried Si-SiO_2 interface also acts as a sink of interstitials but with a different recombination length (L_{int}) compared to the silicon surface (L_{surf}), (see Figure 11). L_{int} was initially set at a value of 1 nm (same trapping efficiency as the silicon surface), while keeping all other simulation parameters fixed to the values obtained from the reference Si wafer. The simulation results are shown in Figure 16 (coloured dashed lines). With the exception of the longest annealing times, when the defects enter the dissolution stage (pink triangles in Figure 16), the excellent agreement between simulations and experiments clearly confirms that the observed phenomenon in SOI wafers can be modeled in terms of an additional capture of interstitials at the buried Si–SiO_2 interface. The discrepancy between simulation and experiments for the 2700–7200 s time interval is probably due to the increased difficulty in extracting a reliable interstitial supersaturation value in the late stages of TED, when the small observed profile broadening becomes comparable to the noise of the SIMS signal.

Finally, simulations have been repeated using different values of L_{int} in order to assess the ability of this approach to provide a reliable estimation of the recombination efficiency. Results are reported in Figure 16 for the time intervals 300–900s and 900–2700s (solid black lines) for increasing L_{int} values of 5, 10, and 40 nm, respectively, that correspond to progressively weaker recombination mechanisms. As expected, the simulated interstitial supersaturation in the defect region (located more than 1 μm away from the Si–SiO_2 interface) is insensitive to these variations in L_{int}. In contrast, in the vicinity of the interface, the supersaturation increases when increasing L_{int}. In particular, it is found that starting from a value of 10 nm, at least one of the experimental points is not correctly simulated, which provides an upper limit for the interface recombination length value.

3.4. Germanium-based materials

3.4.1. Defect formation in strained and relaxed SiGe alloys

As seen in section 3.1.2, the optimization of the source/drain junction performances in MOS devices containing SiGe layers relies on the capability to accurately model implantation and diffusion phenomena in such layers, which are strongly related to the evolution of implantation-induced extended defects. The effects of Germanium composition on the evolution of extended defects in Si-Ge layers was reported in literature by several publications [69,70,71]. Fedina et al. [71] showed that differently from silicon, the formation of dislocation loops in electron irradiated strained SiGe layers was favoured in comparison with planar {311} defects, due to the presence of strain in the SiGe layer. A similar effect was also reported in the case of extended defects formed by ion implantation in unstrained SiGe layer [70], where it was shown that the concentration of Ge in the alloy not only affects the {311}/Dislocation Loops density ratio but also the ripening of these two kinds of defects. These studies pointed out some interesting features concerning the evolution of implantation defects in SiGe but the reported data were too limited to provide a full description of the investigated phenomena and to improve physical models for their prediction.

On the one hand, it was necessary to disentangle the two main mechanisms contributing to the modification of defect evolution in SiGe epitaxial layers, namely the "chemical" contribution due to the presence of Ge and the contribution due to the presence of strain. On the other hand, it was necessary, to study defect evolution at several different temperatures since the Ostwald ripening mechanism associated to defect evolution is thermally activated.

In the following of this sub-section, we will therefore summarise the results of the investigations we carried out on this subject, including the PhD thesis of Mehdi Bazizi [64] and the post-doctoral activity of Pier Francesco Fazzini [72].

Experimental study

For this activity, we therefore conceived some dedicated test structures that allowed us to observe compositional and strain effects separately, while keeping a common reference for the damage formation process. They are schematically illustrated in Figure 17. For the compositional effect study, three wafers containing relaxed SiGe alloy layers with various Ge contents (20, 35 and 50 at. %, cf. Figure 17b) were grown by CVD on graded SiGe virtual substrates. For the study of strain effects, two more structures were fabricated. In the first (cf. Figure 17c), a tensely strained Si layer was grown on relaxed SiGe layer, followed by the deposition of a SiGe capping layer with the same composition. In the second (cf. Figure 17d), a compressively strained SiGe layer was directly grown on top of a Si substrate,

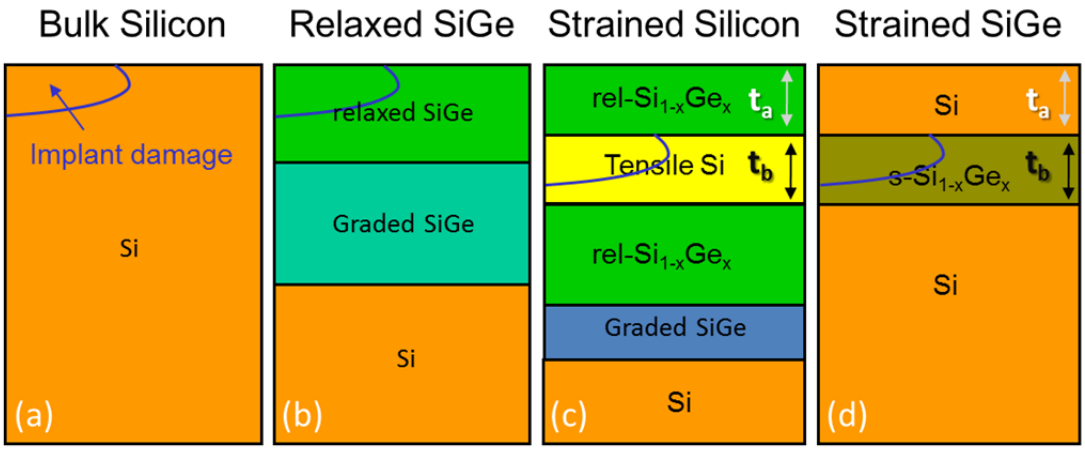

Figure 17 – Schematic illustration of the multi-layered structures used in our experiments to study extended defects evolution in strained and unstrained Silicon-Germanium layers.

followed by a 50 nm Si capping layer. For the strain effect study, only the 20 and 35 % Ge compositions were considered. Two different implant conditions for the damage introduction were identified by numeric simulations [67,73] to ensure that the excess interstitial distributions were entirely contained in the targeted layer and that the interstitial supersaturation was high enough for extended defects to nucleate during annealing: a non-amorphising implant (40 keV Si^+, $6x10^{13}$ cm^{-2}) and an amorphising one (35 keV Ge^+, $1x10^{15}$ cm^{-2}).

An example of the compositional effect on defect evolution is shown in Figure 18. The images refer to a non-amorphising Si^+ implant followed by annealing at 740°C for 900 s and clearly show some evident differences in defects distribution among the various samples. In the reference Si sample (Figure 18a) the majority of defects are rod-like {311}s with few circular faulted dislocation loops (FDLs). In the 20% relaxed SiGe structure (Figure 18b), the two defect types are still visible but {311}s size and density has decreased. This effect is more pronounced in the 35% case in which the FDL density continues to increase while the {311} density decreases. Finally, only FDLs are present in the sample containing 50% Ge.

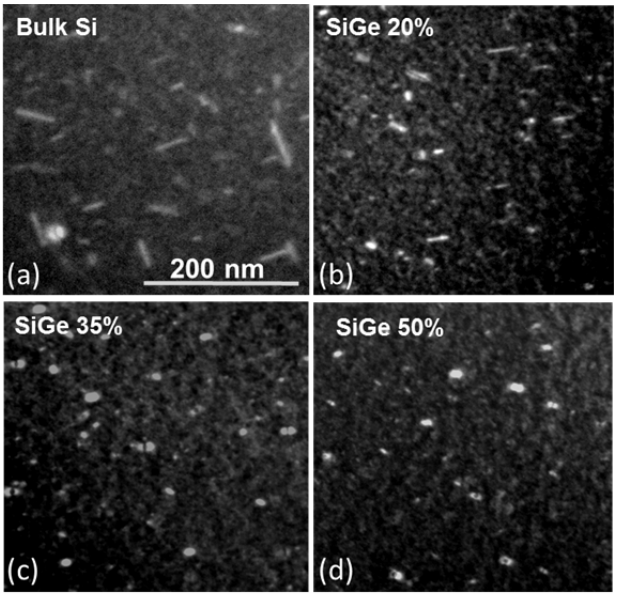

Figure 18 – Plan View WBDF images (g=[422], s<0) of the Si and relaxed $Si_{1-x}Ge_x$ structures after a non-amorphising Si^+ implant and annealing at 740°C for 900 s. {311} defects and Faulted Dislocation Loops are visible in this image as high contrasted white zones on a dark background.

The favoured formation of DLs when the Ge content in the SiGe alloys is increased was confirmed by the investigation of the samples submitted to an amorphising Ge^+ implant. As shown in Figure 19a, also in this case loops are preferentially formed in the

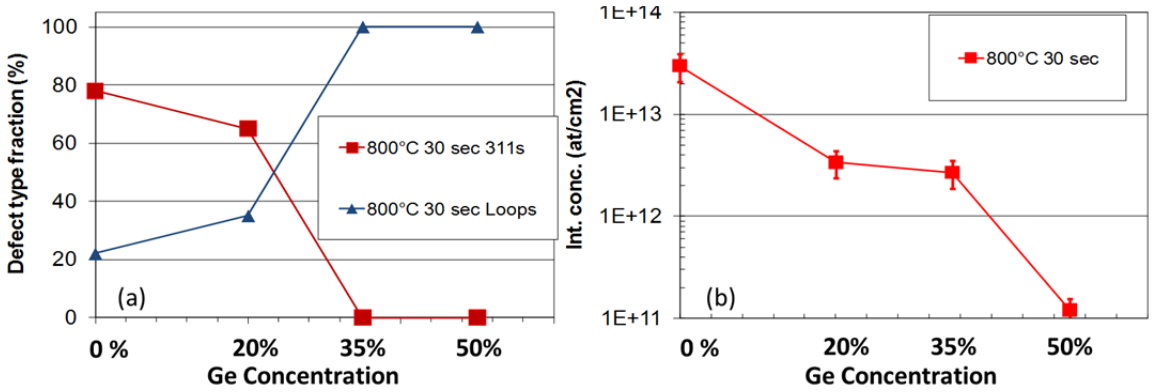

Figure 19 – (a) Defect type fractions ({311} s vs DLs) and (b) overall density of interstitials contained in all defect families as a function of Ge content in relaxed SiGe structures after implantation with 35 keV Ge^+ 1×10^{15} cm^{-2} and annealing at 800°C for 30 s.

35% and 50% SiGe structures, where they represent the totality of the formed defects. An additional effect associated to the presence of Ge is the decrease of the total number of interstitial atoms contained in the defects, as shown in Figure 19b. In particular, this result applies to dislocation loops, which are the only defect type observed in the 35% and 50% structures. As for {311} defects, this behaviour was verified and confirmed separately (not shown) by selecting "low" thermal budget annealing conditions (680°C for 300 s or 900 s) so that {311} defects only were formed.

In summary, the increase of Ge concentration in relaxed SiGe structures leads to *(i)* an overall decrease of the defect stability (i.e. a decrease in the total density of interstitials contained in the defects) and to (ii) an enhanced {311}-to-loops transformation.

For the investigation of the strain effect on the formation of extended defects, the structures fabricated with 35 % Ge content could not be used, as they contained several hairpin dislocations originating from the EOR defects, probably related to the initial stages of a relaxation process [74]. The analysis was therefore carried out uniquely on the 20 % Ge-based structures. Figure 20 shows a visual summary of the evolution of extended defects in the strained Si and SiGe structures after an amorphising Ge^+ implant and anneal at 740°C for 900 s. We found that, compared to the reference Si sample (Figure 20a), the {311} defects exhibit a smaller size and a slightly higher density in the

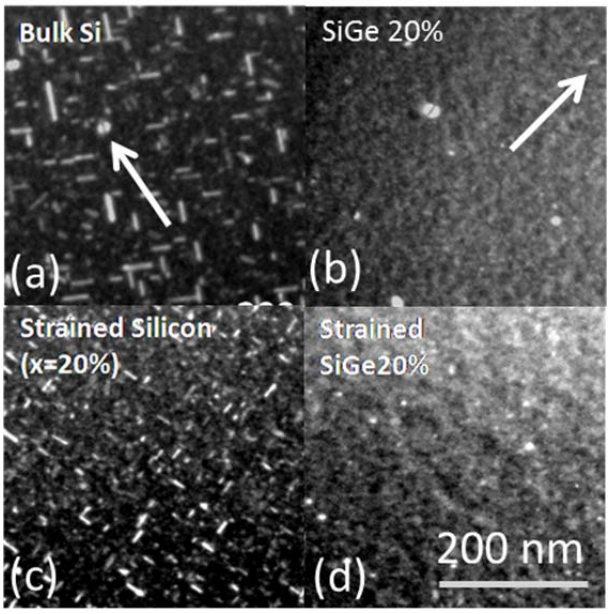

Figure 20 – Plan-view WBDF images of various samples showing the nature and density of EOR defects in relaxed and strained structures with different Ge content after implantation with 35 keV Ge^+ $1x10^{15}cm^{-2}$ and annealing at 740°C for 900 s. (a) Bulk Si. (b) Relaxed $Si_{0.2}Ge_{0.2}$. (c) Strained silcon (tensile). (d) Strained $Si_{0.2}Ge_{0.2}$ (compressive).

strained Si sample (Figure 20c). In addition, while {311}s represent the totality of the defect population in the strained sample, a small fraction of loops is present in the reference unstrained one (cf. arrow in Figure 20a). These results suggest that the Ostwald ripening of {311}s is somehow weakly "retarded" by tensile strain, which is also responsible for a less effective {311}-to-loops transformation. The opposite behaviour is observed in the case of compressive strain introduced in SiGe layers: while some {311}s are still present in the reference relaxed SiGe structure (cf. arrow in Figure 20b), the compressively strained SiGe sample only contains loops. As in the previous case, the overall defect stability is not strongly altered, with the total density of interstitials contained in the defects being comparable in the two structures. This behaviour was confirmed by the quantitative analysis of all data obtained under different annealing conditions (740°C 300 s and 900 s, 800°C 30 s and 300 s).

The strain effects on the defect formation can therefore be summarised as follows: *(i)* tensile strain (in Si) retards the transformation of {311} defects into loops; *(ii)* compressive strain (in SiGe) enhances the transformation of {311}s into loops; *(iii)* in all cases, the overall defect stability is not strongly modified in the presence of strain.

Several physical mechanisms contribute to the formation and evolution of implantation-induced extended defects and each one of them might be modified by adding germanium (and/or introducing strain) to silicon.

One of these is the diffusion of the free interstitials that compose the defects. Indeed, several studies [75,76,77] indicate that both Ge and Si self-diffusivities in relaxed SiGe strongly increase with Ge content. This leads to an enhanced interstitial recombination at the surface during defect evolution and to an accelerated defect growth. In the case of {311} defects, this also implies that the critical size for transformation into loops is reached more quickly in SiGe alloys than in Si. These modifications are in agreement with two of the observed effects in relaxed SiGe structures: *(i)* an overall decrease of the defect stability (i.e. a decrease in the total density of interstitials contained in the defects) and *(ii)* an enhanced {311}-to-loops transformation. However, they cannot explain the observed decrease in defect size (cf. Figure 18).

Other mechanisms must therefore be considered to achieve a deeper understanding of the observed defect evolution and extend to applicability of Si defect models to SiGe-based materials. For instance, considering implantation damage, the substrate atomic mass increases when Ge is added to silicon, leading to a decrease of interstitial generation during implant. This is in agreement with the observed decrease in the number of atoms stored in the defects (cf. Figure 19b). In addition, it is well known that the Si-Ge bond energy is weaker than the Si-Si one [78,79,80,81], which can have several consequences on both point defects (modification of the equilibrium concentration of interstitials and vacancies) and extended defects: *(i)* decrease in the interstitial binding energy (leading to an increase

of the emission rate of both {311}s and DLs) and *(ii)* lowering of the energy barrier for the transformation of {311}s defects into loops (cf. section 1.4.1).

On the other hand, concerning the effect of strain, theoretical studies [82] indicate that biaxial tensile (compressive) strain in Si induces an increase (decrease) of the interstitial diffusivity. This is apparently in contrast with the observed effects in tensely strained Si, where the "slower" defect ripening with respect to unstrained Si (higher {311}s density and smaller size, cf. Figure 20) is rather in agreement with a lower interstitial diffusivity. A more complex scenario is therefore required to fully explain these results, possibly including the strain effects on both interstitial equilibrium concentration and defect formation energy.

Modelling

The modelling activity related to defect formation in SiGe-based materials was carried out within the EU project ATOMICS, in direct collaboration with the TCAD software producer Synopsys, with the main objective of minimising the required modifications of the existing silicon defect models, while ensuring their compatibility with all other integrated process models as well as a sufficiently short CPU time. For these reasons, the chosen simulation platform used in this activity was the "moment"-based model, already mentioned in Chp 1 (cf. section 1.5.3) [83,84], in which the number of differential equations necessary to fully describe the evolution of defects size-distributions during annealing is drastically reduced with respect to the original "FRENDTECH defect model" (cf. section 1.5.3).

The "moment"-based model only uses 3 equations for the evolution of small interstitial clusters (containing either 2, 3 or 4 interstitial atoms), while the evolution of {311} defects and Dislocation loops is driven by the four equations reported below (two per each defect family), describing two moments of their respective size-distributions, namely the defect density (D_{311} and D_{Loop}) and the total number of atoms contained in the defects (C_{311} and C_{Loop}):

$$\frac{dD_{311}}{dt} = k_f C_I \cdot C_{I4} - k_b \frac{D_{311}}{C_{311}} \cdot D_{311} - k_{311->DL} k_{D311} D_{311} \tag{2}$$

$$\frac{dC_{311}}{dt} = 5k_f C_I \cdot C_{I4} + k_a C_I \cdot D_{311} - k_b D_{311} - k_{311->DL} C_{311} \tag{3}$$

$$\frac{dD_{Loop}}{dt} = k_{311->DL} k_{D311} D_{311} + k_{CDL} \cdot 2\pi^2 \cdot R_{DL} \cdot D_I \cdot (-C^*_{I,DL}) \cdot \frac{D_{Loop}}{C_{Loop}} \cdot D_{Loop} \tag{4}$$

$$\frac{dC_{Loop}}{dt} = k_{311->DL} C_{311} + k_{CDL} \cdot 2\pi^2 \cdot R_{DL} \cdot D_I \cdot (C_I - C^*_{I,DL}) \cdot D_{Loop} \tag{5}$$

Although a full description of this model is beyond the scope of this document (details can be found in ref. 84), it is important to note here that the main physical

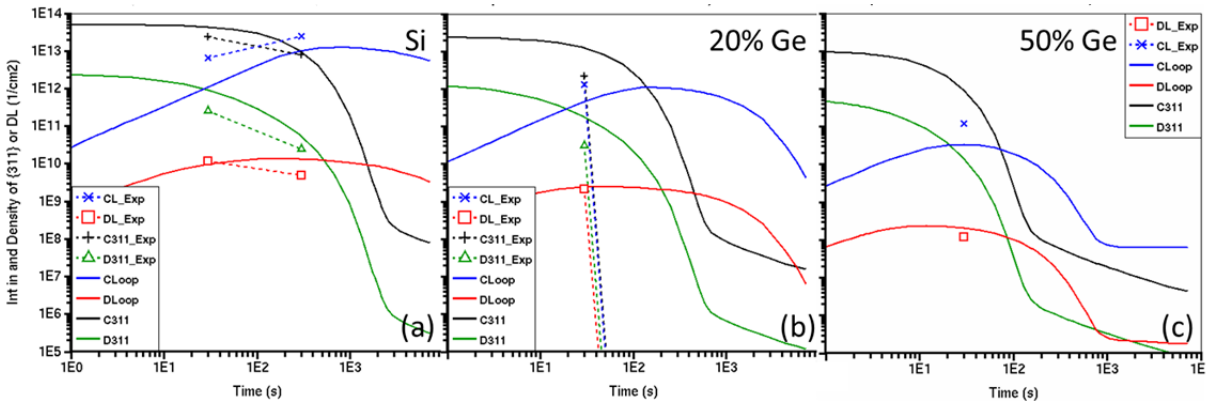

Figure 21 – Time evolution of extended defects density (D_{311} and D_{Loop}) and interstitial concentration trapped by the defects (C_{311} and C_{Loop}) in (a) bulk Si, (b) 20% SiGe and (c) 50% SiGe after implantation with 35 keV Ge^+ 1×10^{15} cm^{-2} and annealing at 800°C. Comparison of experimental data (symbols) and simulated curves (solid lines).

concepts describing defect evolution are equivalent to those considered in the "FRENDTECH defect model". In particular, information on the formation energy of {311} defects is contained in the k_b term of equations (2) and (3), describing the {311}s emission rate#, whereas for dislocation loops (eqs. (4) and (5)) the concerned parameter is $C^*_{I,DL}$##. Finally, the energy barriers related to the transformation of small interstitial clusters into {311} defects and from {311}s to dislocation loops are represented by the terms k_f and $k_{311\rightarrow DL}$, respectively.

In order to keep the number of model free parameters as low as possible, the effect of composition and strain on the evolution of {311} defects and dislocation loops was modeled considering that only three of the above mentioned parameters are dependent on the Ge content and strain level, namely k_f, k_b and $k_{311\rightarrow DL}$. An additional calibration parameter was *i-factor*, used in the simulation of the implant step, to calculate the number of silicon interstitials at the beginning of the annealing. Finally, in addition to the TEM results on defect evolution reported above, the simulations were also compared to the measured supersaturation of free silicon interstitials, obtained in similar relaxed SiGe structures by measuring the enhanced diffusion of Boron marker layers contained below that extended defects band.

An example of simulation results for the Ge compositional effect on defect formation in relaxed SiGe layers is reported in Figure 21, for an annealing temperature of 800°C###. Starting from a reference calibrated simulation in Bulk Si (Figure 21a), showing a good agreement between measured and simulated {311} and loops evolution, the model correctly predicts the decrease in density of both {311}s and DLs

---

Referring to eqs. (7) and (9) of Chp. 1, it results that $k_b \equiv R_n = D_i C_i^* \frac{A_n}{R_{eff}} exp\left(\frac{E_f(n)}{kT}\right)$, the difference being that, in the "moment"-based model, k_b is independent on size.

Referring to eqs. (7) and (9) of Chp. 1, it results that $C^*_{I,DL} = C_i^* exp\left(\frac{E_f(n)}{kT}\right)$. Unlike the {311} case, $C^*_{I,DL}$ is size-dependent through the loop radius, R_{DL}, contained in its definition [84].

The full set of simulation results for both the compositional and the strain effect on defect evolution is reported in the PhD thesis of Mehdi Bazizi [64].

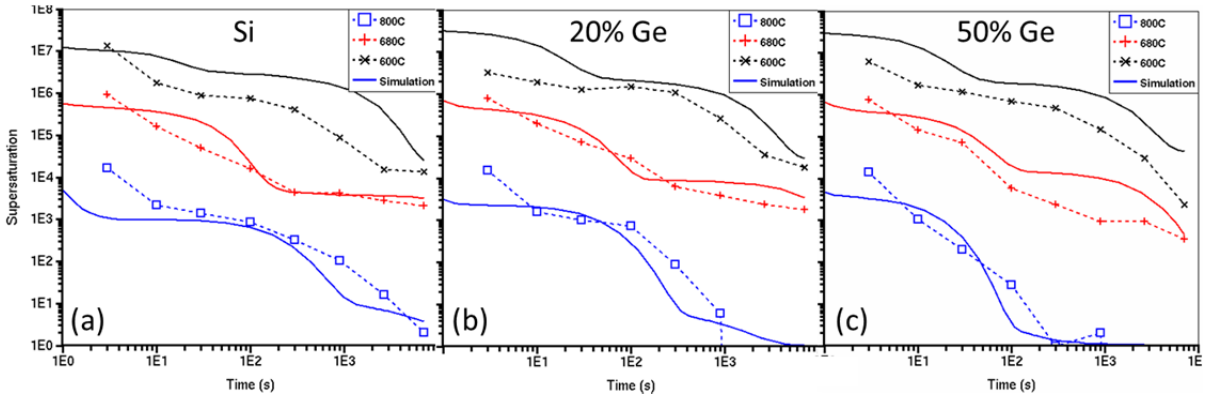

Figure 22 – Time evolution of interstitial point defects supersaturation in (a) bulk Si, (b) 20% SiGe and (c) 50% SiGe after implantation with 35 keV Ge^+ 1×10^{15} cm^{-2} and annealing at different temperatures. Comparison of experimental data (symbols) and simulated curves (solid lines).

in the 20% Ge sample after 30 sec (Figure 21b), as well as the earlier onset of {311}s dissolution, however a residual presence of dislocation loops is still predicted

after 300 s (whereas no defects were observed in TEM). Similarly, in SiGe layers with a 50% germanium content, the agreement between experiments and simulations is clear concerning the further decrease in the number of atoms stored in the loops after 30 s anneal, however the predicted {311}s and DLs dissolutions do not occur as rapidly as experimentally observed. A better overall agreement between experimental and calculated values is obtained for the interstitial supersaturation extracted from TED measurements (cf. Figure 22), which is more sensitive to the relative amount of the various defect families (ICs, {311}s and loops) rather than to the exact density value of each one of them.

The reported defect and TED simulations were obtained by modifying only three model parameters, namely by multiplying them by a corrective factor, α, as reported in Figure 23. In accordance with the physical analysis of the experimental results reported above, the lower stability of {311} defects and dislocation loops with increasing Germanium content in the SiGe layers was modelled by a slightly higher emission of interstitials from {311} defects (featured by the k_b parameter, cf. Figure 23a) and a higher transformation rate of {311}s into dislocation loops (featured by the $k_{311\rightarrow DL}$ parameter, cf. Figure 23b). In addition, the *i-factor* parameter was also calibrated in order to decrease the initial number of interstitials, in agreement with

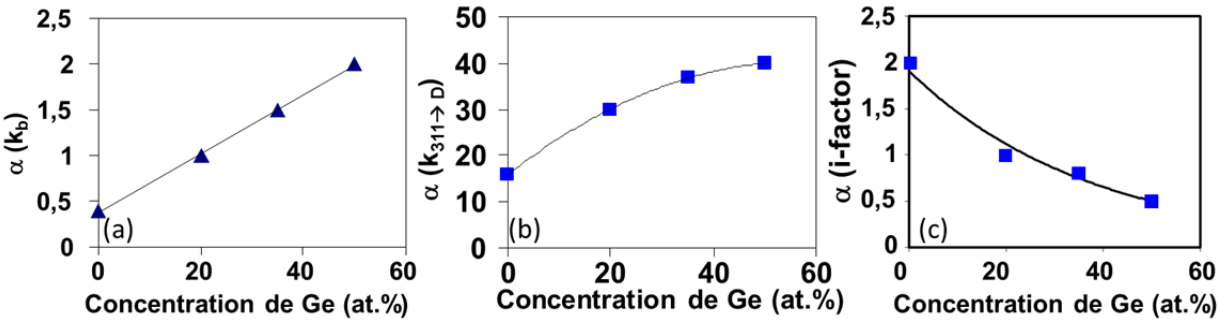

Figure 23 – Ge-content dependence of the correction multiplying factor applied to the default parameters of the "moment-based" defect model: (a) {311}s emission rate, (b) {311}→DLs transformation rate and (c) i-factor.

the increased atomic mass of SiGe layers with respect to Si (cf. Figure 23c). Finally, a regression of the calibration parameters obtained from the investigation of the compositional effect presented here and of strain effect (not shown), was done for a better implementation in the commercial version of Synopsys Sentaurus Process, where this set of parameters is still the reference for the simulations of extended defects in SiGe layers. Indeed, these models were further validated by the successful simulation of the electrical performances of 45-nm PMOS and NMOS containing a strained Si channel (on SiGe substrates) [85].

3.4.2. Ultra-shallow junction fabrication in pure Germanium

As discussed at the beginning of this chapter, germanium is the most promising "high-mobility" channel material expected to replace silicon in the near future. Indeed, compared to silicon, germanium exhibits a four times higher hole mobility [86] and requires lower process temperatures [87], reducing the problems related to the diffusion/activation of dopants in ultra-shallow junctions (USJ) and making germanium significantly better suited for integration with high-k dielectrics and metal gates [27,88].

At the time when we started working on this material (late 2008), a strongly debated question concerned the role of Ge interstitials during ultra-shallow junction fabrication by ion implantation. Due to the large vacancy concentrations existing under equilibrium conditions in Ge at usual process temperatures [89,90] and the observation that the equilibrium diffusion of self-interstitials (as well as that of several impurities) occurs by a vacancy mechanism [91,92], a doubt was raised on the possibility to form EOR defects after an amorphising implant in Ge. Indeed, early experiments performed using transmission electron microscopy did not reveal the presence of defects after SPER of amorphous Ge [93,94,95], while the first evidences of EOR defects formation (observed in cross section TEM images) came from two later works [96,97], with the latter published in 2009. However, in the work of Hickey *et al.* [96], EOR defects were observed together with several other defects caused by the incomplete amorphisation achieved at high ion implantation energy (1 MeV).

In addition, concerning p-type USJ fabrication, the occurrence of Boron enhanced diffusion was also the object of a strong debate[#] and no evidence at all existed concerning defects-related dopant electrical deactivation.

We will therefore summarise in the following of this sub-section the experimental work we carried out on this subject, including the Master research project of Federico Panciera and the post-doctoral activity of Pier Francesco Fazzini [98].

[#] The first direct experimental proof of Boron TED was provided in 2010 [E. Napolitani *et al.*, Appl. Phys. Lett. 96 (2010) 201906].

For this work, we fabricated p-type USJs by implanting 10 keV B^+ to a dose of $1x10^{15}$ cm^{-2} into germanium substrates preamorphised by a 100 keV Ge^+ implant to a dose of $1x10^{15}$ cm^{-2}. Dopant activation was investigated at different temperatures (between 400°C and 900°C). Cross-section TEM images from samples annealed at 400°C revealed the presence of a defect band located at a depth compatible with the expected position of the a/c interface (~100 nm), as shown in Figure 24a relative to a 100 s anneal time. The variation of the apparent defect density (~$1x10^{11}$ cm^{-2}, measured in plan-view using different diffracting vectors) indicated that they consisted of small dislocation loops (with an average diameter of less than 5 nm). At 400 °C, the defects did not exhibit any change in size up to 900 s anneal, then they rapidly dissolved after longer times (cf. Figure 24b and Figure 24c taken after 100 s and 7200 s, respectively).

In the 400°C-500°C range, SIMS profiles did not show any Boron diffusion, while at 900°C diffusion became observable only for B concentrations below 2×10^{18} cm^{-3}, in agreement with the maximum B solubility in Ge at high temperature [99]. In contrast, the Boron activation level exhibited a clear evolution between 400°C and 500°C, as shown in Figure 25, where the Hall effect measurements (Hall dose, N_H, and sheet resistance, R_S, are reported as a function of the annealing time. Starting from the lowest investigated thermal budget (400°C 100 s), where the Hall dose corresponds to the total activation of the implanted Boron profile, N_H was found to steadily decrease when increasing the annealing time, while no diffusion was detected (as well as no significant variation of carrier mobility), indicating that B deactivation occurred in this time interval. On the other hand, during isothermal anneals at 450°C and 500 °C, N_H increased, suggesting that boron atoms are reactivated in such conditions until N_H reaches the initial "full" activation value after 2700 s at 500 °C.

Considering that B deactivation occurs within the same time interval necessary to achieve complete defects dissolution, while the total deactivated boron dose is of the same order (~1×10^{14} cm^{-2}) as the density of interstitials initially trapped in the EOR defects, we concluded that, similarly to Si, the observed deactivation/reactivation phenomenon is due to the formation of electrically inactive boron-interstitial-clusters (BICs), caused by the migration of interstitials released from the dissolving EOR defects towards the doped region. However, the whole

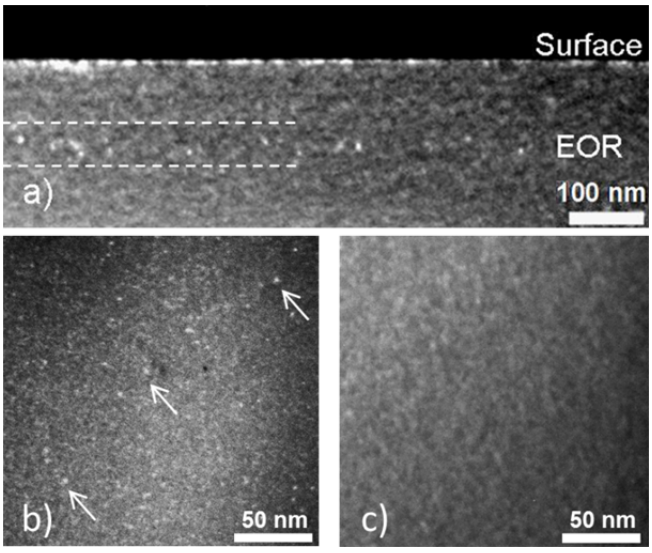

Figure 24 – WBDF-TEM images of a Ge sample amorphised by 100 keV Ge^+ $1x10^{15}$ cm^{-2} and subsequently annealed at 400 °C for different times. (a)-(b): 100 s. (c): 2 h. Images are taken in cross-section, (a), using g=422, or in plan-view, (b) and (c), under g=400.

deactivation/reactivation cycle surprisingly takes place while the maximum active B concentration largely exceeds (by some decades) its solubility limit, i.e. while the system is still in a metastable state, whereas, in silicon, Boron deactivation is accompanied by a progressive decrease of the maximum active concentration down to the expected solid solubility value. This difference between the two materials was confirmed by the high-thermal budget investigations. In the case, showing that only after 3h annealing at 900°C, the system reached thermal equilibrium, with a much lower value of the active dose (~2×10^{13} cm^{-2}), corresponding to an active concentration close to the boron solubility limit at this temperature (2×10^{18} cm^{-3} [99]).

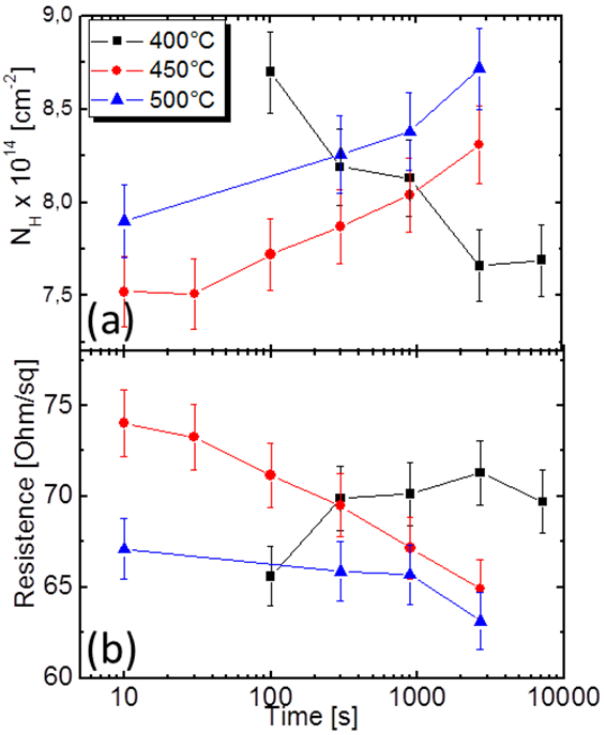

Figure 25 – (a Hall dose (N_H) of B implanted (10 keV $1x10^{15}$ cm^{-2}) in preamorphised Ge after thermal annealing at 400, 450, and 500 °C. (b) Sheet resistance (R_S) for the same samples.

On the basis of these results, we therefore proposed that Boron deactivation in Ge occurs through two separate phases: a first one of "transient" deactivation promoted by the excess of self-interstitial and characterized by unstable BICs formation; and a second one of precipitation during which boron definitively reaches its solubility limit. In Si, the cycle of deactivation/reactivation is superposed to precipitation, so when reactivation starts the system is already at equilibrium. On the contrary, in Ge these two phases occur at different times, because the thermal budget needed for the system to reach thermodynamic equilibrium, i.e. precipitation (several hours at temperatures as high as 900°C), is much higher than the one required for the whole deactivation/reactivation cycle to be completed, i.e. defect and BIC dissolution (~15min at 500°C). Finally, this peculiarity of Boron deactivation in Germanium is very interesting from a technological point of view, as it implies that, in Germanium, it is possible to achieve highly-activated defect-free p^+-n junctions using the pre-amorphisation technique.

3.5. Conclusions

The progressive introduction of advanced processes and materials in the semiconductor industry raised some specific questions related to the fabrication of USJs, including the formation of implant-induced defects during ultra-fast annealing, their evolution in the presence of the buried Si-SiO_2 interface in SOI materials or the

Boron activation stability in Germanium. We addressed these issues in a series of experiments started in 2005, mainly within the EU research projects ATOMICS and PullNANO. The main conclusions of our investigations in this domain are summarised below:

- During the ultra-fast temperature ramp-up and ramp-down occurring in a **millisecond Flash anneal**, the basic mechanisms that control the growth and evolution of extended defects are not modified with respect to the relatively slower annealing processes and defect models previously established for conventional anneals can be extended to the millisecond regime. In addition, the combination of impurity co-implantation and pre-amorphisation with millisecond Flash anneals provides a viable processe to achieve Ultra-Shallow Junctions compatible with the 32nm technology node, targeted at the beginning of this study (x_j<15 nm, R_S < 700 Ω/sq.).
- We used two different methods to study the behaviour of the buried Si-SiO_2 interface in **SOI materials** with respect to the implant-generated interstitial excess, the first based on the TEM analysis of the formation and evolution of implantation induced extended defects in SOI, the second based on the diffusion of CVD-grown Boron marker layers. In both cases, we provided an experimental evidence of the efficient interstitial trapping occurring at the buried Si–SiO_2 interface. In addition, the diffusion-based study allowed to estimate an upper limit (10 nm) for the interface recombination length, L_{imt}.
- We investigated the **formation and evolution of defects in SiGe alloys**, by separating the "chemical" contribution due to the presence of Ge in relaxed alloys from the contribution of strain in strained layers. We found that the increase of Ge concentration in relaxed SiGe structures leads to *(i)* an overall decrease of the defect stability (i.e. a decrease in the total density of interstitials contained in the defects) and to (ii) an enhanced {311}-to-loops transformation. Concerning strain effects we evidenced that *(i)* tensile strain (in Si) retards the transformation of {311} defects into loops; *(ii)* compressive strain (in SiGe) enhances the transformation of {311}s into loops; *(iii)* in all cases, the overall defect stability is not strongly modified in the presence of strain. The existing defect models, developed for silicon, were adapted to the SiGe case by modifying a limited number of model parameters, in agreement with the physical analysis of the experimental study.
- Finally, we investigated the formation of **B-implanted USJs in Germanium** and in particular the stability of these junctions during post-annealing steps. Similarly to the silicon case, Boron deactivation in Ge occurs through two separate phases: a first one of "transient" deactivation promoted by the excess of self-interstitials diffusing out of the EOR defect region; and a second one of precipitation during which boron definitively reaches its solubility limit. However, in Germanium, these two phases require different thermal budgets, so that a full deactivation/reactivation cycle can be e completed with no concomitant

precipitation, i.e. in Germanium, it is possible to achieve highly-activated defect-free p^+-n junctions using the pre-amorphisation technique.

3.6. References

[1] R.H. Dennard, F.H. Gaensslen, H.N. Yu, V.L Rideout, E. Bassous, A.R Le Blanc, IEEE J. Sol.-State Circuits, 9 (1974) 256

[2] E.C. Jones and E. Ishida, Mat. Sci. and Eng. Reports, R24 (1998) 1-80

[3] A.T. Fiory and K.K. Bourdelle, Appl. Phys. Lett., 74 (1999) 2658

[4] A.E. Michel, W. Rausch, P.A. Ronsheim, R.H. Kastl, Appl. Phys. Lett., 50 (1987) 416

[5] International Roadmap for Semiconductor Technology, website: http://public.itrs.net.

[6] A. Gat, J.F. Gibbons, T.J. Magee, J. Peng, V.R. Deline, P. Williams, C.A. Evans, Appl. Phys. Lett., 32 (1978) 276

[7] D.M. Camm, B. Lojek, in Proc. 2nd Int. RTP Conf. (1994), p. 259

[8] T. Ito et al., Intl. Workshop on Jct. Tech. 2002, 23 (2002).

[9] S. McCoy, E. A. Arevalo, J. C. Gelpey, D. F. Downey, Proc. 12th Int RTP Conf. IEEE (2004), p. 99

[10] H.W. Kennel, M.D. Giles, M. Diebel, P.H. Keys, J. Hwang', S. Govindarajul, M. Liu , A. Budrevich, Proc. 14th Int RTP Conf. IEEE (2006), p. 85

[11] N. Weste and K. Eshragian, Principles of CMOS VLSI Design: A Systems Perspective, Addison-Wesley, MA, 1988.

[12] T.C. Chen, Proc. Of the 2006 IEEE International Solid-State Circuits Conference, IEEE, p.1-18

[13] H. Iwai, Microelectronic Engineering 86 (2009) 1520-1528

[14] S.E. Thompson, S. Parthasarathy, Mat. Today, 9(6) (2006) 20-25

[15] J. P. Colinge, SOI Technology: Materials to VLSI, 3rd ed.Kluwer, Boston, 2004.

[16] A. F. Saavedra, K. S. Jones, M. E. Law, and K. K. Chan, Mater. Sci. Eng., B 107 (2004) 198

[17] P.F. Fazzini, F. Cristiano, C. Dupré, S. Paul, T. Ernst, H. Kheyrandish, and K.K. Bourdelle, Mat Sci Eng B 154-155 (2008) 256

[18] J. J. Hamilton, K. J. Kirkby, N. E. B. Cowern, E. J. H. Collart, M. Bersani, D. Giubertoni, S. Gennaro, and A. Parisini, Appl. Phys. Lett. 91 (2007) 092122

[19] J. J. Hamilton, N. E. B. Cowern, E. J. H. Collart, B. Colombeau, M. Bersani, D. Giubertoni, A. Parisini, J. A. Sharp, and K. J. Kirkby, Appl. Phys. Lett. 89 (2006) 042111

[20] T. Skotnicki, C. Fenouillet-Beranger, C. Gallon, F. Boeuf, S. Monfray, F. Payet, A. Pouydebasque, M. Szczap, A. Farcy, F. Arnaud, S. Clerc, M. Sellier, A. Cathignol, J.-P. Schoellkopf, E. Perea, R. Ferrant, H. Mingam, IEEE Trans. Elec. Dev. 55 (2008) 96-130

[21] Y. Song, H. Zhou, Q. Xu, J. Luo, H. Yin, J. Yan, H. Zhong, J. Electronic Mat. 40 (2011) 1584-1612

[22] S.S. Chung, Electrochem. Soc. Transactions, 41(7) (2011) 27-41

[23] K.J. Kuhn, A. Murthy, R. Kotlyar, M. Kuhn, Electrochem. Soc. Transactions, 33(6) (2010) 3-17

[24] V. Moroz, M. Choi, Electrochem. Soc. Transactions, 33(6) (2010) 21-32

[25] Sze, S. M., Physics of Semiconductor Devices, 2nd edition, Wiley, New York, (1981)

[26] M.V. Fischetti, S.E. Laux, J. Appl. Phys. 80 (1996) 2234

[27] Y. Kamata, Materials Today, 11(1-2) (2008) 30-38

[28] J.C. Gelpey, K. Elliott, D. Camm, S. McCoy, J. Ross, D.F. Downey, E.A. Arevalo, Electrochem. Soc. Proc. 2002-11 (2002) 313

[29] W. Lerch, S. Paul, J. Niess, S. McCoy, T. Selinger, J. Gelpey, F. Cristiano, F.Severac, S. Boninelli and P. Pichler, Mat. Sci. and Eng. B, 124-125 (2005) 24

[30] W.Lerch, S.Paul, J.Niess, F.Cristiano, Y.Lamrani, P.Calvo, N.Cherkashin, D.F.Downey and E.A.Arevalo, J. Electrochem. Soc 152 (2005) G787-G793

[31] R. A. Camillo-Castillo, M. E. Law, K. S. Jones, R. Lindsay, K. Maex, B. J. Pawlak and S. McCoy, J. Vac. Sci. Technol. B 24 (2006) 450

[32] M.Foad, E-MRS 2005, Strasbourg, France, private communication

[33] J. Sharp, N. Cowern, R. Webb, D. Giubertoni, S. Gennaro, M. Bersani, M. Foad, K. Kirkby, P.F. Fazzini, F. Cristiano, Appl. Phys. Lett., 89 (2006) 192105

[34] S.Paul, W.Lerch, B.Colombeau, N.E.B.Cowern, F.Cristiano, S.Boninelli and D.Bolze, J. Vac. Sci. and Tech. B, 24 (2006) 437-441

[35] H. Graoui, and M.Foad, Mat. Sci. and Eng., B124-125 (2005) 188

[36] B. J. Pawlak, T. Janssens, B. Brijs, W. Vandervorst, E. J. H. Collart, S. B. Felch and N. E. B. Cowern, Appl. Phys. Lett. 89 (2006) 062110

[37] V. Moroz, Y.S. Oh, D. Pramanik, H. Graoui and M.A. Foad, Appl. Phys. Lett. 87 (2005) 051908

[38] F. Severac, PhD thesis, University of Toulouse, 2008

[39] S. Paul, W. Lerch, J. Chan, S. McCoy, J. Gelpey, F. Cristiano, F. Severac, P. F. Fazzini, D. Bolze: J. Vac. Sci. and Tech. B, 26 (2008) 293

[40] C.H. Poon, A. See, Y.L. Tan, M. Zhou, D. Gui: Electrochem. and Sol. State Lett. Vol. 10 (2007), p. H362

[41] R.A. Camillo-Castillo, M.L. Law, K.S. Jones, L. Radic, R. Lindsay, S. McCoy: Appl. Phys. Lett. Vol. 88 (2006), p. 232104

[42] F. Cristiano, E.M. Bazizi, P.F. Fazzini, S. Boninelli, R. Duffy, A. Pakfar, S. Paul, W. Lerch, Mat. Sci. Forum 573-574 (2008) 269

[43] W. Lerch, S. Paul, J. Niess, S. McCoy, J. Gelpey, F. Cristiano, R. Duffy: ECS Transactions Vol. 3(2) (2006), p. 77

[44] C. Zechner, N. Zographos, D. Matveev, A. Erlebach, Mat. Sci. Eng. B 124-125 (2005) 401

[45] N. Zographos, C. Zechner, I. Avci, Mat. Res. Soc. Symp. Proc., 994 (2007) 297

[46] S. Boninelli, N. Cherkashin, A. Claverie, and F. Cristiano, Appl. Phys. Lett., 89 (2006) 161904.

[47] F. Cristiano, E.M. Baizi, P.F. Fazzini, S. Paul, W. Lerch, S. Boninelli, R. Duffy, A. Pakfar, H. Bourdon, F. Milesi, Proc. IWJT 2008, IEEE (2008) p.114

[48] D. De Salvador, G. Bisognin, E. Napolitani, M. Mastromatteo, N. Baggio, A. Carnera, F. Boscherini, G. Impellizzeri, S. Mirabella, S. Boninelli, F. Priolo and F. Cristiano, Appl. Phys. Lett. 95 (2009) 101908

[49] M. Diebel, S.T. Dunham, Phys. Rev. Lett., 93 (2004) 245901

[50] F. Cristiano, C. Bonafos, A. Nejim, S. Lombardo, M. Omri, D. Alquier, A. Martinez, S.U. Campisano, P.L.F. Hemment, and A. Claverie, Nucl. Instr. and Meth., B127/128 (1997) 22-26.

[51] N.E.B. Cowem, A. Cacciato, J.S. Custer, F.W. Saris, W. Vandervorst, Appl. Phys. Lett., 68 (1996) 1150.

[52] K.L. Yeo, A.T.S. Wee and Y.F. Chong, J. Appl. Phys. 96 (2004) 3692

[53] A.F. Saavedra, Kevin S. Jones, Mark E. Law, Kevin K. Chan and Erin C. Jones, J. Appl. Phys. 96 (2004) 1891

[54] S.W. Crowder, C.J. Hsieh, P.B. Griffin, and J.D. Plummer., J. Appl. Phys. 76 (1994) 2756

[55] Vuong et al., Appl. Phys. Lett. 75 (1999) 1083

[56] K. R. C. Mok, B. Colombeau, M. Jaraiz, P. Castrillo, J.E. Rubio, R. Pinacho, M.P. Srinivasan, F. Benistant, I. Martin Bragado, J.J. Hamilton, Mat. Res. Symp. Proc. 912, C03.04 (2006)

[57] A. Ogura and M. Hiroi, Thin Sol. Films 397 (2001) 56

[58] D. R. Lim, C. S. Rafferty and F. P. Klemens, Appl. Phys. Lett., 67 (1995) 2302

[59] A. Agarwal, H.-J. Gossmann, D. J. Eaglesham, L. Pelaz, D. C. Jacobson, T. E. Haynes, and Yu. E. Erokhin, Appl. Phys. Lett. 71 (1997) 3141

[60] N. E. B. Cowern, D. Alquier, M. Omri, A. Claverie, and A. Nejim, Nucl. Instrum. Methods Phys. Res. B 148 (1999) 257

[61] Y. Lamrani, F. Cristiano, B. Colombeau, E. Scheid, P. Calvo, H. Schaefer, A. Claverie, Nucl. Inst. Meth. Phys. Res. B 216 (2004) 281

[62] P.F. Fazzini, F. Cristiano, C. Dupré, A. Claverie, T. Ernst, M. Gavelle, J. Vac. Sci. Technol. B 26 (2008) 342

[63] E.M. Bazizi, P.F. Fazzini, F. Cristiano, A. Pakfar, C. Tavernier, H. Kheyrandish, S. Paul, W. Lerch, J. Appl. Phys., 107 (2010) 074503

[64] E.M. Bazizi, PhD thesis, University of Toulouse, 2010

[65] A.F. Saavedra, J. Frazer, K.S. Jones, I. Avci, S.K. Earles, M.E. Law, E.C. Jones, J. Vac. Sci. Technol. B 20 (2002) 2243

[66] A.F. Saavedra, A.C. King, K.S. Jones, E.C. Jones, K.K. Chan, J. Vac. Sci. Technol. B 22 (2004) 459

[67] J.F. Ziegler, Nucl. Instr. Meth. B 219–220 (2004) 1027 and www.srim.org

[68] N.E.B. Cowern, K.T.F. Janssen, G.F.A. van de Walle and D.J. Gravesteijn, Phys. Rev. Lett., 65 (1990) 2434.

[69] S. Im, J. Washburn, R. Gronsky, N.W. Cheung and K.M. Yu, Appl. Phys. Lett., 63 (1993) 929.

[70] R.T. Crosby, K.S. Jones, M.E. Law, L. Radic and P.E. Thompson, Appl. Phys. Lett., 87 (2005) 192111.

[71] L. Fedina, O.I. Lebedev, G. Van Tendeloo, J. Van Landuyt, O.A. Mironov, and E.H. Parker, Phys. Rev. B. 61 (2000) 10336.

[72] P.F. Fazzini, F. Cristiano, E. Talbot, G. Ben Assayag, S. Paul, W. Lerch, A. Pakfar, J.M. Hartmann, Thin Solid Films 518 (2010) 2338

[73] C.Vieu, A.Claverie, J.Faure and J.Beauvillain, Nucl. Inst. Meth. B, 28 (1987) 229

[74] F.Cristiano, A.Nejim, P.L.F.Hemment, Yu.Suprun-Belevich, A.Claverie, Nucl. Instr. and Meth., B147 (1999) 35-42

[75] N. R. Zangenberg, J. Lundsgaard Hansen, J. Fage-Pedersen, A. Nylansted Larsen, Phys. Rev. Lett. 87 (2001) 125901.

[76] A. Strohm, T. Voss, W. Frank, J. Räisänen, M. Dietrich, Physica B 308 (2001) 542.

[77] H. Bracht, E. E. Haller, R. Clark-Phelps, Phys. Rev. Lett. 81 (1998) 393.

[78] J.L. Martins and A. Zunger, Phys. Rev. Lett., 56 (1986) 1400

[79] F. K. LeGoues, V. P. Kesan, and S. S. Iyer, Phys. Rev. Lett., 64 (1990) 40

[80] K. Nakagawa, N. Sugii, S. Yamaguchi,M. Miyao, J. Cryst. Growth 201 (1999) 560

[81] Tetelin, C., Wallart, X. ; Nys, J. P. ; Vescan, L. ; Gravesteijn, D. J., J. Appl. Phys 83 (1998) 2842

[82] M. Diebel et S.T. Dunham, Proc. of Int. Conf. on Simul. of Semic. Proc. and Dev. (SISPAD) 2003, IEEE (2003) p.147-150

[83] C. Zechner, N. Zographos, D. Matveev, A. Erlebach, Mat. Sci. Eng. B 124-125 (2005) 401

[84] N. Zographos, C. Zechner, I. Avci, Mat. Res. Soc. Symp. Proc., 994 (2007) 297

[85] E. M. Bazizi, P. F. Fazzini, F. Cristiano, A. Pakfar, C. Tavernier, F. Payet, T. Skotnicki, C. Zechner, N. Zographos, D. Matveev, N. E. B. Cowern, N.S. Bennett, C. Ahn, and J.C. Yoon, IEDM 2010, 15.1.1-4

[86] C. Claeys, E. Simoen, Germanium-Based Technology – From Materials to Devices (Elsevier, Amsterdam, 2007)

[87] C. Claeys, E. Simoen, K. Opsomer, D.P. Brunco and M. Meuris, Mat. Sci. and Eng. B 154 (2008) 49

[88] C. O. Chui, S. Ramanathan, B. B. Triplett, P. C. McIntyre and K. C. Saraswat, IEEE Electron Device Lett. 23(8) (2002) 473

[89] W. Frank, Crucial Issues in Semiconductors Materials and Processing Technologies, Kluwer Dordrecht, 1992, pp. 383–402

[90] M. Werner, H. Mehrer, H.D. Hochheimer, Phys. Rev. B, 32 (1985) 3930

[91] Laitinen et al., Phys. Rev. Lett., 89 (2002) 085902

[92] S. Brotzmann and H. Bracht, J. Appl. Phys., 103 (2008) 033508

[93] A. Satta, E. Simoen, T. Clarysse, T. Janssens, A. Benedetti and B.D. Jaeger, Appl. Phys. Lett., 87 (2005) 172109

[94] Y.L. Chao, S. Prussin, J.C.S. Woo and R. Scholz, Appl. Phys. Lett, 87 (2005) 142102

[95] A. Satta, E. Simoen, R. Duffy, T. Janssens, T. Clarysse, A Benedetti, M. Meuris and W. Vandervorst, Appl. Phys. Lett., 88 (2006) 162118

[96] D.P. Hickey, Z.L. Bryan, K.S. Jones, R.G. Elliman and E.E. Haller, J. Vac. Sci. Technol. B, 26 (2008) 425

[97] S. Koffel, N. Cherkashin, F. Houdellier, M.J. Hytch, G. Benassayag, P. Scheiblin and A. Claverie, J. Appl. Phys, 105 (2009) 126110

[98] F. Panciera, P.F. Fazzini, M. Collet, J. Boucher, E. Bedel, F. Cristiano, Appl. Phys. Lett., 97 (2010) 012105

[99] S. Uppal, A. F. W. Willoughby, J. M. Bonar, N. E. B. Cowern, T. Grasby, R. J. H. Morris and M. G. Dowsett, J. Appl. Phys., 96 (2004) 1376.

Perspectives

Since I joined CRNS in 1998, my research activity has focused on the structural analysis of implantation-induced defects in Silicon and SiGe-based materials and on their impact on dopant diffusion and activation anomalies.

The context of my research was the need to improve the performances of MOS transistors, the building block of all integrated circuits, through their miniaturisation (i.e. the "*More Moore*" paradigm). This included, among other issues, the fabrication of *Ultra Shallow Source/Drain Junctions*, whose doping is mainly achieved by ion implantation.

For my investigations, I used several complementary characterization methods, the main ones being TEM for the structural analysis, SIMS for the chemical dopant profiling and Hall-effect for the electrical investigations. In addition to the understanding of the various investigated phenomena achieved through my work, I also contributed to the improvement of the existing physical models (or to the development of new ones when necessary) for the predictive simulations of USJ fabrication.

Due to the increased difficulties to maintain the MOS miniaturization pace [1] (as well as to the approaching of its physical limits), the general context of the MOS-related research domain has largely evolved over the last years.

On the one hand, the continuous increase of short channel effects, including increasing parasitic resistances and capacitances, has put forward the reduction of power consumption as the main issue to be solved in future device generations. Research studies towards this objective will therefore be crucially important to ensure the development of future MOS technology until the end of the roadmap, which is currently estimated by the ITRS around the 22 nm technology node for "bulk" Si transistors, the 14 nm node for FDSOI, and the 7 nm node for 3D multi-gate (FinFETs or Nanowire-based) MOS [2]. In addition, on the short-medium term, new research will be still stimulated by other important issues, including the continuous improvement of strain engineering methods for the increase of carrier mobility, the integration of alternative high-mobility channel materials and, particularly for the S/D junction fabrication, the continuous optimisation of advanced doping and annealing schemes.

On the other hand, the years 2000s have seen the emergence of the so-called "*More-than-Moore*" domain [3], consisting in the addition of novel functionalities to electronic devices based on (or derived from) Silicon MOS technology. The "*More-than-Moore*" domain covers a wide spectrum of product categories, including RF, high-voltage/power, SiP, passives, sensors, actuators, microfluidic, biochip, etc. and has become more and more strategically important in the European research scenario

[4]. Moreover, the future developments in the "*More-than-Moore*" domain[#] are foreseen in ITRS as part of an "extended-CMOS" vision, i.e. MOS technology is considered as an "extended platform" for the integration of future multifunctional electronics. As a consequence, despite "*More-than-Moore*" extra-functionalities do not necessarily scale with Moore's law, future research in this domain will have to be strictly "connected" to research in advanced-MOS devices [5].

In the next years, **I therefore plan to pursue within this "extended-CMOS" context my research activity on the investigation of physical phenomena related to the use of ion implantation in semiconductor processes for "More Moore" and "More than Moore" applications**. In addition, I will contribute to two new research activities recently developed within the MPN[##] research group of LAAS that I lead since January 2012, one focused on the improvement of carrier mobility in SiC power devices, and the other on the development of nanowire-based systems.

Concerning future studies on implantation-induced defects, the crucial "power-crisis" issue mentioned above naturally leads to the need of investigating their impact on leakage currents, which strongly contribute to the increase of power consumption, critically important for instance in mobile communication devices, or to unwanted dark currents in CMOS image devices. Indeed, most of the junction fabrication methods used today are expected to result in the formation of new and complex distributions of extended defects and defect-dopant clusters, especially in the case of cocktail and high-dose plasma implants. In all cases, these defects are expected to have a major impact on the junction leakage currents. The identification of the phenomena responsible for their appearance, in particular the correlation with certain defects and processing parameters, is therefore a high challenge. In addition, the electrical properties of extended defects are not taken into account in the physical models currently implemented in TCAD simulators, explaining why fundamental studies aiming at evaluating them are today necessary.

Several studies on the electrical characterization of implantation induced defects have been mostly reported until the end of the 1990s. However, the correlation of energy levels to the extended defects has not been definitely established. Thanks to the improved knowledge that I have contribute to establish over the last decade on the energetics, formation and evolution mechanisms from point to extended defects, it is therefore possible today to achieve a better understanding of the defect electrical properties by combining deep level transient spectroscopy (DLTS) measurements with atomistic simulations and structural analysis of the defect nature, density and size.

[#] As well as in the "*Beyond CMOS*" domain, not discussed here.

[##] Materials and Processes for Nanoelectronics

In fact, thanks to the electrical characterization skills available within the MPN group, we recently started this activity within the EU project ATEMOX[#], by establishing a characterization protocol involving a specially designed test structure that places the implantation defects within probing range of the DLTS technique and applying it to silicon material containing defects generated by conventional implantation and annealing schemes. The combination of DLTS results with TEM investigations and predictive defect simulations allows to unambiguously associate the deep energy levels measured by DLTS to a given defect configuration, while the combination of DLTS and I-V measurements from the same test structures allows to identify the most relevant defects in terms of leakage current generation.

In the future, this work, currently carried out on silicon material using conventional implantation and annealing schemes, will be extended to *(i)* alternative implant methods, such as Plasma Immersion Ion Implantation (PIII), *(ii)* advanced annealing processes, such as *non-melt* and *melt* Laser anneals or extremely low SPER[##] (~500°C) anneals, particularly important for 3D integration schemes [6] and *(iii)* high-mobility substrate materials, such as Ge and III-Vs. However, in most of these domains, the current knowledge on the defect formation and evolution mechanisms is far from being as mature as in the "reference" silicon case. Further structural studies will therefore be necessary before (or while) investigating the electrical impact of defects induced by these advanced processes/materials.

In particular, on the basis of the currently established collaborations, we will primarily address the three areas detailed below:

a. Plasma Implantation

With respect to conventional beamline implantation, PIII can provide shallow implants with higher beam current, making it attractive for the fabrication of heavily-doped regions in MOS-based technologies [7], including S/D junctions, polysilicon gate or backside doped layers in image sensors [8]. In addition, PIII process conditions can be adjusted to achieve 3D conformal doping which can be used for the fabrication of doped shallow and deep trenches for the isolation of adjacent devices or the fabrication of S/D regions in multi-gate MOS architectures (FinFETs or nanowire-based). However, **the multi-species, multi-energetic and multi-angular nature of PIII results in complex dopant and defect distributions that are still difficult to predict**, including the formation of large and stable Boron precipitates that are neglected in current process simulators.

[#] www.atemox.eu

[##] Solid Phase Epitaxial Regrowth

Among the several issues related to the use of this doping method, the first to be investigated will concern the use of BF_3 for the fabrication of p-type doped regions. The high implant doses typically used (of the order of $1x10^{15}$ cm^{-2}) combined with the low implant energy (<5 keV) result in the amorphisation of a shallow surface layer (<10 nm), with Boron and Fluorine concentrations below the a/c interface as high as $1x10^{20}$ cm^{-3}. In such conditions, the combined effects of high B and F concentration and of surface proximity make it difficult to predict which of the known defect formation phenomena will dominate during annealing (formation of Si-interstitial defects with Boron decoration, formation of large Boron precipitates, EOR stabilisation induced by Fluorine…), as indicated by the preliminary investigations carried out within the EU project ATEMOX. Future work will therefore aim at the development of new physical models to predict the formation of large Boron precipitates in the presence of additional interactive impurities (F or H for the case of B_2H_6 plasma implants).

b. Laser annealing

Concerning Laser annealing, the focus of future research will be mostly placed on *melt* annealing conditions for which current knowledge on defect formation is quite limited compared to other ultra-fast *non-melt* methods (either laser-based or Flash-assisted). The low thermal budget of a laser pulse with duration in the nanosecond regime allows melting and recristallisation (liquid phase epitaxy) of the implanted region while no significant annealing of areas away from the surface takes place. This makes this technique very attractive *per se* for the achievement of USJs [9,10,11] but more generally for all semiconductor technologies in which dopants need to be activated while preserving the integrity of the surrounding areas, as in the case of 3D integration [12], thin film displays [13], high-frequency bipolar silicon-on-glass processes [14] or CMOS backside imagers [15]. In the melt regime, box shaped profiles with activation rates close to 100% and excellent surface uniformity can be obtained, however **little is known on the defect formation below the original liquid/solid interface, where highly damaged material is exposed to a non-melt anneal for few nanoseconds**, the main difficulty being due to the different time constants of the several key physical processes occurring during the anneal at this timescale [16]. To give an example, our preliminary results obtained within the EU project ATEMOX on non-amorphised B-implanted silicon structures indicate that unexpected Boron precipitation occurs in this region (**Erreur ! Source du renvoi introuvable.** [17]) even when B concentration is well below the solid solubility value. Such defect formation is totally unexpected within the conventional defect models based on diffusion-limited mechanisms, therefore calling for further work on the defect formation mechanisms at the nanosecond timescale.

c. Germanium

The interest in using Germanium to replace Si as a high-mobility channel material was triggered in the early 2000s by the successful implementation of high-k dielectrics to replace SiO_2 in Si MOS [18,19]. Since then, the feasibility of high-performing p-channel Ge devices has been demonstrated [20] while good performing n-channel devices remain an issue [21]. This is mainly due to the poor quality of the Ge/high-k interface, leading to degraded mobility and the difficulties in controlling the behaviour (diffusion and activation) of n-type dopants in S/D regions, the latter issue being intimately related to the damage evolution during annealing.

To this respect, several open questions remain to be clarified in order to fully understand and predict dopant incorporation in germanium. These include:

(i) the determination of the exact defect evolution mechanism, which is "hindered" by the weak defect size evolution as well as the relatively short process window for a direct defect analysis by TEM;

(ii) the role of the surface on damage evolution, which is proposed to act as a reflecting boundary for point defects [22] on the basis of dopant diffusion experiments, while recent TEM investigations of EOR damage evolution [23] indicate an opposite behaviour (i.e. surface can effectively trap point defects diffusing out of the damage region);

(iii) the impact of co-implanted impurities, such as Fluorine which if found to be deleterious for some authors [24] or extremely beneficial for others [25];

(iv) the identification of the best strategy to achieve high dopant activation, including low temperature SPER [26], high-temperature laser anneal [27], multiple low-dose implantation/annealing cycles [28] or point-defect engineering, such as interstitial injection (from neutral species implants) to reduce the concentration of vacancies, which are at the origin of the formation of inactive V-dopant clusters [29].

In fact, despite the reported progress on dopant activation, state-of-the-art data show that junction depths achieved by ion implantation are still deeper than the ITRS targets [30], so that Ge-on-insulator or other thin-body germanium architectures might be necessary to allow Ge implementation in advanced planar MOS technology [**Erreur ! Signet non défini.**]. However, whether or not Ge will ever make its way into planar MOS technology [31], **further research on implantation related issues in Germanium will be still extremely valuable when considering the increasing interest towards this material in other MOS-related technologies in the More-than-Moore domain**, such as photodetectors [32,33].

Indeed, Germanium has a higher absorption coefficient in Ge, which makes it an extremely attractive material for use in high-performance infrared detectors. In addition, the higher carrier mobility compared to Si, might result in improved device

speed, as well as the ability to operate at low voltages. Ge photodetectors, implemented in the form of p-i-n vertical or horizontal structures, were initially demonstrated by locally growing a Germanium layer on relaxed SiGe virtual substrates [34], while in more recent works, Germanium is directly grown on Si [35] or SOI [36]. Concerning the p/n doped regions, they are realized in most cases by ion implantation.

Among the various performance requirements of Ge photodetectors (such as speed, responsivity and low-voltage operation), **a critically important one is the control of the dark current, which is intimately related to the presence of extended defects in the grown structures**. The two main defect "sources" are *(i)* the damage due to the implant steps used to fabricate the p/n doped regions and *(ii)* the lattice mismatch between the Ge and the Si substrate that result in the formation of misfit and threading dislocations. It is therefore clear that the "ion implantation-related issues" mentioned above in the case of high-performance Ge MOSFETs need also to be addressed in the context of Ge photodetectors.

On the other hand, misfit dislocations formed at the Ge-Si interface, in addition to inducing undesired dark currents, also enhance the updiffusion of Si into the Ge layer [37], which results in the formation of a SiGe layer and hence in a degradation of the detector efficiency, especially at longer wavelengths. Our previous experience in the field of dopant diffusion and specifically in the investigation of Ge/Si interdiffusion [38], will therefore allow me to improve the understanding of this phenomenon, so to contribute to the process optimisation.

On the basis of the skills and knowledge that I acquired during my previous research work, I therefore plan to pursue my investigations of doping-diffusion issues in Germanium in the next future and give my contribution to the solution of the several issues mentioned above.

Finally, in the last part of this section, I will shortly present two research activities recently started within the MPN research group, to which I contribute thanks to the experience I gained over the years on ion implantation-induced damage or on doping issues in source/drain regions of MOS devices.

The first is coordinated by Eléna Bedel and concerns the improvement of carrier mobility in SiC power devices. Today, SiC is certainly the most promising semiconductor for future high-temperature and high-power electronic devices due to its superior physical and electrical properties compared to silicon. However, the potential of SiC is limited by several problems [39,40], one of them being the large density of traps at the SiC/SiO_2 interface. These traps can capture charges and act as Columbic scattering centers and hence reduce the mobility of channel electrons. In

addition, because of the large density of interface traps, commonly used transfer characteristics analyses are not suitable for the reliable determination of the electrical transport properties of SiC MOSFETs [41,42]. Concerning the possible origin of these traps, some investigations proposed that bulk traps in SiC may play a role in reducing electron mobility, possibly related to carbon clusters located at or in the vicinity of the SiC/SiO_2 interface [43,44]. These suggestions have recently been supported by some TEM investigations, based on Z-contrast [45] or EELS[#] [46] imaging methods, claiming that such C-based clusters were indeed formed.

Within this context, I coordinate the ANR-PICF project MobiSiC, started at the end of 2010 and run in collaboration with the FhG-IISB laboratory of Erlangen, Germany and the CEMES-CNRS laboratory in Toulouse. While the TEM-EELS investigations run at CEMES have allowed to raise some doubts on the claimed observations of C-based clusters, as no evidence of these clusters was found in many investigated test structures, our group has implemented a Hall-effect measurement method for the reliable determination of the carrier density and mobility in the channel of SiC MOSFETs fabricated using a Hall-bar configuration. In particular, we currently investigate the beneficial impact of a Nitrogen implant in the channel region of n-MOSFETs, which leads to an improved passivation of bulk traps and therefore to an increase in carrier mobility. In addition, thanks to a further collaboration with the ONERA laboratory in Toulouse, we have access to Hall-effect measurements in a wide temperature range, allowing to investigate in detail the dominant scattering mechanisms.

Due to the growing interest towards this material system, both in the academic and the industrial domain, we plan to pursue this research axis in the next years, especially considering that, in addition to the mobility concerns currently investigated, the doping of source/drain regions in SiC MOSFETS still represents a critical issue [47,48], due to the unwanted material etching or surface roughening that can occur during the post-implantation annealing [49], calling among other solutions, for novel annealing methods [50,51] to improve dopant activation.

The second activity recently started within the MPN group and to which I plan to contribute is coordinated by Guilhem Larrieu. It concerns the development of nanowire-based field effect transistors (NW-FETs), which are among the most promising solutions to overcome the limits of today's electronic devices based on planar silicon, especially for their ability to implement gate-all-around architectures [52]. Indeed, NW-FETS provide the ideal configuration for the electrostatic control of the charge carriers in the channel and can ensure the further reduction of the "ultimate" transistor size while managing the leakage current.

[#] Electron Energy Loss Spectroscopy

Among the possible device architectures, the one based on the use of dense vertical nanowire arrays fabricated by the "top-down" approach is currently being developed at LAAS, which, in addition to the "ultimate" MOS scaling, is also a very promising approach for the realisation of future "More-than-Moore" devices, including high sensitive biochemical sensors [53] or photovoltaic cells [54].

However, before achieving such promising results, significant fundamental challenges need to be addressed that cover several research domains, including device engineering and materials science. These include the reduction of the S/D series resistance and of the interface defects at the gate dielectric/NWs interface.

Concerning the S/D issue, the use of ion implantation for the realisation of highly doped NWs, is questionable, with opposite results claiming either a reduced amount of structural disorder in implanted Si-NWs compared to bulk Si [55] or an "unrecoverable" amorphisation damage during annealing of FinFETs Si structures [56]. For this reason, while an alternative S/D fabrication option based on the implementation of "Schottky contacts" will be developed in parallel (including the dopant segregation technique [57]), we plan to follow an incremental approach to fully investigate the potential of ion implantation for the realisation of S/D contacts in NW-based transistors.

Within this approach, several fabrication schemes will be tested: *(i)* implantation and activation in the Si bulk followed by the NWs structuring; *(ii)* implantation in the bulk and activation after the Si NWs formation or *(iii)* implantation and activation after the Si NWs formation. Radial junction will be also evaluated using plasma doping (in collaboration with Ion Beam Services), where the incorporation of the dopants in 3D and the effect of the NW array density will be particularly studied.

The assessment of the investigated processes will be based on the combined use of structural and electrical characterisation methods. Transmission Electron Microscopy will be used to characterise the fabricated structures in terms of their crystalline structure, the quality of the NW surfaces, the presence of extended defects created during the implant/anneal/etch procedure, the possible formation of large clusters of doping atoms and the presence of strain in the nanowires (the most advanced characterisation techniques will be implemented with the support of the CEMES-CNRS laboratory). Finally, concerning the electrical characterisations, two-terminal structures will be directly implemented on vertical Si NWs arrays [58]. This represents an interesting advantage of the "top-down" fabrication approach, as it considerably attenuates variability issues associated to the stochastic nature of the fabrication process steps at the nanoscale and allows to characterise the NWs in the absence of any manipulations following their fabrication, as in the case of "bottom-up" grown NWs.

References

[1] H. Iwai, Microelectronic Engineering 86 (2009) 1520-1528

[2] 2011 International Roadmap for Semiconductor Technology, "Front-End Processes" Chapter, http://public.itrs.net.

[3] G.Q. Zhang, F. van Roosmalen, M. Graef, 6th Int. Conf. on Electronic Packaging Technology, IEEE 2005

[4] SINANO Institute vision, June 2009

[5] Report of the FP7 Workshop on Advanced Nanoelectronics Technologies, Brussels, September 2009

[6] P. Batude, M. Vinet, B. Previtali, C. Tabone, C. Xu, J. Mazurier, O. Weber, F. Andrieu, L. Tosti, L. Brevard, B. Sklenard, P. Coudrain, S. Bobba, H. Ben Jamaa, P. Gaillardon, A. Pouydebasque, O. Thomas, C. Le Royer, J. Hartmann, L. Sanchez, L. Baud, V. Carron, L. Clavelier, G. De Micheli, S. Deleonibus, O. Faynot, and T. Poiroux, IEDM 2011, 7.3.1 -7.3.4, IEEE

[7] F.Gonzatti, F.Milési, V.Delaye, J.Duchaine, F.Torregrosa, H.Etienne, K.Yckache, *Proc. IIT10, ed.J.Matsuo et al., AIP 2010*, p.27

[8] K.C. Ku, C.Y. Liu, H.C. Tai, V. Venezia, US Patent 2012/0080765

[9] Y. Takamura, S. H. Jain, P. B. Griffin, and J. D. Plummer, J. Appl. Phys. 92 (2002) 230

[10] E.V. Monakhov, B.G. Svensson, M.K. Linnarsson, A. La Magna, V. Privitera, M. Camalleri, G. Fortunato, L. Mariucci, Mat. Sci. Eng. B, 114-115 (2004) 352

[11] S.W. Do, S.H. Kong, Y.H. Lee, J.G. Oh, J.K. Lee, M.A. Ju, S.J. Jeon, J.C. Ku, J. Korean Phys. Soc., 55 (2009) 1065

[12] B. Rajendran, R.S. Shenoy, M.O. Thompson, R.F.W. Pease, Prc. Of the 2004 VLSI Multilevel Interconnection Conference, IEEE 2004

[13] Kagan, C. R. and Andry, P. (2003). Thin-film transistors. Marcel Dekker Inc

[14] G. Lorito, V. Gonda, S. Liu, T.L.M. Scholtes, H. Schellevis, L.K. Nanver, Proc. of 2006 MIEL Int. Conf. (International Conference on Microelectronics), vol. 25, p. 342, IEEE 2006

[15] H. Bourdon, A. Halimaoui, J. Venturini, F. Gonzatti, D. Dutartre, 15th International Conference on Advanced Thermal Processing of Semiconductors, Catania (2007), p. 275

[16] H.W. Kennel, M.D. Giles, M. Diebel, P.H. Keys, J. Hwang', S. Govindarajul, M. Liu , A. Budrevich, Proc. 14th Int RTP Conf. IEEE (2006), p. 85

[17] Y. Qiu, F. Cristiano, K. Huet, A. La Magna, *to be published*

[18] B.H. Lee, J.W. Oh, H.H. Tseng, R. Jammy, H. Huff, Materials Today, vol. 9, June 2006, 32

[19] C. Claeys, E. Simoen, K. Opsomer, D.P. Brunco, M. Meuris, Mat. Sci. Eng. B, 154 (2008) 49

[20] J.Mitard, B. De Jaeger, F.E. Leys, G. Hellings, K.Martens, G. Eneman, D.P. Brunco, R. Loo, J.C. Lin, D. Shamiryan, T. Vandeweyer, G. Winderickx, E. Vrancken, C.H. Yu, K. De Meyer, M. Caymax, L. Pantisano, M. Meuris, M.M. Heyns, IEDM Tech. Dig., 2008, p. 873.

[21] Y. Song, H. Zhou, Q. Xu, J. Luo, H. Yin, J. Yan, H. Zhong, J. Electronic Mat. 40 (2011) 1584-1612

[22] H. Bracht, S. Schneider, R. Kube, Microelectr. Eng., 88 (2011) 452

[23] S. Boninelli, G. Impellizzeri, A. Alberti, F. Priolo, F. Cristiano, C. Spinella, Appl. Phys. Lett., 101 (2012) 162103

[24] G. Hellings, E. Rosseel, T. Clarysse, D.H. Petersen, O. Hansen, P.F. Nielsen, E. Simoen, G. Eneman, B. De Jaeger, T. Hoffmann, K. De Meyer, W. Vandervorst, Microelectr. Eng., 88 (2011) 347

[25] W.-S. Jung, J.H. Nam, J.-Y.J. Lin, S. Ryu, A. Nainani, K.C. Saraswat, Proc. 6th ISTDM Conf, June 2012 Berkeley (USA), IEEE 2012

[26] R. Duffy, M. Shayesteh, M. White, J. Kearney,A.-M. Kelleher, Appl. Phys. Lett., 96 (2010) 231909

[27] G. Thareja, S. Chopra, B. Adams, Y. Kim, S. Moffatt, K. Saraswat, Elec. Device Letters, 32 (2011) 838

[28] J. Kim, S.W. Bedell, D.K. Sadana, Appl. Phys. Lett., 101 (2012) 112107

[29] J. Vanhellemont and E. Simoen, Mat. Sci. in Semic. Proc., 2012 in press

[30] G. Hellings, E. Rosseel, T. Clarysse, D. Hjorth Petersen, O. Hansen, P. Folmer Nielsen, E. Simoen, G. Eneman, B. De Jaeger, T. Hoffmann, K. De Meyer, W. Vandervorst, Microelec. Eng., 88 (2011) 347

[31] K.J. Kuhn, M.Y. Liu, H. Kennel, Proc. of 2010 Int. Work. On Junction Technology, IEEE 2010.

[32] B. Ackland, C. Rafferty, C. King, I. Aberg, J. O'Neill, T. Sriram, A. Lattes, C. Godek and S. Pappas, 2009 IISW (Int. Work. Image Sensor Workshop), Bergen Norway, June 2009, paper 053, IEEE.

[33] M. Takenaka, K. Morii, M. Sugiyama, Y. Nakano, S. Takagi, Optics Express 20 (2012) 8718

[34] S.B. Samavedam, M.T. Currie, T.A. Langdo, E.A. Fitzgerald, Appl. Phys. Lett., 73 (1998) 2125

[35] L. Vivien, A. Polzer, D. Marris-Morini, J. Osmond, J.M. Hartmann, P. Crozat, E. Cassan, C. Kopp, H. Zimmermann, J.M. Fédéli, Optics Express, 20 (2012) 1097

[36] S.J. Koester, J.D. Schaub, G. Dehlinger, J.O. Chu, IEEE J. of Selected Topics in Quatum Electr., 12 (2006) 1489

[37] M. Gavelle, E.M. Bazizi, E. Scheid, P.F. Fazzini, F. Cristiano, C. Armand, W. Lerch, S. Paul, Y. Campidelli, A. Halimaoui, J. Appl. Phys. 104 (2008) 113524

[38] M. Gavelle, PhD Thesis, Univ. Paul Sabatier, Toulouse, 2007

[39] A. Agarwal, S. Haney, J. Elec. Mater 37 (2008) 646-654

[40] S. Potbhare, N. Goldsman, G. Pennington, A. Lelis, J. M. McGarrity, J. Appl. Phys. 100 (2006) 044515, 1-8

[41] N. S. Saks and A.K. Agarwal, Appl. Phys. Lett. 77, 20 (2000) 3281-3283

[42] N. Saks, "Hall effect studies of electron mobility and trapping at the SiC/SiO_2 interface", in Silicon Carbide – Recent Major Advances, W.J. Choyke, H. Matsunami, and G. Pensl (Eds), Springer, New York, 2004, pp. 387-410

[43] G. Y. Chung, C. C. Tin, J. R. Williams, K. McDonalds, M. Di Ventra, S. T. Pantelides, L. C. Feldman, R. A. Weller, Appl. Phys. Lett. 76 (2000) 1713-1715

[44] X. Shen, S. T. Pantelides, Appl. Phys. Lett. 98 (2011) 053507

[45] T. L. Biggerstaff, C. L. Reynolds, T. Zheleva, A. Lelis, D. Habersat, S. Haney, S.-H. Ryu, A. Agarwal, G. Duscher, Appl. Phys. Lett. 95 (2009) 032108

[46] T. Zheleva, A. Lelis, G. Duscher, F. Liu, I. Levin, M. Das, Appl. Phys. Lett. 93 (2008) 022108

[47] A. Poggi, F. Bergamini, R. Nipoti, S. Solmi, M. Canino, A. Carnera, Appl. Phys. Lett., 88 (2006) 162106

[48] R. Nipoti, A. Nath, S.B. Qadri, Y.L. Tian, C. Albonetti, A. Carnera, M.V. Rao, J. Electronic Mat., 41 (2012) 457

[49] Y. Negoro, N. Miyamoto, T. Kimono, and H. Matsumani, Mater. Sci. Forum 389-393 (2002) 783

[50] S.G. Sundaresan, M. Mulpuri, V. Rao, Y.-L.. Tian, J.A. Schreifels, M.C. Wood, K.A. Jones, A.V. Davydov, J. Elec. Mat., 36 (2007) 324

[51] R. Nipoti, A. Nath, M.V. Rao, A. Hallen, A. Carnera, Y.-L. Tian, Appl. Phys. Express, 4 (2011) 111301

[52] J. Appenzeller, J. Knoch, M.T. Björk, H. Riel, H. Schmid, W. Riess, IEEE Trans. Elec. Dev. 55 (2008) 2827

[53] G.J. Zhang, G. Zhang, J.H. Chua, R.E. Chee, E.H. Wong, A. Agarwal, K.D. Buddharaju, N. Singh, Z. Gao, N. Balasubramanian, Nano Lett. 8 (2008) 1066

[54] Z. Fan, H. Razavi, J.-W Do, A. Moriwaki, O. Ergen, Y.-L. Chueh, P.W. Leu, J.C. Ho, T. Takahashi, L.A. Reichertz, S. Neale, K. Yu, M. Wu, J.W. Ager, X.A. Javey, Nat. Mat. 8 (2009) 648

[55] A. Colli, A. Fasoli, C. Ronning, S. Pisana, S. Piscanec, A.C. Ferrari, Nanolett., 8 (2008) 2188

[56] R. Duffy, M.J.H. Van Dal, B.J. Pawlak, M. Kaiser R.G.R. Weemaes, B. Degroote, E. Kunnen, E. Altamirano, Appl. Phys. Lett., 90 (2007) 241912

[57] G. Larrieu et al., IEDM'07, pp. 147–150, Dec. 2007

[58] X.L. Han, G. Larrieu, E. Dubois and F. Cristiano, Surf. Sci. 606 (2012) 836

Appendix

Model for Boron deactivation/reactivation in PAI USJs

The results shown in section 2.2 suggest that the Boron deactivation mechanism (boron clustering) during annealing is driven by the emission of Si self-interstitials from the end-of-range defects. On the other hand, the reactivation (decrease of the sheet resistance) is the combined result of two different mechanisms: cluster dissolution and dopant diffusion. In order to quantitatively interpret the deactivation/reactivation results, a simple model developed with the help of Pierre Temple-Boyer from LAAS is presented below that gives the time evolution of the active dose as it is directly measured by Hall-effect. The model is schematically represented in Figure 1.

The implanted boron profile contains two regions: region "A", below the solid solubility, contains N_A electrically active boron atoms; and region "B", above the solid solubility, contains N_B clustered and electrically inactive boron atoms. Finally, the EOR defects region is characterized by the number of Si atoms stored in the EOR, N_{EOR}. During annealing, we already showed that the EOR defects dissolve following an exponential decay (cf. figure 2-a, section 3), inducing a flux $\vec{J}_{EOR}$, of Si interstitial atoms towards the surface. We assume that for each diffusing interstitial atom, a number α of boron atoms in region "A" are clustered and "move" to region "B". In parallel, the clustered boron atoms in region "B" are not energetically stable and are assumed to dissolve following, also, an exponential decay, liberating boron atoms from region "B" into region "A".

Under these assumptions, the whole system can be described by the following equations:

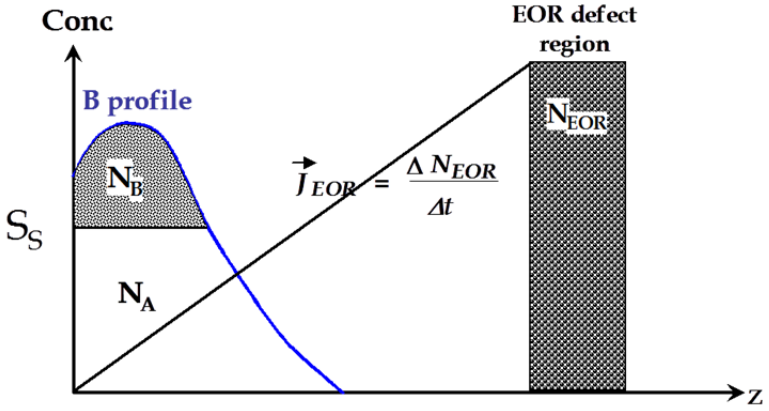

Figure 1 – Schematic representation of the boron chemical concentration depth-profile (region (A) below the solid solubility and region (B) above the solid solubility), and of the EOR defects region; for the SPEG post-annealed samples.

$$\begin{cases} dN_{EOR} &= & -N_{EOR}\dfrac{dt}{\tau_{EOR}} \\ dN_A &= & -\alpha\cdot N_{EOR}\dfrac{dt}{\tau_{EOR}} + N_{BIC}\dfrac{dt}{\tau_{BIC}} \\ dN_{BIC} &= & +\alpha\cdot N_{EOR}\dfrac{dt}{\tau_{EOR}} - N_{BIC}\dfrac{dt}{\tau_{BIC}} \end{cases} \quad (1)$$

The first equation describes the EOR dissolution, characterized by a decay time τ_{EOR}. The active dose N_A decreases following the EOR dissolution and increases when boron clusters dissolve (with a decay time τ_{BIC}). While N_B follows an opposite behavior to that of N_A.

The solution to this system of differential equations is given by the following equations:

$$\begin{cases} N_{EOR}(t) &= & N_{EOR}(0)\exp\left(-\dfrac{t}{\tau_{EOR}}\right) \\ N_B(t) &= & \left\{N_B(0) - \dfrac{\alpha\tau_{BIC}}{\tau_{EOR}-\tau_{BIC}}\cdot N_{EOR}(0)\right\}\cdot\exp\left(-\dfrac{t}{\tau_{BIC}}\right) + \dfrac{\alpha\tau_{BIC}}{\tau_{EOR}-\tau_{BIC}}\cdot N_{EOR}(0)\cdot\exp\left(-\dfrac{t}{\tau_{EOR}}\right) \\ N_A(t) &= & \Phi - N_{BIC}(t) \end{cases} \quad (2)$$

The experimental results presented in the previous section, indicate that the deactivation mechanism is systematically more effective than the reactivation one at the beginning of the annealing. We can therefore reasonably assume that $\tau_{EOR} \ll \tau_{BIC}$ at all temperatures. As a consequence, the expression for N_B can be simplified to the following expression:

$$N_B(t) = \left\{N_B(0) + \alpha\cdot N_{EOR}(0)\left[1-\exp(-\frac{t}{\tau_{EOR}})\right]\right\}\exp\left(-\frac{t}{\tau_{BIC}}\right) \quad (3)$$

Thus, we deduct the explicit solution for N_A:

$$N_A(t) = \Phi - N_B(t) \quad (4)$$

The $N_A(t)$ expression contains three free parameters (α, τ_{BIC}, and τ_{EOR}), while all other parameters ($N_B(0), N_{EOR}(0)$, and Φ) are extracted from the measurements. However, for both very short annealing times ($t \ll \tau_{EOR}$) and very long ones ($t \gg \tau_{EOR}$), $N_A(t)$ assumes a linear form:

$$\begin{cases} N_A(t) &= a_1 + b_1\cdot t \quad , \quad for \quad t \ll \tau_{EOR} \\ N_A(t) &= a_2 + b_2\cdot t \quad , \quad for \quad t \gg \tau_{EOR} \end{cases} \quad (5)$$

With:

$$\begin{cases} a_1 = N_A(0) - \alpha \cdot N_{EOR}(0) \\ b_1 = \dfrac{N_{BIC}(0) + \alpha \cdot N_{EOR}(0)}{\tau_{BIC}} \end{cases} \quad \text{and} \quad \begin{cases} a_2 = N_A(0) \\ b_1 = -\dfrac{\alpha \cdot N_{EOR}(0)}{\tau_{EOR}} \end{cases} \tag{6}$$

If the slopes (b_1 and b_2) and intercepts (a_1 and a_2) of the linear regions are extracted from the experimental curves, it is therefore possible to evaluate the three free parameters without using a numerical procedure:

$$\begin{cases} \tau_{EOR} = -\dfrac{N_A(0) - a_1}{b_2} \\ \alpha = \dfrac{N_A(0) - a_1}{N_{EOR}} \\ \tau_{BIC} = \dfrac{N_{BIC}(0) + N_A(0) - a_1}{b_1} \end{cases} \tag{7}$$

In practice, the annealing times used in this work were not long enough to observe a clear linear increase of $N_A(t)$ for $t >> \tau_{EOR}$ at all temperatures. We therefore used only the short time approximation to evaluate α by using a_1 extracted from the data obtained at 900°C. Then, we fixed the α for all temperatures. A numerical fitting procedure was then used to extract the values of τ_{EOR} and τ_{BIC}.